High Pressure Hydrogen Dehydration Using Ionic Liquids

J.C.B. Brenkman

Technische Universiteit Delft

TU Delft

Delft
University of
Technology

Challenge the future

High Pressure
Hydrogen Dehydration
Using Ionic Liquids

by

J.C.B. Brenkman

in partial fulfillment of the requirements for the degree of

Master of Science
in Mechanical Engineering
Track: Energy & Process Technology

at the Delft University of Technology,
to be defended publicly on Wednesday June 26, 2019 at 9:00 AM.

Student number:	4169093	
Supervisor:	Rogier Schoon	Royal Dutch Shell
Thesis committee:	Prof. dr. ir. T.J.H. Vlugt	Delft University of Technology
	Prof. dr. ir. R.A.W.M Henkes	Delft University of Technology
	Dr. ir. M. Ramdin	Delft University of Technology
	Dr. ir. D.A. Vermaas	Delft University of Technology
	Ahmadreza Rahbari	Delft University of Technology

An electronic version of this thesis is available at http://repository.tudelft.nl/.

TUDelft Delft
University of
Technology

ACRONYMS

Acronym	Definition
CAPEX	Capital Expenditure
CMS	Carbon Molecular Sieves
COSMO-RS	Conductor like Screening Model for Real Solvents
EoS	Equation of State
EHC	Electrochemical Hydrogen Compressor
FCEV	Fuel Cell Electric Vehicles
HEX	Heat Exchanger
HP	High Pressure
IL	Ionic Liquid
ILM	Immobilized Liquid Membranes
ISO	International Organization for Standardization
KF	Karl Fischer
NG	Natural Gas
OPEX	Operational Expenditure
PEM	Proton Exchange Membrane
PR	Peng-Robinson
PSA	Pressure Swing Adsorption
PV	Photovoltaic
SDS	Safety Data Sheet
SMIRK	Shell's Modified Intensified Redlich Kwong
SRK	Soave Redlich Kwong
TSA	Temperature Swing Adsorption
UN	United Nations
UNFCCC	United Nations Framework Convention on Climate Change
VLE	Vapor Liquid Equilibrium

CHEMICALS

Acronym	Definition
DEG	Diethylene glycol
TEG	Triethylene glycol
[EMIM][Acetate]	1-Ethyl-3-methylimidazolium acetate
[BMIM][Chloride]	1-Butyl-3-methylimidazolium chloride
[EMIM][Ethyl sulfate]	1-Ethyl-3-methylimidazolium ethyl sulfate
[BMIM][Octyl sulfate]	1-Butyl-3-methylimidazolium octyl sulfate

ABSTRACT

Renewable energy projects, such as wind and solar (PV) parks, are rapidly being built to replace fossil fuel based energy sources. The major drawback of electricity production from renewable sources is that they are intermittent and therefore lead to a mismatch between the supply and the demand of energy. Energy storage in the form of hydrogen production is a potential candidate to overcome this problem. However, due to its low volumetric energy density, hydrogen must be compressed to use it for storage or transportation purposes. HYET BV has developed an Electrochemical Hydrogen Compressor (EHC) that is capable of compressing hydrogen up to P = 1000 bar, and have the potential of bringing compression costs down to 3 kWh/kg. As the compressed hydrogen is saturated with water, it must be dehydrated before it is used for refuelling Fuel Cell Electric Vehicles (FCEV), as the ISO 14687-2:2012 standard has limited the water concentration to 5 μmol water per mol gas mixture.

In this work, a landscaping study was performed to search for potential drying methods, including membrane separation, adsorption, absorption and cooling. To select the best method for hydrogen dehydration, it is essential to have a good understanding of the thermodynamics at the given pressure conditions, beginning with the saturated water content in compressed hydrogen. To the best of our knowledge, the only experimental data describing the water content in the H_2-H_2O mixture for pressures exceeding 300 bar are from 1927 and are limited to T = 323.15K [J. Am. Chem. Soc., 1927, 49, pp 65-78]. In this thesis, it was concluded that conventional Equations of State (EoS) failed to predict the equilibrium coexistence compositions of the liquid and gas phase. Therefore, molecular simulations were used, which adequately predicted the water content in compressed hydrogen.

The second part of this thesis was to select the best drying method for hydrogen dehydration. Previous work showed that absorption using Ionic Liquids (IL) could be an interesting alternative to traditional drying methods. Therefore, absorption experiments were performed on the ILs 1-Ethyl-3-methylimidazolium acetate [EMIM][Acetate], 1-Butyl-3-methylimidazolium chloride [BMIM][Chloride], and 1-Butyl-3-methylimidazolium octyl sulfate [BMIM][Octyl Sulfate] to test the feasibility of ILs for hydrogen dehydration. The ILs were selected on stability, safety, and on the activity coefficient of water in the given IL. The experiments showed that ILs can be used as an absorbent to dry hydrogen gas. A part from the initial selection criteria, the experiments showed that surface tension is an important criterion for future IL selection, as it is strongly related to foam production. Finally, the very hygroscopic ILs tested turned out to be capable of absorbing large amounts of water, but a lot of energy was required to regenerate the ILs, making them less attractive as a potential absorbent.

CONTENTS

1

INTRODUCTION

In 2015, The United Nations (UN) agreed on reducing the world-wide greenhouse gas emissions. As a result, 195 members of the United Nations Framework Convention on Climate Change (UNFCCC) signed the agreement that aims to keep the global average temperature increase to well below 2°C, aiming for 1.5°C, above pre-industrial levels [1]. On top of that, the UN has set 17 sustainable development goals for 2030 to end poverty and hunger worldwide [2]. As access to energy is a key enabler to defeat poverty, the worldwide energy demand is expected to grow by 40% by 2040 [3]. To achieve the UN sustainable development goals, while simultaneously reducing greenhouse gas emissions, new forms of energy sources are needed. Fossil fuels, such as coal, oil, and natural gas, are currently accountable for 80% of the total primary energy supply [3] and renewable energy projects, such as wind and solar (PV) parks, are rapidly being built to replace fossil fuels. It is expected that 40% of the total generated electricity will be generated from renewable energy sources in 2040 [3].

However, cheap electricity production from renewable sources is only a part of the solution. The other part is to integrate this electricity into the existing electricity grid. In the first place, electricity production from renewable sources, like wind and solar (PV), are intermittent and therefore lead to a mismatch between supply and demand of energy [4]. To close this gap between supply and demand, energy storage is required [5, 6]. In the second place, transporting electrons over large distances is expensive. When distances become significant (>hundred kilometers), it becomes cheaper to transport molecules through a pipe rather than to transport electrons through a power cable [7]. This holds even more where natural gas infrastructures are already in place [7].

Hydrogen is a potential candidate to overcome both problems [7, 8], as hydrogen can be used to reproduce electrons via fuel cells, for heating or as a raw material for the chemical industry [4, 9]. The major drawback of hydrogen is the low volumetric energy density at room temperature and atmospheric pressure. To use hydrogen for storage or transportation, the density must be increased significantly [10]. One possible way to do this is cryogenic cooling. However, hydrogen has a boiling temperature of 20.25K, which makes this process very energy intensive. The other option, which is most common at the moment, is gaseous compression. For instance, pressurized gaseous hydrogen is typically stored in Fuel Cell Electric Vehicles (FCEV) at $P = 350$ bar or $P = 700$ bar [10]. Such a tank has a capacity of around 100 to 150 litres and stores 4 to 6 kg of hydrogen, which provides a range of approximately 500 km [10]. High pressure storage tanks are installed at refueling stations that temporary store the hydrogen up to 1000 bar. This high pressure is required to fill the hydrogen tank within the target time of 3 to 5 minutes [10].

Currently, hydrogen gas is compressed at refueling stations, using mechanical compressors. These conventional compressors, including piston, compressed air, diaphragm, or ionic compressors, require an average of 6 kWh/kg of energy to compress hydrogen from 10 to 400 bar [11]. The required compressors at refueling stations typically have a low throughput and a high pressure ratio. Under these constraints, the efficiency of mechanical compressors drop significantly. Furthermore, mechanical compressors require a lot of maintenance and produce a lot of noise, which is a problem on locations where acoustical emission is a constraint [12].

An emerging alternative compressor is the Electrochemical Hydrogen Compressor (EHC). It has no moving parts and therefore does not require a lot of maintenance and operates fully silent [12]. HYET BV has developed an EHC that has the potential of bringing compression costs down to 3 kWh/kg [11]. A pressure level

1

of 1000 bar was achieved at the compressor outlet. This shows that HYETT's EHC is capable of compressing to the desired pressure level of a refueling station storage tank. The working principle of an EHC operation is similar to a Proton Exchange Membrane (PEM) fuel cell [13]. The compressor consists of a number of stacks in parallel, where every single stack consists of a low pressure and a high pressure side, separated by a membrane that is only permeable for hydrogen protons and not for molecules. The membrane is positioned between two platinum catalysts containing electrodes. In Fig. 1.1, the working principle of the EHC is shown. Just like a fuel cell, a potential difference over the electrodes splits a hydrogen molecule into two protons that are transported through the membrane. However, unlike a fuel cell where hydrogen forms water with an oxygen molecule, the protons are here reformed to hydrogen molecules at elevated pressures [12]. The reactions are presented below in Eqs. (1.1) to (1.3) [12]:
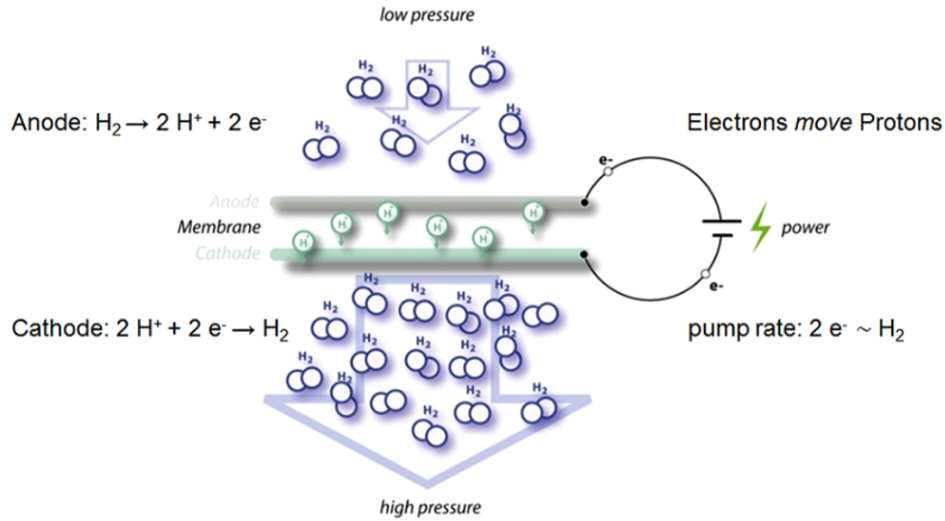

Figure 1.1: Working principle of an Electrochemical Hydrogen Compressor (EHC). Source: HYET BV.

$$\text{Anode} \quad H_2^{LP} \rightarrow 2H^+ + 2e^- \tag{1.1}$$

$$\text{Cathode} \quad 2H^+ + 2e^- \rightarrow H_2^{HP} \tag{1.2}$$

$$\text{Overall} \quad H_2^{LP} \rightarrow H_2^{HP} \tag{1.3}$$

The EHC has several advantages compared to traditional technologies. Apart from the higher efficiency, especially at high compression ratios [12], low maintenance requirements, and fully silent operation. From an electrochemical point, the compression ratio could be infinitely large. Only back diffusion of hydrogen from high to low pressure, is limiting higher pressure ratios [12]. Furthermore, due to the highly selective membrane, the compressor can also operate as a purifier, since other molecules than H_2 are not able to pass the membrane. Finally, the EHC is very well suited to scale up, due to its limited size [12]. A drawback of the EHC, which is comparable to that of a fuel cell, is high material costs. Mainly the platinum catalyst, which is required to resist the corrosive environments in the compressor, is very expensive [12]. Another disadvantage is that the resulting hydrogen gas is saturated with water. This water comes from the membrane that is always hydrated. This is because water enables the transport of protons through the membrane. This causes a problem for FCEV applications, as the maximum water content in hydrogen used for PEM fuel cells in road vehicles, is 5μmol water per mol hydrogen fuel mixture [14]. This maximum water content is described in Table 1 of the ISO 14687-2:2012. The International Organization for Standardization (ISO) states that water provides a transport mechanism for water-soluble contaminants such as K^+ and Na^+ when present as an aerosol [14]. For conventional compressors, it is better to remove water prior to compression, as water can damage the compressor and it accumulates as a liquid, due to the pressure increase. However, water removal prior to compression is not applicable to EHC, as the output gas is saturated with water. Therefore, the hydrogen gas needs to be dehydrated at high pressure.

1.1. RESEARCH OBJECTIVES

A landscaping study, described in Chapter 2, was performed to search for potential drying methods, including membrane separation, adsorption, absorption and cooling. The most common methods to dehydrate gases are adsorption and absorption. This is elaborated on in Chapter 2. To select the best method for hydrogen dehydration, it is essential to have a good understanding of the thermodynamics at the given pressure conditions, beginning with the saturated water content in compressed hydrogen. Unfortunately, there are very little experimental data available on the Vapor Liquid Equilibrium (VLE) of the H_2-H_2O system at elevated pressures. To the best of our knowledge, the only experimental data describing the water content in the H_2-H_2O mixture for pressures exceeding 300 bar are from 1927 (limited to T = 323.15K) [15]. Therefore, thermodynamic modeling was required to determine the water content in compressed hydrogen, resulting in the first objective of this research:

1) Determine the water content in compressed hydrogen up to 1000 bar, in the temperature range of 0°C to 70°C.

In parallel, the different drying methods were evaluated on their feasibility to dry hydrogen gas at high pressures. Previous studies showed that absorption using Ionic Liquids (IL) could be an interesting alternative to traditional drying methods [16–19]. However, there has been no work produced on the use of ILs as a drying agent for hydrogen dehydration. Therefore further research was required to test the feasibility of using ILs as an absorbent. This resulted in the second objective:

2) Test the feasibility of Ionic Liquids for high pressure hydrogen dehydration.

1.2. APPROACH

WATER CONTENT IN COMPRESSED HYDROGEN

Chapter 3 describes different thermodynamic models to calculate VLE of H_2-H_2O systems. In industrial applications, the most common method is to use cubic Equations of State (EoS), because of their simplicity [20, 21]. First the Peng-Robinson (PR), Soave Redlich Kwong (SRK), and Shell's Modified Intensified Redlich Kwong (SMIRK) EoS were used to predict the water content at elevated pressures. The predicted compositions of both the liquid and the vapor phase, calculated using all the different EoS, were not in good agreement with the available experimental data. Since the conventional EoS failed to describe the VLE of the H_2-H_2O system at elevated pressures, more physically based models were required. SAFT types EoS are more physically based, but they still require a temperature dependent binary interaction parameter k_{ij} [22]. Due to the lack of experimental data at high pressure, it is not possible to fit such a parameter. Therefore, force field based molecular simulations were used to study the phase coexistence of the H_2-H_2O system. These molecular simulations showed excellent agreement with experimental data and resulted in the paper from [Rahbari, Brenkman, and co-workers.] [23], attached in Appendix B.

IONIC LIQUIDS AS DRYING AGENT

To test the feasibility of ILs as a drying agent, literature was consulted to see if ILs have been used for hydrogen dehydration before. Although no work applied the concept on hydrogen, some work described the use of ILs to dry natural gas [17–19], which is in many ways similar to hydrogen dehydration. Chapter 4 gives a brief description of ILs in general and on what criteria they should be selected on for hydrogen dehydration. To test the feasibility, preliminary experiments were executed, which are described in Chapter 5. Finally the results are discussed in Chapter 6.

2

DRYING METHODS

There are several methods to remove impurities from a gas stream [24]. An overview of different drying methods is provided in this chapter, including their pros and cons. As elucidated in the introduction, the required drying process is different from most conventional ones. Usually, gases are purified before they are compressed. In this case, an Electrochemical Hydrogen Compressor (EHC) is used, which causes the hydrogen gas to leave the compressor saturated with water. Therefore, it does not make sense to dry the hydrogen prior to the compression stage, and the dehydration must take place at elevated pressures. Other specific constraints for this project are the required purity and the small scale of the unit.

- **Pressure**
  Present-day refueling stations use mechanical compressors, where water is removed from the hydrogen gas prior to the compression stage, as water could damage the compressor. Water is removed using pressure, or temperature swing adsorption [25]. If hydrogen is compressed using an EHC, it leaves the compressor saturated with water. Therefore one must dry the hydrogen at a pressure of 875 bar. Dehydration units are usually operated at low pressure, so this constraint challenges the existing technologies.

- **Purity**
  The desired purity of gases strongly depends on the application. If hydrogen is used for heating or industrial processes, it usually does not require a very low water content. For Fuel Cell Electric Vehicles (FCEV) however, hydrogen specifications are very strict [14]. One of the key constraints is the maximum water content in the pressurized hydrogen. The ISO standard requires a maximum water concentration of 5 ppm, with the following motivation [14]:

  "Water (H_2O*) generally does not affect the function of a fuel cell, however; it provides a transport mechanism for water-soluble contaminants such as* K^+ *and* Na^+ *when present as an aerosol. Both* K^+ *and* Na^+ *are recommended not to exceed 0.05 μmol/mol. In addition, water may pose a concern including ice formation for onboard vehicle fuel and hydrogen dispensing systems under certain conditions. Water should remain gaseous throughout the operating conditions of systems."*

  Since the temperature of the hydrogen gas increases significantly during refueling [26], it is not likely that ice formation occurs in the dispensing system or the hydrogen tanks. In the dispensing system the temperature of the hydrogen increases, because the Joule-Thomson coefficient at the pressure and the temperature conditions of refueling is negative [26, 27]. Therefore, the hydrogen gas enters the cylinder at an increased temperature. This temperature increases even further because of the compression of the gas inside the cylinder, which is called heat of compression [26]. Various studies have modeled and experimentally validated the temperature rise in hydrogen tanks during refueling [26, 28–30].

- **Footprint/Scale**
  The final application specific criterion is that the whole unit must be installed at a refueling station, instead of an industrial plant. Therefore the drying unit must have a small footprint and operate efficiently at low throughput.

Besides these project specific criteria, more general criteria are listed below:

- low energy use

- low hydrogen loss

- low Capital Expenditure (CAPEX) & Operational Expenditure (OPEX)

- low safety & environmental risks

2.1. OVERVIEW OF POSSIBLE DRYING METHODS

The considered methods are elaborated on in this section. Including membrane separation, adsorption, absorption, and cooling.

2.1.1. MEMBRANE SEPARATION

One of the possible methods for gas separation is membrane separation. The advantages over other methods include low cost for low volumes, high mechanical reliability due to simplicity of the operation, low energy costs and small footprint. Membrane separation is commercially available for dehydration of air and natural gas. The biggest obstacle for applying this technology for hydrogen dehydration is the required purity of the hydrogen gas. Polymeric membranes for example, which are commercially used for this application, achieved dew points down to -40°C at atmospheric pressure, which is not dry enough [31].

IMMOBILIZED LIQUID MEMBRANES

Immobilized liquid membranes (ILM) can overcome this problem, as they can achieve very high selectivities. ILMs are basically polymeric membranes, in which the pores are filled with an organic fluid. This increases the selectivity significantly and it has been demonstrated to work for removing water and other impurities from biogas. However, to reach this level of purity, multiple stages are required, resulting in a significant pressure drop [32]. Unfortunately, there are some obstacles with this method that need to be overcome before the technology can concluded to be feasible. Major problems are pressure drop, instability, flux decline and liquid phase evaporation [16]. Although ILM may be a promising candidate in the future, the technology is currently not ready.

CARBON MOLECULAR SIEVE MEMBRANES

Carbon Molecular Sieves (CMS) are another promising alternative for polymer mebranes. CMS membranes can be prepared by controlling the carbonization procedure during carbonization of a polymeric material. They can be designed for very specific applications and therefore achieve very high selectivities [33]. The main drawback of CMS membranes is that water can block the very small pores, blocking the transport of hydrogen molecules.

2.1.2. ADSORPTION

Adsorption is the adhesion of a molecule to the surface area of the adsorbent and is used to remove impurities in gases that have a low concentration of contaminants. The desired substance, in this case water, is adsorbed by an adsorbent that eventually becomes saturated and must be regenerated or replaced. There are several possibilities to regenerate the adsorbent [24]:

1. Temperature Swing Adsorption (TSA).
   The absorbed water is evaporated out of the adsorbent by increasing the temperature and purging the column with dry hydrogen or an inert gas.

2. Pressure Swing Adsorption (PSA).
   Vaporization of the water by decreasing pressure, often by creating vacuum. Just like TSA, dry hydrogen or an inert gas is used for purging.

3. Inert Purge Stripping (without changing T or P).
   When the adsorbent is saturated with water, an inert gas is used to vaporize the water out of the adsorbent, without changing the temperature or pressure.

4. Chemical desorption.
   A fluid that adsorbs water even more than the used adsorbent is used to retrieve the water from the adsorbent.

Inert purge stripping only works if the hydrogen input is relatively wet, resulting in a large difference in concentration between product gas and purge gas. That is clearly not the case here, so therefore inert purge stripping is not an option. Chemical desorption is most likely not effective due to the required purity of the hydrogen gas. The adsorbent must already be very hygroscopic, to achieve 5 ppm water content. Therefore, it is not likely that the adsorbent easily releases the adsorbed water to a chemical absorbent. In similar applications, TSA and PSA, or a combination of both, are typically used. They also proved to be capable of achieving the required level of purities. The major drawback of PSA for HP drying is the fact that it is not desirable to depressurize the adsorbent column. Re-pressurizing the column back to 875 bar costs a lot of time and energy. Fig. 2.1 shows a typical scheme of an adsorption unit, in this case TSA [34]. The drying unit consists of a minimum of two columns, often three. While one bed is drying the hydrogen, the other is regenerated. This is done by purging hot gas over the column. This gas could be dry hydrogen, or an inert gas.
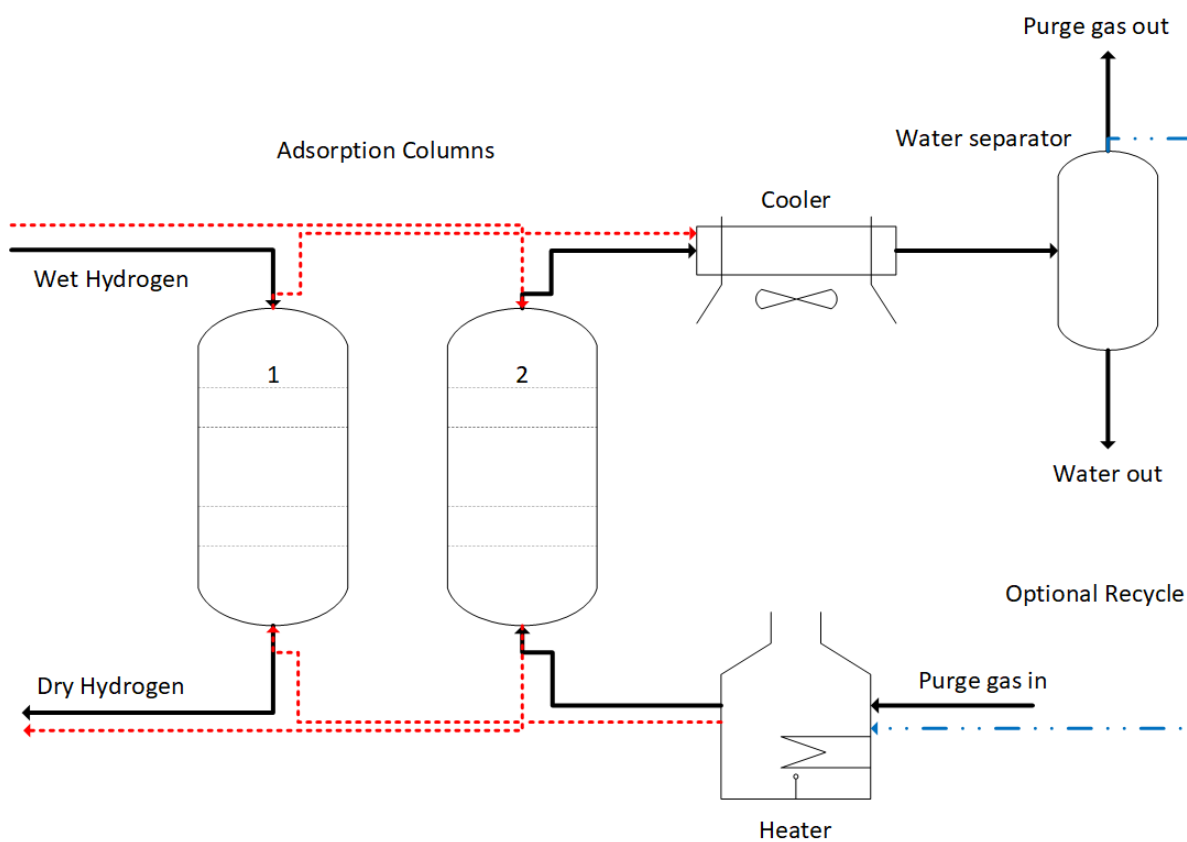
Figure 2.1: Schematic of a typical TSA unit. Solid lines indicate the formation where column 1 is used as adsorption column, and 2 is being regenerated. The dashed lines indicate the process when it is the other way around. In the adsorption column, wet hydrogen enters and leaves the column dehydrated. Heated purge gas enters the regeneration column and leaves it hydrated, to be cooled and separated from water. Hydrogen loss can be prevented by recycling the purge gas (indicated by the dotdashed line).

Commercially available adsorbent agents that absorb water are activated alumina, silica gel, and synthetic sodium or calcium aluminosilicate zeolites (molecular sieves). Literature shows that activated alumina and zeolites have been proven to work at high pressure, respectively at 3000 atm [35] and 5000 bar [36]. No damage of adsorbent or discontinuity in adsorption isotherms were reported. Silica gel, however, is affected by high pressures. Each time silica gel is compressed it gets granulated, which leads to destruction of the skeleton structure [25].

Adsorption, and in particular TSA, seems a very reasonable option for high pressure dehydration. It is capable of obtaining very low ppm levels of water content and can operate at high pressure. The major disadvantage

is that the efficiency is strongly related to the hydrogen throughput. At refueling stations, the capacity is relatively low, making this option less attractive.

2.1.3. Cooling
Condensing
The most straight forward method for reducing the water content in hydrogen gas is cooling the hydrogen until all water condenses. However, there is little known about the dewpoints, i.e. at what temperature the water condenses, of water at elevated pressures. Further research is required on the thermodynamics of high pressure H_2-H_2O systems, to see if condensing is a serious option. Nonetheless, even if condensing does not result in the desired level of purity, it could very well be a good pre-treatment method. The final bit of water can then be removed by one of the other methods, described in this chapter.

Freezing
It is also possible to cool the hydrogen gas even further, so that the water vapor will directly turn into ice, called deposition. This method would require two units, just like adsorption. In this case, such a unit will be a heat exchanger (HEX). Hydrogen gas is cooled well below zero °C, and the ice will build up in the HEX. When the HEX reaches the maximum ice level, it goes in regeneration mode and the other unit is used. Regeneration would simply mean heating the HEX, until all ice melts and the resulting water is removed. Disadvantages of this method are very much comparable to those for adsorption.

2.1.4. Absorption
The final drying method considered is absorption. In contrast to adsorption, where water is adsorbed by a solid agent, absorption consists of liquids that absorb water from the vapor phase. Absorption is already used for applications like natural gas dehydration, which is quite similar to hydrogen dehydration. In those cases, Diethyleneglycol (DEG) or triethyleneglycol (TEG) are used as absorbents. Fig. 2.2 shows a typical absorption unit [34]. The wet hydrogen is infused in the bottom of a tray column (left side of figure) and the dry absorbent flows in from the top. During the contact, the absorbent is enriched with water where after the water is boiled out in a heater (right side of figure). At elevated pressures, absorption can be favorable over adsorption, as

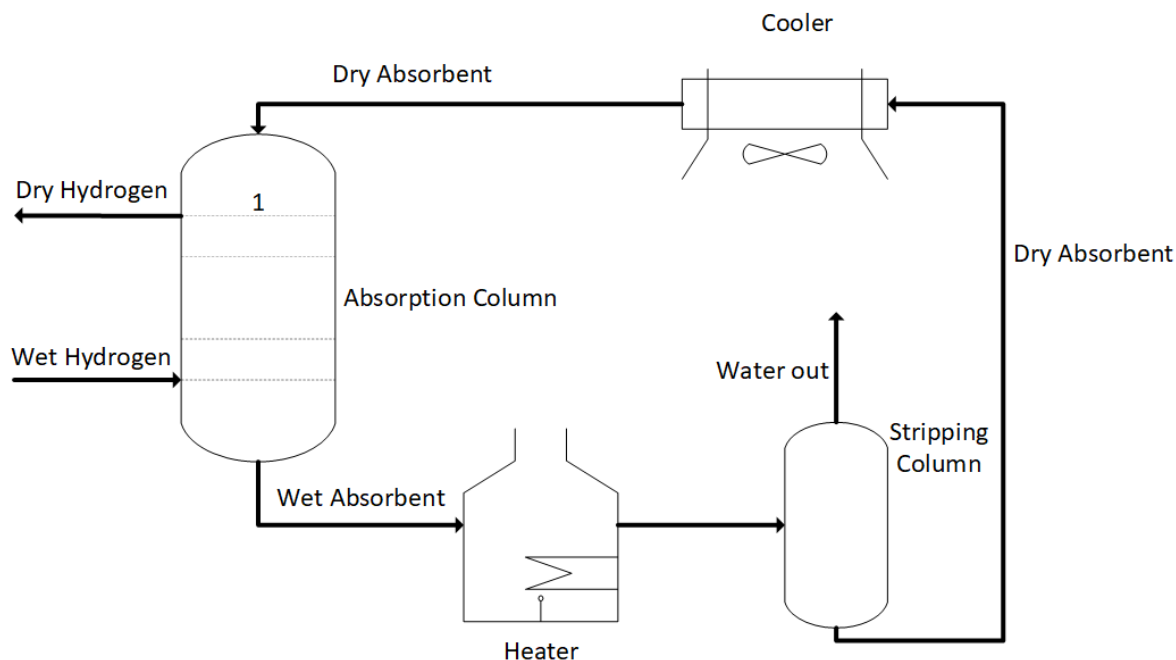Figure 2.2: Schematic of a typical absorption unit. The dry absorbent enters the absorption column and absorbs the water from the wet hydrogen gas. It leaves at the bottom where after it is heated and the water is stripped out the absorbent. Finally, the dry absorbent is cooled back and it re-enters the absorption column.

the absorption column does not need to be depressurized and no purge gas is required. Due to the high

pressure, it is also likely to achieve the required purities. However, just like TSA, absorption also becomes more efficient at higher flow rates. Another disadvantage is the contamination of the resulting hydrogen gas, due to evaporation of the absorbent.

IONIC LIQUIDS

The latter disadvantage can be overcome by using Ionic Liquids (ILs) instead of conventional absorbents like TEG. Because ILs practically have no vapor pressure, contamination of the hydrogen gas by evaporation of the absorbent is prevented. A few studies have shown that absorption using ILs could potentially work for natural gas dehydration [17, 19]. To the best of our knowledge, no literature exists that describes the use of ILs for hydrogen dehydration.

2.2. METHOD SELECTION

To select the best method for high pressure hydrogen dehydration, pros and cons of the different methods were tested against the criteria stated in Chapter 2. To the best of our knowledge, no previous work described the use of membranes that were capable of drying gases to a water content below 5 ppm, especially at elevated pressures. Therefore, this method is no longer considered for hydrogen gas dehydration. Note that membranes can improve in the future, making this option interesting again.

The three other methods are, based on the three main criteria, expected to be capable of drying hydrogen gas at the given pressures to the required purity.

- Adsorption is the most obvious method to go for, as it is most commonly used to remove contaminants at low concentrations from gases. Previous work showed that adsorption systems are capable of drying gases at elevated pressure [37]. PSA, which is the most efficient method based on mass transfer, requires decompression of the adsorption column, which is not favorable. TSA is an alternative option that does not require depressurization of the columns. However, the mass transfer to the purge gas is less efficient with TSA and therefore this process requires much more purging gas. Even if this purging gas is recycled, all this gas needs to be heated and cooled back again. Currently HyET uses a TSA in a demo-unit that has a hydrogen gas loss of 20%. Although this can be reduced significantly, TSA will unavoidably lead to a substantial hydrogen loss, or an efficiency reduction of the entire compressor unit, due to recycling of the purge gas.

- Absorption has the major advantage that the absorbent can be pumped out the absorption column, without decompressing the column. Therefore, only a single column is needed; this reduced number of components is favorable at low volumes. The absorbent can be regenerated separately, by reducing pressure and/or increasing temperature. This does not require a purge gas, resulting in hydrogen loss or energy loss due to recycling. The major risk related to absorption is vaporization of the absorbent. This is a concern, especially due to the strict specifications of the hydrogen gas [14]. Ionic Liquids are a potential solution to this problem, as they have practically no vapor pressure. Table 2.1 shows the vapor pressures of water, Triethylene Glycol (TEG), which is the most commonly used absorbent, and six hygroscopic ILs [19]. To the best of our knowledge, no previous studies exist that used ILs to dehydrate hydrogen gas. Previous studies also concluded that ILs are promising as absorbent, which makes it an area that needs more research [25, 38]. Therefore, this work focuses on testing the feasibility of ILs to dehydrate hydrogen gas.

Table 2.1: Vapor pressures of several liquids.
(a): calcuted using Wagner equation

Liquid	Vapor Pressure / (Pa)
Water	$7.0 \times 10^{4\,(a)}$
TEG	2.4×10^{1} [38]
[choline][glycolate]	2.5×10^{-5} [19]
[DMIM][DMPO$_4$]	2.5×10^{-6} [19]
[EMIM][MeSO$_3$]	3.9×10^{-8} [19]
[BMIM][BF$_4$]	1.5×10^{-8} [19]
[EMIM][Et(EG)$_2$SO$_4$]	7.5×10^{-9} [19]
[EMIM][EtSO$_4$]	7.0×10^{-9} [19]

- The final method is cooling the hydrogen gas, until all water is condensed or frozen out. This is especially interesting for refueling applications, because the refueling protocol currently requires precooling. The reason for this is that the temperature of hydrogen increases as it is filled in a vehicle tank [39] and the temperature in the tank may not exceed 85°C [40]. To determine if cooling is the best method to dry the hydrogen gas, it is essential to know the saturated water content in compressed hydrogen at different temperatures and pressures. Unfortunately, as mentioned in the introduction, there are very little experimental data on the water content in high pressure hydrogen. Therefore, prior to comparing the three different methods, the first part of this work is focused on calculating the saturated water content in hydrogen gas.

3

THERMODYNAMICS

3.1. INTRODUCTION

As stated in Chapter 2, it is crucial to know the water content in compressed hydrogen at different temperatures, to compare different drying methods. First, the water content of the hydrogen gas that leaves the EHC is needed. In this specific application, hydrogen leaves the compressor at a pressure of 875 bar and temperatures ranging from 35°C to 40°C. Thereafter the water content at lower temperatures is required, to see if cooling is a viable option. Will it be possible to remove the excess water by condensing it, or could this be at least a part of the solution? The first major part of this thesis project was to determine the water content in the compressed hydrogen, at different conditions. The saturated water content is the maximum amount of water vapor that can be present in compressed hydrogen, before the water condenses. This chapter describes different methods to calculate the Vapor Liquid Equilibrium of hydrogen and water at high pressure conditions. The calculated data are compared to experimental data. Due to the high pressure range, no VLE experiments in this range were executed. At these conditions, the ideal gas law and the ideal mixing rules do no longer apply [41].

3.2. EXPERIMENTAL DATA

For the VLE, both the liquid phase and the vapor phase composition need to be studied. Therefore, experimental data for both the solubility of hydrogen in water and the concentration of water vapor in compressed hydrogen are relevant. Fig. 3.1 shows all available data for water vapor in compressed hydrogen [15, 42–45]. Unfortunately, very little data are available for the water content in hydrogen for pressures exceeding 300 bar. The only paper is from Bartlett [15], who measured the water vapor in compressed hydrogen at 50°C. In that paper there are only three data points (400/600/1000 atm.) higher than 300 bar. The most common method for VLE calculations, is to fit an Equation of State (EoS) on available data. Since there are little data available at high pressure conditions, the fitted EoS must be extrapolated, which is not very reliable.

3.3. THE GAMMA/PHI FORMULATION OF VLE

The simplest equation for VLE calculations is applying Raoult's law. Application of Raoult's law acquires two major assumptions[46]:

- The vapor phase is considered an ideal gas (ideal gas law applies).

- The liquid phase is an ideal solution.

It is obvious that both assumptions do not apply for the given application. The ideal gas law does not hold, as pressures are very high (950 bar). Fig. 3.2 shows the density of hydrogen, calculated using the ideal gas law, and the density from RefProp®[1] [27]. The increasing error shows that when the pressure increases, hydrogen can no longer be treated as an ideal gas. At 100 bar and 50°C the compressibility factor Z already shows an error of 6% compared to the ideal gas law ($Z = 1$) [27]. Since this error increases drastically for the output

---

[1]Refprop® is a program, developed by the National Institute of Standards and Technology, that calculates the thermodynamic properties of industrially important fluids and their mixtures [27].
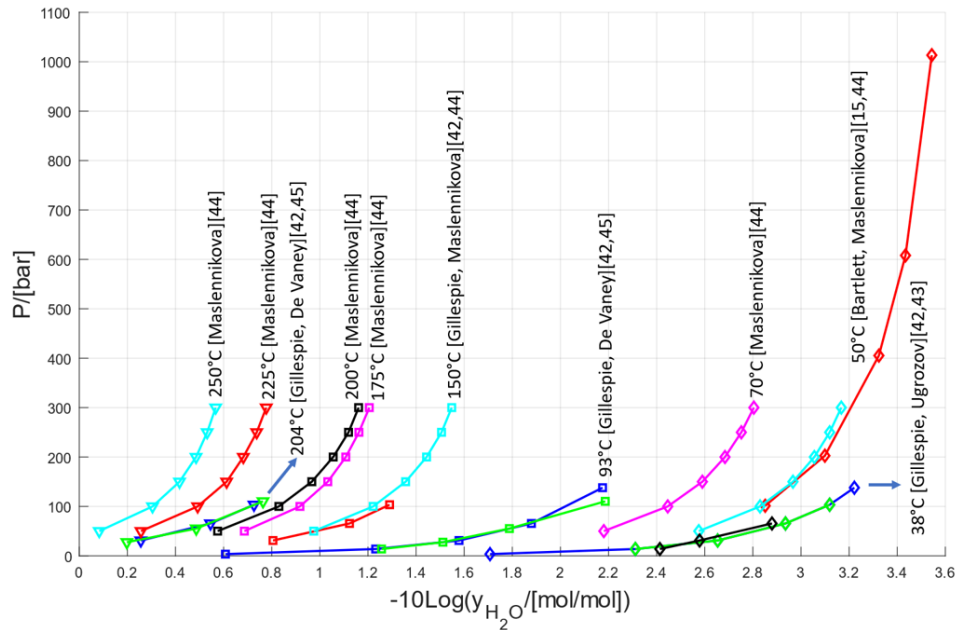
Figure 3.1: Available experimental data of the water content in compressed hydrogen, at temperatures between 0°C and 250°C [15, 42–45].

pressure of the EHC, the ideal gas law can not be used. Furthermore, water is a polar molecule and hydrogen is not, which implies that they are not chemically similar and the liquid phase can therefore not be treated as an ideal solution. Two common approaches for calculating Vapor Liquid Equilibrium data are the $\gamma - \phi$
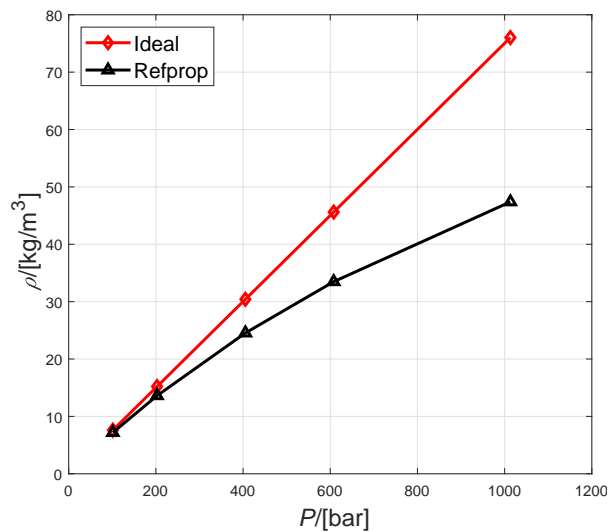
Figure 3.2: Density of hydrogen as a function of pressure, at a temperature of 50°C. Predicted using ideal gas law(diamonds), and densities from RefProp® [27] (triangles).

formulation and the $\phi - \phi$ formulation. The $\gamma - \phi$ method is the traditional approach that requires an activity coefficient of water in the liquid mixture γ_{H_2O}. This formulation is based on the fact that the fugacity in the liquid phase is equal to the fugacity in the vapor phase, which is derived from the chemical potential [41]:

$$\hat{f}_i^V = \hat{f}_i^L, \tag{3.1}$$

where the hat indicates that it concerns a property of a substance in a mixture. The fugacity can be interpreted as the pressure, corrected for the non-idealities. Thus, for an ideal gas, the fugacity is equal to the

pressure. The fugacity coefficient Φ is the ratio of the fugacity to the pressure:

$$\Phi = \frac{f}{P} \tag{3.2}$$

The vapor phase fugacity of a component in a mixture is:

$$\hat{f}_i^V = \hat{\Phi}_i y_i P. \tag{3.3}$$

The fugacity coefficient of a component in a mixture $\hat{\Phi}_i$ should not be confused with the fugacity coefficient of a pure component Φ_i. The latter varies only with temperature and pressure, while the former also varies with the composition of the mixture. Section 3.4.2 describes different EoS to find $\hat{\Phi}_i$. The liquid phase fugacity of a component in a mixture is [46]:

$$\hat{f}_i^L = \gamma_i x_i \Phi_i^{sat} P_i^{sat} \exp\left[\frac{V_i(P - P_i^{sat})}{RT}\right], \tag{3.4}$$

where γ_i is the activity coefficient of i in the solution, Φ_i^{sat} is the fugacity coefficient of the pure component at saturated pressure and V_i is the liquid molar volume of the pure component i. The exponential part of the equation is called the Poynting factor. The Poynting factor corrects for the compressibility effects within the liquid. This factor is usually neglected, as it is equal to 1 at low to moderate pressures. Since pressures are very high in this work, it can not be neglected. Fig. 3.3 shows the Poynting Factor at 50°C and for different pressures. At pressures close to 1000 bar, the Poynting factor is almost 2. Combining Eqs. (3.3) and (3.4) into
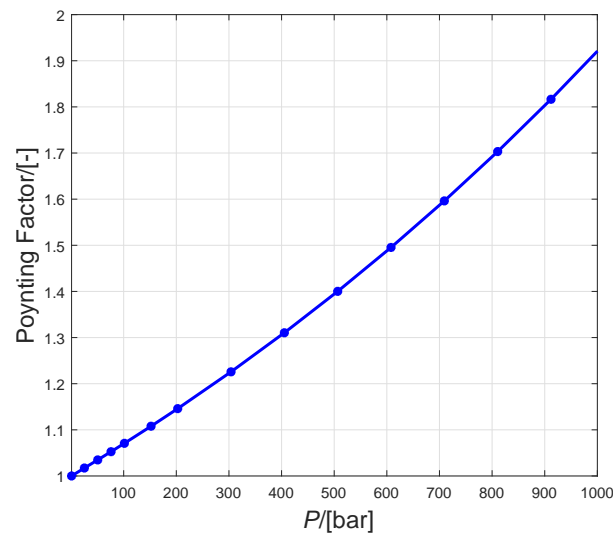
Figure 3.3: Poynting Factor, as a function of pressure, at 50°C.

Eq. (3.1) gives the $\gamma - \phi$ formulation:

$$\hat{\Phi}_i y_i P = \gamma_i x_i \Phi_i^{sat} P_i^{sat} \exp\left[\frac{V_i(P - P_i^{sat})}{RT}\right] \tag{3.5}$$

The detailed derivation of the $\gamma - \phi$ formulation is described in [Smith *et al.*]. P_i^{sat} is the saturated vapor pressure of water and is calculated with the Wagner equation [47]:

$$\ln(P_r^{sat}) = (a\tau + b\tau^{1.5} + c\tau^3 + d\tau^6)/T_r{}^2 \tag{3.6}$$

Where $P_r^{sat} = P^{sat}/P_c$ is the reduced saturated vapor pressure, $T_r = T/T_c$ is the reduced temperature, and $\tau = 1 - T_r$. Since hydrogen can not be liquefied at temperatures above the critical temperature ($= 32.98K$), the saturated vapor pressure of hydrogen can not be calculated at the required temperatures.

---

[2]The last two exponents are different for water than for other substances.

3.4. CUBIC EQUATIONS OF STATE (EoS) FOR VLE CALCULATIONS

In industrial applications, the most commonly used method to describe VLE systems is using cubic Equations of State (EoS). This section elaborates on different EoS to describe the VLE of the H_2-H_2O system. These EoS can be used to describe pure components, but combined with mixing rules, they can also describe properties of components in mixtures. The performance of each cubic EoS, used in this work, to describe the VLE of the H_2-H_2O system will be evaluated. To give a better description of real gases, so where the compressibility factor $Z \neq 1$ [46], extra parameters are required to describe the system using an EoS. These parameters are component specific, based on the critical pressure and temperature of that component. These parameters are typically a function of the reduced temperature $T_r = T/T_c$. An EoS that describes both gases and liquids must be at least cubic in V. These cubic EoS are widely used and can be formulated in a general form [47]:

$$P = \frac{RT}{v-b} - \frac{\Theta(v-\eta)}{(v-b)(v^2+\delta v+\epsilon)} \tag{3.7}$$

$$\Theta = a \cdot \alpha(T_r) \tag{3.8}$$

where $a, b, \eta, \alpha(T_r), \delta, \epsilon$ differ for different cubic EoS. For all EoS applied in this work $\eta = b$.

3.4.1. DENSITY CALCULATIONS

PENG-ROBINSON EOS

To make the parameters dependent on temperature, an alpha function is introduced. This alpha function does not only vary with temperature but also introduces a third component specific parameter: the acentric factor ω. This parameter corrects for the assumption that all fluids, when compared at the same reduced temperature and reduced pressure, have the same compressibility factor [46]. The Peng-Robinson (PR) equation is as follows (it is described in detail in [Lin and Daubert][48]):

$$P = \frac{RT}{v-b} - \frac{a \cdot \alpha(T_r)}{v(v+b) + b(v-b)} \tag{3.9}$$

$$a = \frac{0.45724(RT_c)^2}{P_c} \tag{3.10}$$

$$b = \frac{0.0778RT_c}{P_c} \tag{3.11}$$

$$\alpha(T_r) = (1 + (0.37464 + 1.54226\omega - 0.26992\omega^2)(1 - T_r^{1/2}))^2 \tag{3.12}$$

Eq. (3.12) is the regular alpha function for PR. However, there are some small variations of this function optimized for specific applications.

SOAVE'S MODIFIED REDLICH KWONG EOS

Soave's modified Redlich Kwong (SRK) EoS is a variation on the more famous Redlich Kwong EoS. It is known to perform well with respect to the vapor phase.

$$P = \frac{RT}{v-b} - \frac{a \cdot \alpha(T_r)}{v(v+b)} \tag{3.13}$$

$$a = \frac{0.42724(RT_c)^2}{P_c} \tag{3.14}$$

$$b = \frac{0.08664RT_c}{P_c} \tag{3.15}$$

$$\alpha(T_r) = (1 + (0.480 + 1.574\omega - 0.176\omega^2)(1 - T_r^{1/2}))^2 \tag{3.16}$$

Shell Modified Improved Redlich-Kwong (SMIRK) EoS

The SMIRK-EoS is a 2-parameter Redlich-Kwong type EoS where not only $a \cdot \alpha$, but also b is made a function of temperature in order to extend its applicability [49]. Both a and b have the following form [49]:

$$Y = y_1 + y_2 \ln[1 + \exp(y_3(X - y_4))] - y_5 \ln[1 + \exp(-y_3(X - y_4))] \tag{3.17}$$

where: $Y = a$ or b
         y_i = coefficient of the a- or b-function
         $X = T_c / T$

The a- and b- parameters are obtained from regression of vapor pressures and liquid molar volumes along the saturation curve (VLE) of pure components [49]. Since the details of the SMIRK-EoS are not within the scope of this thesis, the reader is referred to the work of Drexhage, J.J. and Welsenes, for further details. Shell developed their own software tool STFlash® for thermodynamic flash calculations including VLE, which is based on Shell thermodynamic methods and parameter databased including the SMIRK EoS. SMIRK results in this work are obtained by using this tool.

Density Results

Fig. 3.4 shows the densities of liquid water and hydrogen gas, which are predicted by the various EoS, compared to data from Refprop® [27]. As expected, cubic EoS perform poorly in describing liquid densities using conventional EoS. Only the SMIRK-EoS gives acceptable results, as Fig. 3.4a shows. However, it starts to deviate more as the pressure increases. Also note that the SMIRK-EoS is already fitted to available experimental data. The vapor phase of hydrogen, however, is well described using this EoS.

(a) water in the liquid phase

(b) Hydrogen in the vapor phase
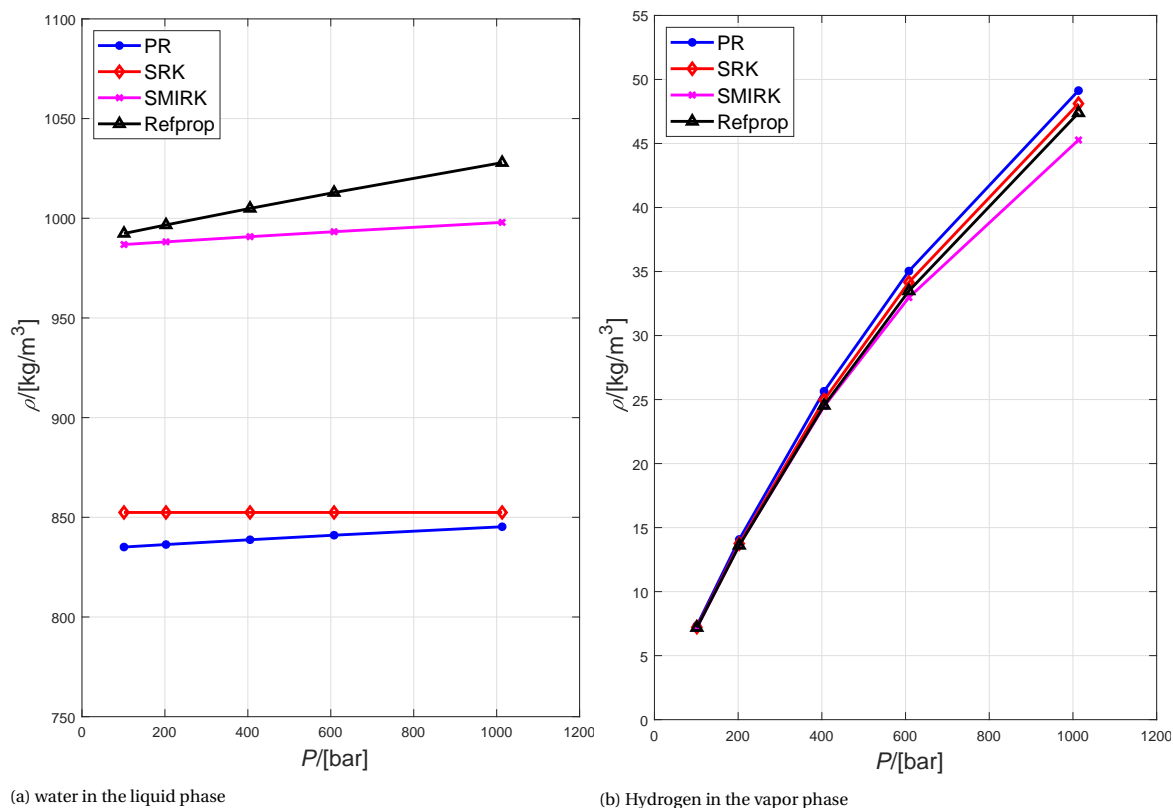
Figure 3.4: Densities of liquid water (a) and hydrogen gas (b) at 50°C, as a function of pressure. Predicted by EoS; PR (circles), SRK (diamonds), SMIRK (squares), compared to experimental data from Refprop® (triangles) [27].

3.4.2. Fugacity Coefficient calculations

The fugacity and the fugacity coefficient depend on the temperature, pressure, and on the composition of the mixture. The challenge in calculating the fugacity coefficients of components in mixtures is that the fugacity depends on all mole fractions of all components in the mixture. All components have different interactions with each other. To account for these interactions, mixing rules are introduced.

MIXING RULES

There are several ways to describe the dependence of different components with different mole fractions. The most common mixing rule is the van der Waals mixing rule that uses a quadratic dependence between components [50].

$$a_{\mathrm{m}} = \sum_i \sum_j x_i x_j a_{ij} \tag{3.18}$$

$$b_{\mathrm{m}} = \sum_i x_i b_i \tag{3.19}$$

where a_{m} and b_{m} are the EoS parameters for the mixture, x is the mole fraction of each component in the specific phase. Note that a_{ii} and a_{jj} are parameters corresponding to a pure component, while a_{ij} and $a_{ji}(i \neq j)$ are called unlike-interaction parameters that describe the interaction between the components:

$$a_{ij} = (1 - K_{ij})(a_i a_j)^{1/2} \tag{3.20}$$

where

$$K_{11} = K_{22} = 0 \qquad \& \qquad K_{12} = K_{21} = k_{ij} \tag{3.21}$$

k_{ij} is called the binary interaction parameter, which is determined by fitting EoS results to experimental data. As mentioned above, there are more complex mixing rules that also contain more interaction parameters. In this work, the van der Waals mixing rules were applied for the PR and SRK EoS.

PENG-ROBINSON EoS

The equation for the fugacity coefficient, predicted by the PR EoS, is [48]:

$$\ln(\hat{\Phi}_i) = \frac{b_i}{b_m}(Z_m - 1) - \ln(Z_m - B_m) -$$
$$\frac{A_m}{2\sqrt{2}B_m} \left(\frac{2\sum_j y_i a_{ij}}{a_m} - \frac{b_i}{b_m} \right) \ln \left(\frac{Z_m + (1+\sqrt{2})B_m}{Z_m - (1-\sqrt{2})B_m} \right) \tag{3.22}$$

where

$$A_m = \frac{a_m P}{R^2 T^2} \tag{3.23}$$

$$B_m = \frac{b_m P}{RT} \tag{3.24}$$

$$Z_m = \frac{P v_g}{RT} \tag{3.25}$$

v_g is the specific volume that is calculated by solving Eq. (3.9).

SOAVE'S REDLICH KWONG EoS

The equation for the fugacity coefficient, predicted by the SRK EoS, is [48]:

$$\ln(\hat{\Phi}_i) = \frac{b_i}{b_m}(Z_m - 1) - \ln(Z_m - B_m) - \frac{A_m}{B_m} \left(\frac{2\sum_j y_i a_{ij}}{a_m} - \frac{b_i}{b_m} \right) \ln \left(1 + \frac{B_m}{Z_m} \right) \tag{3.26}$$

SMIRK-EoS

The fugacity coefficients, predicted by the SMIRK-EoS, are again calculated using STFlash®. By default, the SMIRK method uses the Second Michelsen-Huron-Vidal GExcess mixing rule [51]. This mixing rule uses 4 parameters that are fitted to experimental data. Since these parameters are fitted to a small set of data across a relatively narrow range of pressure and temperature, it is not reliable to use these fitted parameters for extrapolation.

Fugacity Coefficient Results

Fig. 3.5a shows the water content in the H_2-H_2O mixture, calculated with the different EoS, compared to experimental data. This is calculated by substituting Eqs. (3.3) and (3.4) in Eq. (3.1), resulting in Eq. (3.27) for the water fraction in the vapor mixture. Here the binary interaction parameter is not fitted to experimental data. Referring to Section 3.4.2, this means that $k_{ij} = 0$. For the SMIRK-EoS, this is slightly different, as it uses a 4-parameter mixing rule. In this case all four parameters are set to zero. Fig. 3.5b shows the fugacity coefficients $\hat{\Phi}_{H_2O}$ of water in the H_2-H_2O mixture, which follows directly from the fugacity coefficient equations.

$$y_{H_2O} = \gamma_{H_2O} \, x_{H_2O} \, \frac{\Phi^{sat}{}_{H_2O} P^{sat}_{H_2O} \exp\left[\frac{V_{H_2O}(P - P^{sat}_{H_2O})}{RT} \right]}{\hat{\Phi}_{H_2O} P} \tag{3.27}$$

Note that the amount of water dissolved in the liquid phase x_{H_2O} if negligible for this equation and therefore assumed to be equal to one. Accordingly, as $x_{H_2O} \rightarrow 1$, the activity coefficient of water γ_{H_2O} also goes to one. Activity coefficient models have been used to calculate γ_{H_2O} and calculate x_{H_2O} by iteration, but it did not make any significant difference.

(a) Water content in the H_2-H_2O mixture in the vapor phase.

(b) Fugacity coefficients of water in the H_2-H_2O mixture in the vapor phase.
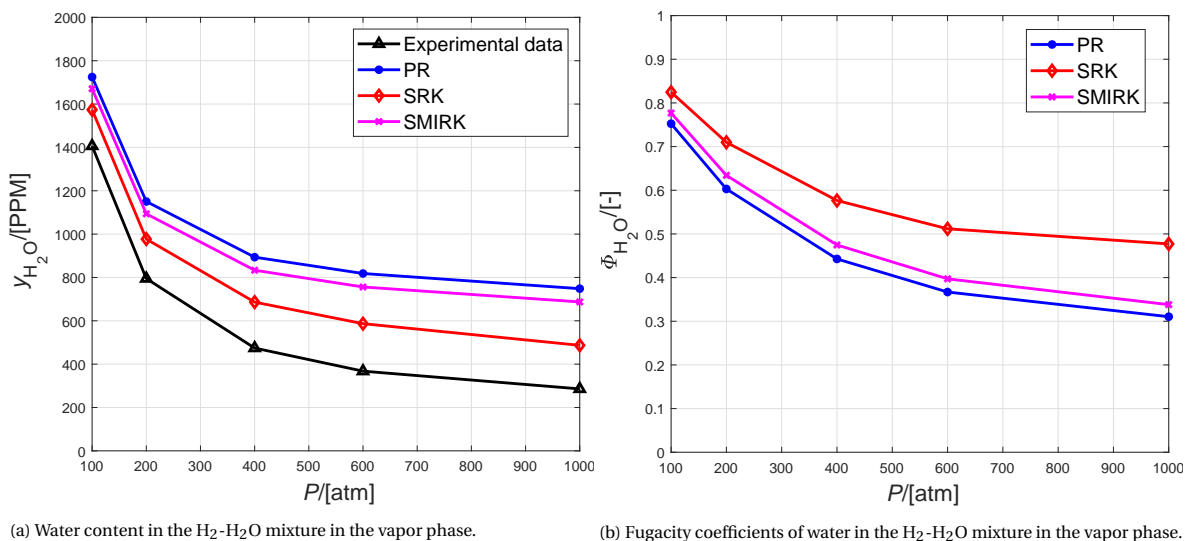
Figure 3.5: Water content (a) and fugacity coefficient of water (b), as a function of pressure, at a temperature of 50°C. Calculated using PR-EoS (circles), SRK-EoS (diamonds) and SMIRK-EoS (x-mark), compared to experimental data (triangles) [15]. ($k_{ij} = 0$)

Fig. 3.5 clearly shows that the experimental data are not accurately described by the different EoS. In these calculations, the binary interaction parameter k_{ij} is equal to zero. The next step is to fit k_{ij} to experimental data to see if better results are obtained. The parameter is gradually increased, until it results in an accurate fit with the experimental data. For the SMIRK-EoS, the 4 interaction parameters, implemented in STFlash®, are used. Fig. 3.6 shows the fugacity coefficients and the water content fitted to the experimental data. In this figure k_{ij} is increased to 0.35, so that SRK fits with the experimental data. This value is very high for a binary interaction parameter. k_{ij} is used to make minor corrections in the a-function of the EoS. If this value becomes very high (normal range is between -0.1 & 0.1), the a-function is not correct for this system at these high pressure conditions. For the PR EoS, the binary interaction parameter needs to be increased even further, in order to fit with the available data.

Different Temperatures

Although the fitted binary interaction parameter is very high and therefore not physical as explained in Section 3.4.2, we also fitted this parameter to experimental data at other temperatures. Fig. 3.7 shows the water content, predicted by the SRK-EoS and the SMIRK-EoS, compared to experimental data. For the SRK-EoS a binary interaction parameter $k_{ij} = 0.35$ is used and for SMIRK-EoS a more complex mixing rule, mentioned in Section 3.4.2, is applied. Note that both SRK-EoS and SMIRK-EoS predict the water content accurately at temperatures near 50°C, but as temperature increases, so do the errors. For SRK-EoS, this is not a surprise, as the interaction parameter is fitted to experimental data at 50°C. The complex mixing rules used in SMIRK-EoS, however, do not perform much better, as the predictions are very similar to SRK-EoS. It could well be

(a) Water content in the H_2-H_2O mixture in the vapor phase.

(b) Fugacity coefficients of water in the H_2-H_2O mixture in the vapor phase.
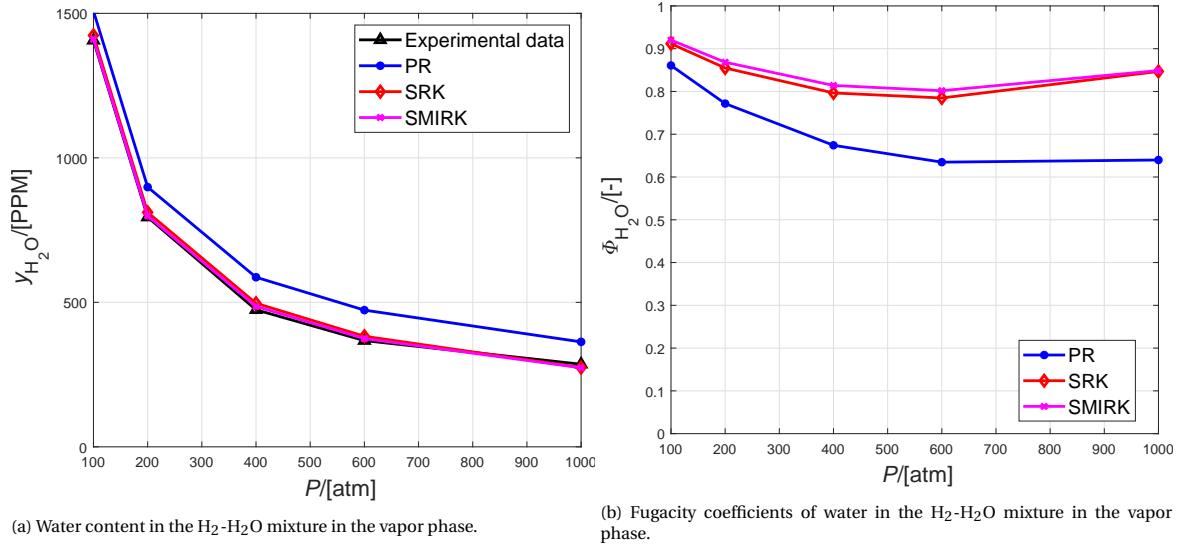
Figure 3.6: Water content (a) and fugacity coefficient of water (b) in the H_2-H_2O vapor mixture, as a function of pressure, at a temperature of 50°C. Calculated using PR-EoS (circles), SRK-EoS (diamonds) and SMIRK-EoS (x-mark), compared to experimental data (triangles) [15]. ($k_{ij} = 0.35$)

possible that this EoS is also only fitted on the data at 50°C, but this is hard to find out. Even though a binary interaction parameter of $k_{ij} = 0.35$ is already very high, k_{ij} is fitted to all experimental data at different temperatures, with the purpose of finding k_{ij} as a function of temperature. Fig. 3.8 shows the predicted water content, where k_{ij} is fitted to every single temperature. Fig. 3.9 shows the parameters at different temperatures. It shows that, for $T > 100°C$, the binary interaction parameter seems very random and nowhere near acceptable values. It is therefore not possible to find a temperature dependence of k_{ij}, based on the available data. Especially in the low temperature domain ($T < 38°C$), which is of particular interest, no experimental data are available and therefore it is not possible to predict the water content in this domain using a conventional EoS. In the work of [Rahbari, Brenkman, and co-workers.], the fitted parameters were also tested for the liquid phase [23]. These parameters predicted the solubility of hydrogen in the liquid phase even worse than without a k_{ij}.
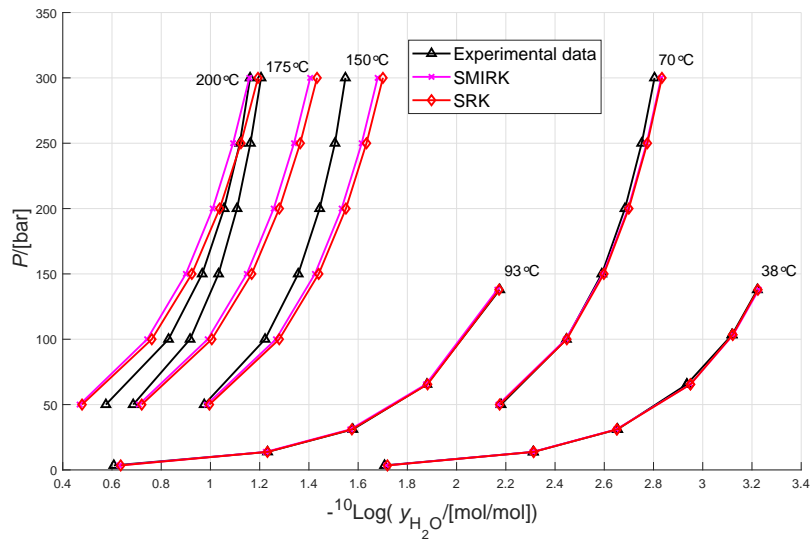
Figure 3.7: Water content in the H_2-H_2O vapor mixture, as a function of pressure, at different temperatures. Calculated using SRK-EoS (diamonds) and SMIRK-EoS (x-mark), compared to experimental data (triangles) [42–44]. ($k_{ij} = 0.35$)
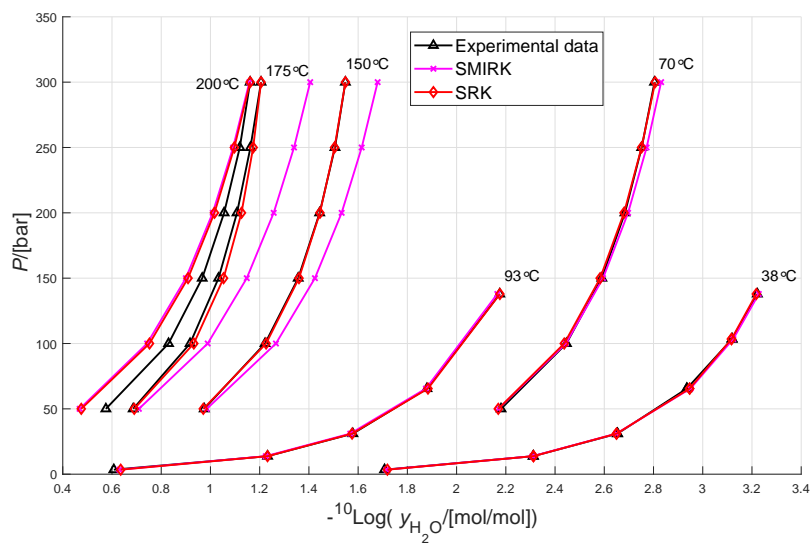
Figure 3.8: Water content in the H_2-H_2O vapor mixture, as a function of pressure, at different temperatures. Calculated using SRK-EoS (diamonds) and SMIRK-EoS (x-mark), compared to experimental data (triangles) [42–44]. (k_{ij} fitted at every temperature (see Fig. 3.9))
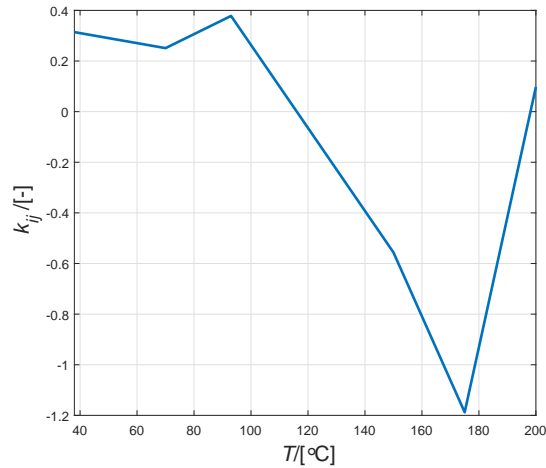
Figure 3.9: Binary interaction parameter k_{ij}, as a function of temperature, fitted to experimental data.

3.5. MOLECULAR SIMULATION

The results in Section 3.4, clearly show that the PR and SRK EoS are not capable of describing the H_2-H_2O system at elevated pressures. The SMIRK-EoS only shows good results in the temperature range where it is been fitted on experimental data. In this work, PR-EoS and SRK-EoS are used with the classical mixing rules. An improvement of these conventional EoS, could be to use mixing rules that take the polarity of the water molecule into account [21]. Another option is to use a more physically based equation of state, like a SAFT-EoS [52]. However, Sun *et al.* showed that a temperature dependent k_{ij} is still required [22]. Molecular simulations are also physically based, but do not require a temperature dependent parameter. For this study, molecular simulations are used to determine the water content in compressed hydrogen at different temperatures. These simulations resulted in the work of [Rahbari, Brenkman, and co-workers.], which accurately describes the used method and results [23].
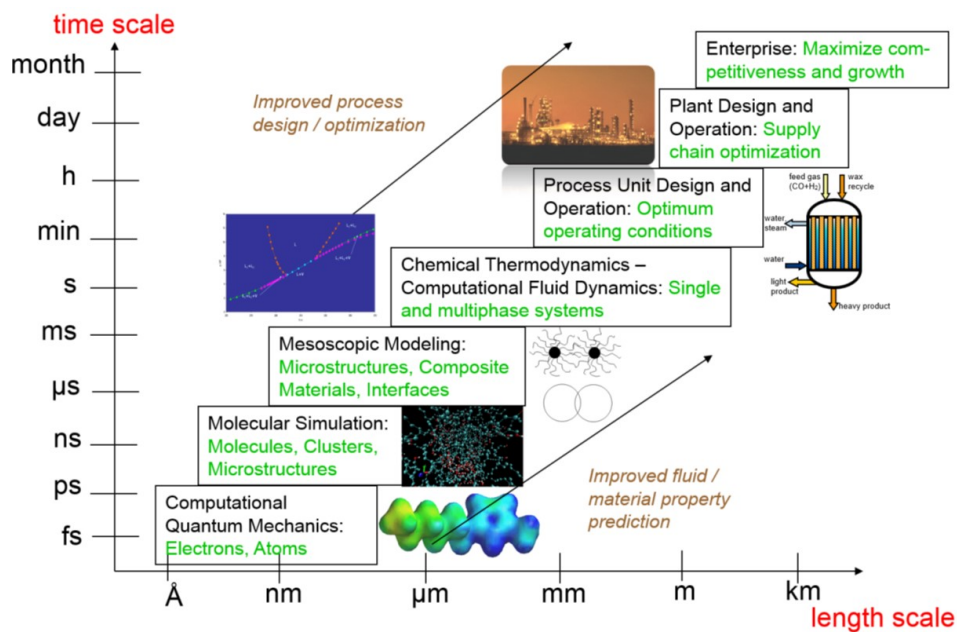
Figure 3.10: An overview of different modelling methods, based on their time and lenth scale. Source: T.J.H. Vlugt.

Fig. 3.10 shows the different scales of the modeling methods. Using cubic EoS, one can predict macroscopic properties of a given system using only a few parameters, at low computational cost. In many cases cubic EoS perform really well. Therefore, they are most commonly used in industry [21]. Especially if abundant experimental data is available, EoS are very reliable. The well known drawback is that the cubic EoS with conventional mixing rules are not accurate for liquid density calculations or other thermodynamic properties of complex fluids [21]. Therefore a k_{ij} is always required, which is unfavorable due to the lack of experimental data. Furthermore mixing rules that for instance take polarity into account need to be modified [21]. Moving more to the bottom left of the figure, one finds modeling methods that are based on the physical structure of single molecules, rather than entire systems. Molecular simulations take into account interactions between the molecules in the system and can predict macroscopic properties of the entire system, using statistical mechanics. To simulate the VLE of the H_2-H_2O system using molecular simulations, two boxes are created that are filled with both molecule types. One box represents the liquid phase, the other box the vapor phase. The interaction between molecules is based on the forcefields, selected for the specific molecules. Typically, random configurations of the H_2-H_2O system are generated, proportional to Boltzmann distribution, and sampled using the Monte Carlo method. The Boltzmann distribution is a probability distribution that indicates how likely it is that a given sample represents the real state of that system. For instance, if two molecules overlap in the simulation, the internal energy becomes infinitely high. This results in a probability of zero, meaning this sample is not used to calculate thermodynamic properties. Using this method, only favorable configurations are used to predict properties like density and the chemical potential. Note that this approach can not be used to calculate transport properties. Predicting transport properties requires molecular dynamics, which is not included in this work. For every molecule, multiple forcefields are available. The performance of the forcefield depends on the required properties and conditions of the given application. In this study, the forcefields were selected on their prediction results of the pure components at high pressure. The Marx [53] force field shows the best agreement with experimental data for hydrogen and the TIP3P [54] predicts the chemical potential of water in good agreement with experimental data from Refprop®[27]. For the comparison between the results with different forcefields, the reader is referred to the work of [Rahbari, Brenkman, and co-workers.] [23], which is attached in Appendix B.

3.5.1. Molecular Simulation Results

Fig. 3.11 shows the molecular simulation results. The results for the water content in the vapor phase are in excellent agreement with the experimental data. The simulations are overpredicting the solubility of hydrogen in the liquid phase. Fortunately, these predictions are not essential for the given HP drying application. The water content in the vapor phase is slightly overpredicted at low pressures, and marginally underpredicted at high pressures. Fig. 3.12 clearly shows this overprediction at 100 atm and 50°C. The figure shows a very good agreement at elevated pressure, which is the relevant pressure range for this work. The molecular simulations are a significant improvement for the EoS. However, further improvements could be made to reduce the over- and under predictions. This can be done by including the polarity of the water molecule, which is not included in the selected forcefield. At 10°C and 1000 bar, the water content is only 29 ppm. It would be interesting to simulate even lower temperatures and higher pressures. Possibly a saturated water content of 5 ppm can be achieved, meaning no further drying steps are required. It should be noted that the model does not include ice formation, so it is questionable how reliable the results are at temperatures close to 0°C.

(a) vapor phase   (b) liquid phase
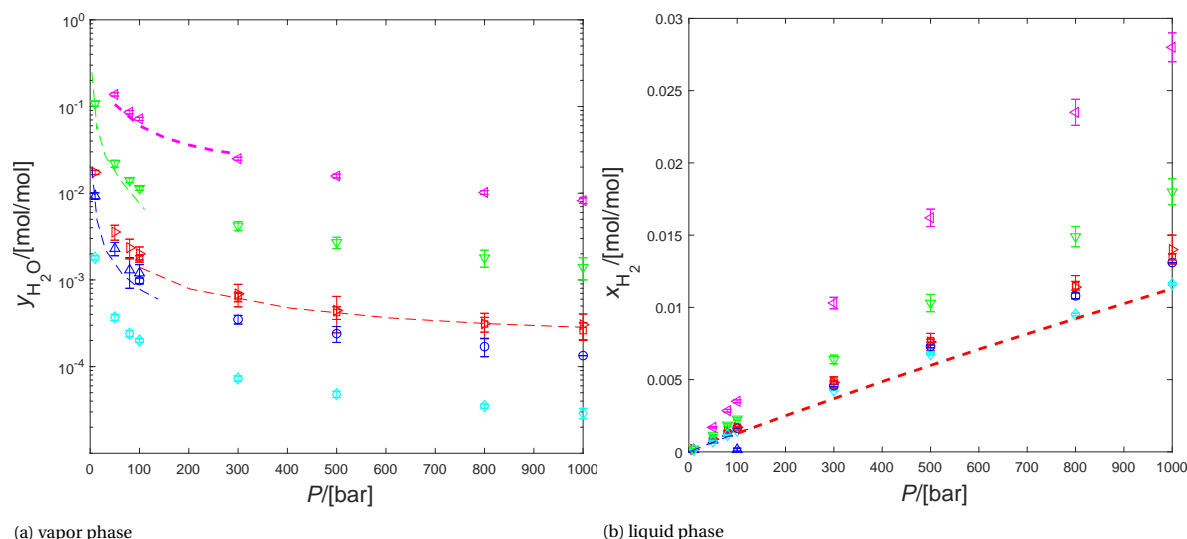
Figure 3.11: Vapor Liquid Equilibrium of the H_2-H_2O system, plotted as the water content in the vapor phase as a function of pressure at different temperatures(a), and the solubility of hydrogen in the liquid phase as a function of pressure at different temperatures (b). Applied force fields are TIP3P[54] for water and Marx[53] for water. Both the GE(triangles) and the NPT(diamond, circle, square) are applied. Simulated temperatures are: T = 283K (cyan), T = 310K (blue), T = 323K (red), T = 366K (green), T = 423K (magenta).
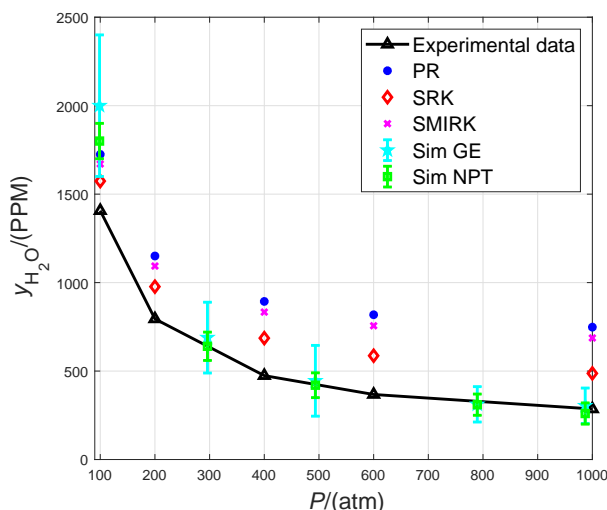
Figure 3.12: Water content in the H_2-H_2O vapor mixture, as a function of pressure, at a temperature of 50℃. Calculated using PR-EoS (circles), SRK-EoS (diamonds), SMIRK-EoS (x-mark), Molecular simulations (Gibbs ensemble (stars) and NPT ensemble (squares)), compared to experimental data (triangles) [15].

3.5.2. GAS-GAS IMMISCIBILITY

At very high pressures, something called gas-gas immiscibility, can arise [55]. Usually, gases become more immiscible at increasing pressure and decreasing temperatures. The simulations clearly show this effect, as the saturated water content decreases drastically with increasing pressure and decreasing temperature. However, in some supercritical mixtures, the vapor phase can split in two separate phases [55]. As pressure is increased or temperature decreased, the vapor phase can split in two phases with different compositions. For the H_2-H_2O system, this can result in a higher saturated water content [56, 57]. Fig. 3.13 shows this effect. Following the red arrow in Fig. 3.13, the miscibility initially decreases, but after the minimum in temperature it increases again. The blue arrow follows the same process for pressure.
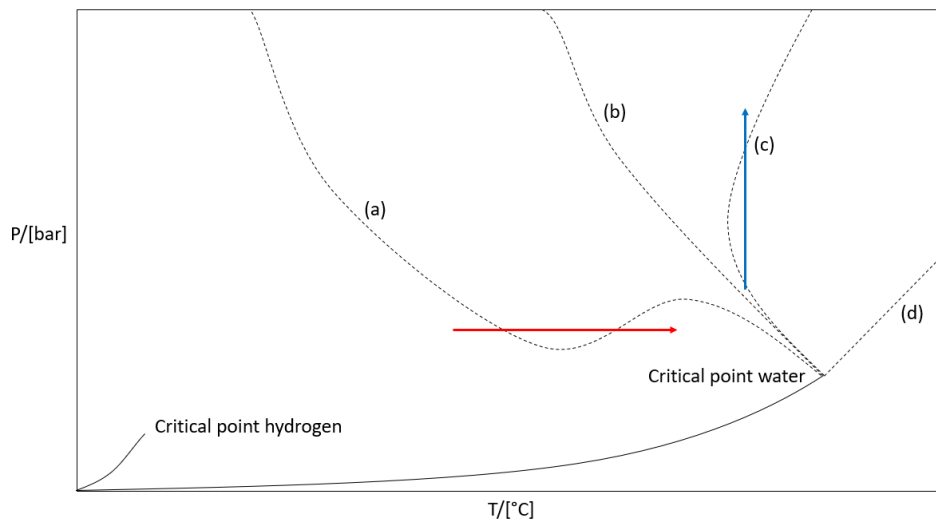
Figure 3.13: $P-T$ diagram of the H_2-H_2O mixture, including four possible critical lines (dashed lines) of the H_2-H_2O mixture. The trend from (a) to (d) indicates the increasing immiscibility [55]. The red arrow indicates a temperature increase at constant pressure, the blue arrow a pressure increase at constant temperature. Both processes go through a peak in immiscibility, as explained above.

There are two kinds of gas-gas immiscibility, first and second kind, shown in Fig. 3.14. For the first kind (Fig. 3.14a), gas-gas immiscibility occurs at the lowest temperature, while the second kind (Fig. 3.14b) has a temperature minimum in the critical line. For further details, the reader is referred to the work of Rowlinson *et al.*[55] and Seward and Franck[56]. Gas-gas immiscibility is not described by the performed molecular simulations. Therefore, although the molecular simulations are a very good prediction tool, experiments are needed to validate the model.

(a) First kind

(b) Second kind
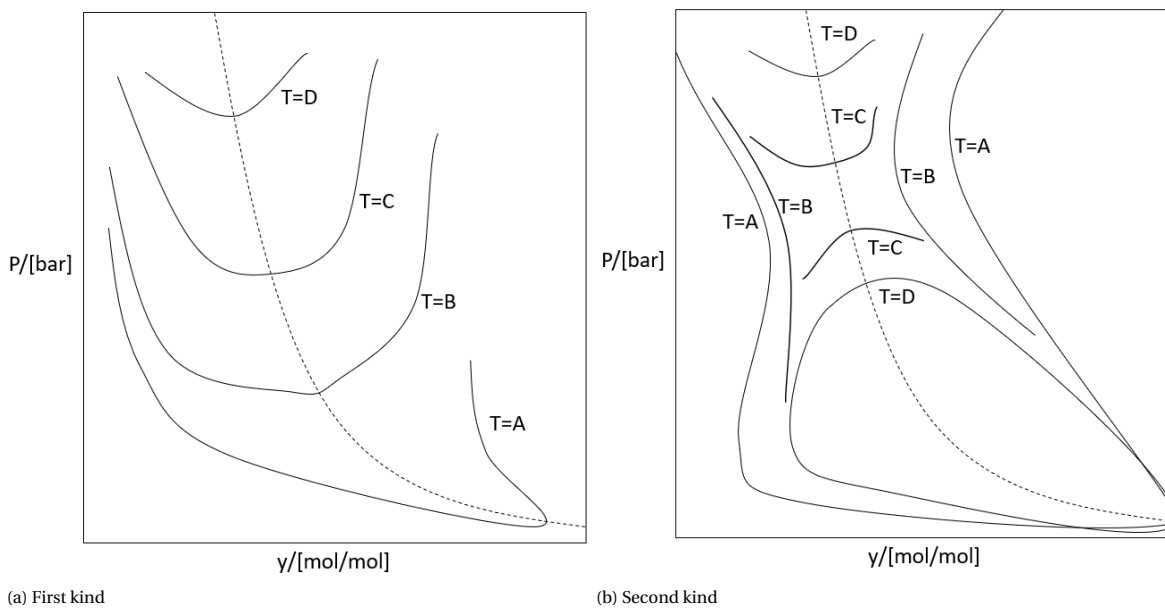
Figure 3.14: $P-y$ diagrams of typical mixtures where gas-gas immiscibility of the first kind (a) and second (b) kind occurs. The temperature increases form A to D. The critical locus is shown dashed [55]. At certain pressures and temperatures, the mixture shows gas-gas immiscibility, meaning that the vapor phase splits in two different vapor phases with different compositions.

<div style="text-align: right; font-size: 3em; font-weight: bold;">4</div>

IONIC LIQUIDS

4.1. INTRODUCTION

As mentioned in Section 2.1.4, Ionic Liquids (ILs) are promising alternative absorbents for hydrogen dehydration, mainly because of there negligible vapor pressure. This chapter gives a brief description of ILs in general, the different classes of ILs and their properties. Although there is no strict definition for ILs, the general way to define them is [58]:

"An Ionic Liquid is a salt with a melting point below 100°C".

Ionic liquids consist of an organic cation and (often) an inorganic anion. They are also referred to as room temperature ILs or molten salts. The number of cations and anions that can be combined is high, resulting in an endless amount of possible combinations. ILs are classified into different groups, depending on the cation. Fig. 4.1 shows five well-known classes: Imidazolium, Pyridinium, Quaternary Ammonium, Tetra Alkylphosphonium and Pyrrolidinium [59].

(a) Imidazolium (b) Quaternary Ammonium (c) Pyrrolidinium (d) Pyridinium (e) Tetra Alkylphosphonium
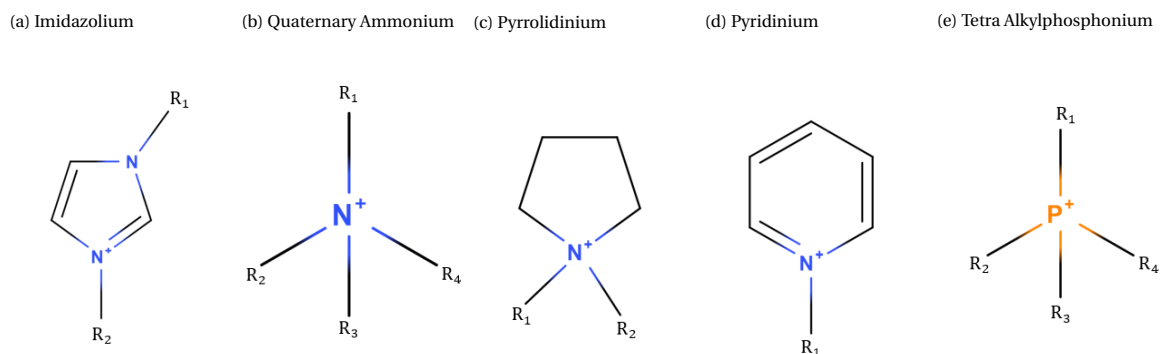
Figure 4.1: An overview of the five most well-known IL classes. ILs are categorized based on their cation.

Ionic liquids are used for various applications, such as catalysis, synthesis, electrochemical devices, lubricants, and absorbents [60]. The possible use of ILs as an absorbent for some molecules, like CO_2 capture, has been studied very widely [61–64]. To the best of our knowledge, no previous work describes the use of ILs to dehydrate hydrogen gas. However [Yu *et al.*, Han *et al.*, Krannich *et al.*, Heym *et al.*] describe systems were ILs are used as an absorbent to dry natural gas, which is a physically similar process. Therefore some data is available describing the solubility of water in different ILs. Water and hydrogen do not have a similar chemical structure. The main difference is that water is polar and hydrogen not. Therefore, absorbents that are very well suited for water absorption, show a very low solubility of H2 at similar conditions [66, 67].

4.2. IONIC LIQUID SELECTION

Due to the numerous possible combinations of cations and anions, it is challenging to select the IL that is the best for this specific application. The selection can be narrowed down, as they should at least satisfy the following constraints:

1. Hygroscopic

2. Negligible vapor pressure

3. Water/Hydrogen/thermally stable

Unfortunately, little experimental data are available on ILs and there is a countless number of them. The alternative way to select ILs, in the absence of experimental data, is thermodynamic modeling. There are a few possible methods available for predicting IL properties. Several studies have shown accurate density and viscosity predictions for various ILs [68, 69], validated with experiments. However, these volumetric properties are not decisive for selecting the best IL for this application. Referring back to the $\gamma-\phi$ formulation, described in Section 3.3, efficient drying is achieved if the water content in the vapor phase y_{H_2O} is low, while the water content in the liquid phase x_{H_2O} is high. The only parameter that varies with a different IL is the activity coefficient of water γ_{H_2O} in that particular Ionic Liquid. A low activity coefficient means that the IL can absorb a larger amount of water at a constant water content in the vapor phase. However, as the drying process is a repeating cycle, a low γ_{H_2O} is only desirable if the IL is also capable of releasing the water again at other conditions. This results in a more detailed description of the desired hygroscopic capability of the IL:

1. The activity coefficient should be low enough to dry the hydrogen gas to a water content of 5 ppm.

2. The difference in the activity coefficient, between absorption mode and regeneration mode, is preferably as large as possible.

The latter determines the amount of water that the IL actually can absorb; this does not take into account the water in the IL that is not removed in the regeneration mode and will permanently be present. While the activity coefficient is of large importance for the selection, previous studies show that it is hard to model properties without having any experimental data to fit on [17]. Possible methods to predict the activity coefficients are COSMO-RS, (Modified) UNIFAC and Molecular Simulation.

4.2.1. (MODIFIED) UNIFAC

UNIFAC is the most commonly used group contribution method for the prediction of activity coefficients in non-ideal mixtures [70]. Group contribution methods subdivide a molecule into functional groups. While the thermodynamics of the system were originally based on interactions between the different molecules, it is now reduced to interactions between these functional groups, which are assumed to be independent of each other [71]. The thermodynamic properties of mixtures can be calculated by adding up all interactions, depending on the temperature, pressure and composition. The full method is explained in detail by Fredenslund *et al.* [70]. Unfortunately, the original UNIFAC method has a few disadvantages. It is not possible to accurately describe VLE data and excess enthalpies simultaneously. Therefore, the temperature dependency of the activity coefficient can not be described correctly [72]. The newer modified UNIFAC (Dortmund) method solves this problem by implementing the temperature dependent parameters. These parameters are fitted simultaneously to a large (Dortmund) database, covering the temperature dependency of the activity coefficients [72]. However, the modified UNIFAC does not eliminate the largest disadvantage of these group contribution methods. The described methods always need at least a few experimental data to fit the required group interaction parameters [71]. Therefore, the selection of ILs, using this method, is limited to ILs that have experimental data available. However, due to the countless possibilities of ILs, a method is required that does not need this kind of data. COSMO-RS gives a good solution, as it does not rely on fitted parameters.

4.2.2. COSMO-RS

Conductor like Screening Model for Real Solvents (COSMO-RS) is a method, based on quantum mechanics, that can predict chemical potentials in liquids [73]. Properties, such as the activity coefficient, can be derived from the chemical potential. Analogously to the group contribution methods, properties are predicted by modeling the interactions between molecules. However, instead of dividing the molecules into functional groups, the molecule structure is simplified to its outer surface [71]. The molecular surface is subdivided into

surface segments, with equal surface areas, that interact with each other. The surface is simulated by a sigma (σ) profile. A sigma profile is the probability distribution of such a segment having a specific charge density [74]. The main advantage of COSMO-RS is that, if one has a correct sigma profile of the pure component, no fitted interaction parameters are necessary. This method is therefore very well suited for the selection of a wide variety of different potential ILs, which have no experimental data available. Although COSMO-RS does not require fitted parameters that describe interactions between different molecules, a few element-based parameters are still required [71]. Therefore, experimental data are still needed to get the surface charge density profile of a pure element right. Furthermore, COSMO-RS captures only approximately ion-dipole interactions, which are existing in this system due to the water-ion interactions. During the course of this project, we approached a company that provides a tool that includes COSMO-RS calculations. Initial predictions using COSMO-RS were executed and compared to the available experimental data [75]. Fig. 4.2 shows these predictions, using three different sets of parameters, and it also includes the experimental data [75]. Based on Fig. 4.2, the following conclusions were drawn:

1. The predicted activity coefficients vary strongly with the used element specific parameters. Without comparing it to experimental data, this already indicates that the used parameters are of much importance.

2. The COSMO-RS predictions show a large deviation with respect to the experimental data. This deviation increases at low water fraction. While COSMO-RS clearly shows a minimum at infinite dilution, the experimental data show that this minimum is somewhere between 0.7-0.8 mole fraction.

3. The temperature dependency of the activity coefficient, predicted by COSMO-RS, is opposite to the experimental data. The predictions suggest that the activity coefficient increases with temperature, while the experiments show that it is the other way around.

Unfortunately, the COSMO-RS predictions show that COSMO-RS also needs some fitting to experimental data, to get reliable results. Previous studies mainly use COSMO-RS on a qualitative basis instead of on a quantitative basis [17, 18, 76–78]. Although COSMO-RS could be used to get a relative understanding of how ILs behave compared to other ILs, it can not be used to validate activity coefficients that follow from experiments. For this reason, we chose not to go ahead with COSMO-RS.

4.2.3. MOLECULAR SIMULATION
The third method to predict IL properties is using molecular simulations, like we used for the VLE of H_2 and H_2O. The working principle of molecular simulation methods is described in Chapter 3. The major drawback of this method is that it requires a lot of time and manual work for every molecule that needs to be simulated. Therefore it is not a very efficient method for screening a large amount of ILs. When an IL is selected though, molecular simulations can be very useful to precisely predict properties like activity coefficients. Molecular simulations for IL systems have not been used in this work, but they could be a useful tool for future work.

4.2.4. LITERATURE AND AVAILIBILITY
The objective of this study is to test the feasibility of hydrogen gas drying, using Ionic Liquids. In this phase of the project, it is not required, nor expected to find the optimal IL. Based on the challenges associated with property prediction, a more pragmatic approach is followed for the IL selection. We first created a long-list of ILs, based on the following:

1. Section 4.1 already mentioned the previous work on testing ILs for natural gas dehydration [17–19, 65]. The ILs used in these works are also interesting for this work, as the process is physically quite similar.

2. As mentioned in Section 4.2.1, Modified UNIFAC is the most commonly used method to predict activity coefficients. It only works though, if interaction parameters are available. The Dortmund Data Bank (DDBST [79]), that provides the worlds largest factual data bank, was used to check which interaction parameters between water and different ILs were included in the data bank. All the Ionic Liquids that belonged to one of the five classes shown in Fig. 4.1 were checked on available parameters in DDBST [79].

3. Finally, the ILs mentioned above were checked for availability, price, and safety. At this stage of the research, little is known about which IL will show the best results, if the concept works at all. Therefore, we decided not to synthesize the ILs ourselves. The most common suppliers of Ionic Liquids are
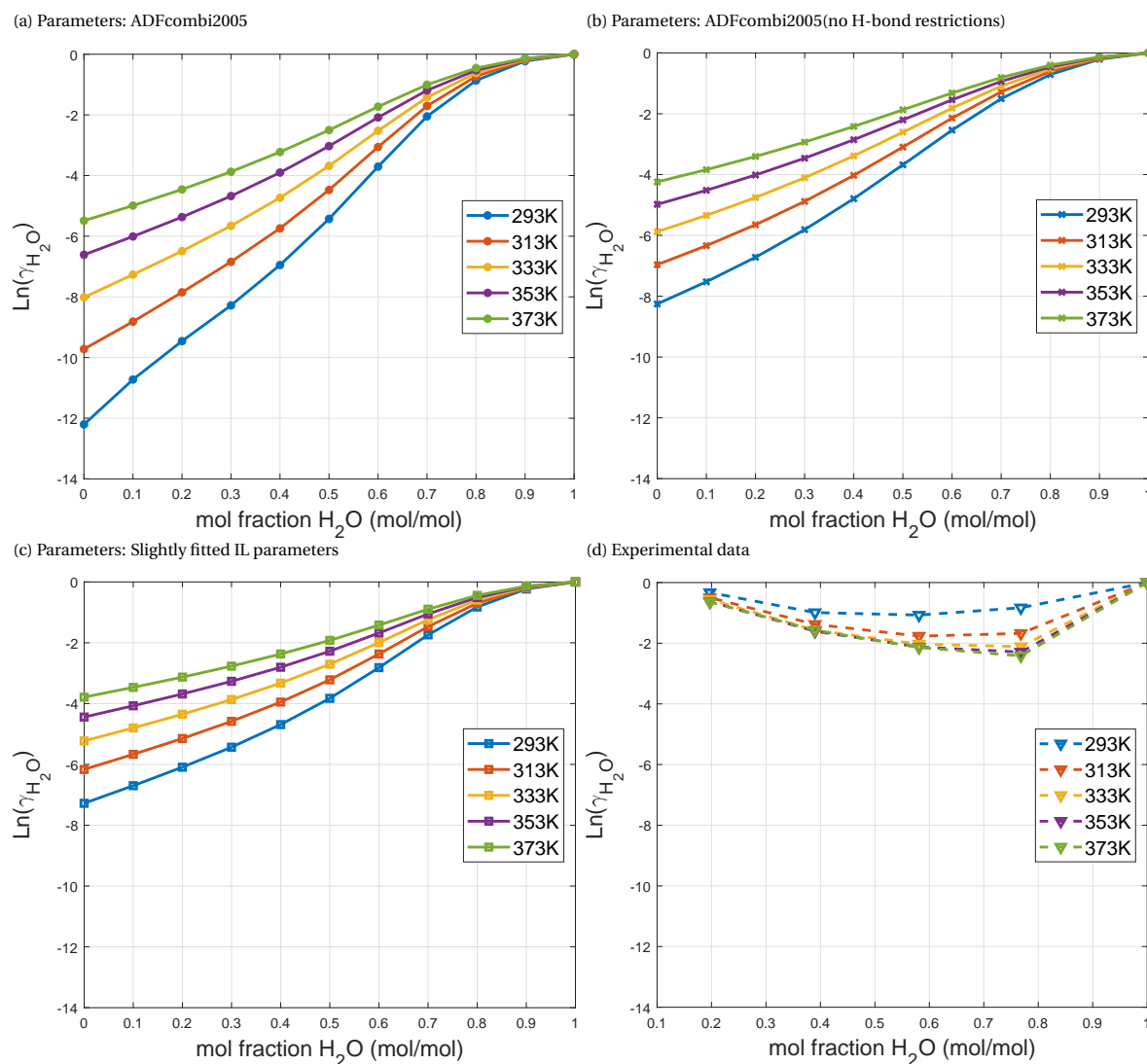
Figure 4.2: Activity coefficient predictions by COSMO-RS (a-c), using three different parameters (ADFcombi2005, ADFcombi2005 (no H-bond restrictions), and slightly fitted parameters). The activity coefficients are plotted as a function of the H_2O mole fraction at five different temperatures (293K, 313K, 333K, 353K, 373K). Experimental data at the same conditions are shown for comparison (d). [75]

Sigma Aldrich® and Iolitec®. The Safety Data Sheets (SDS) were checked to see if the ILs were safe to do experiments on. Due to the limited experience in experimental work with ILs, it was decided to only select ILs that have a GHS07 classification, or less harmful. This classification indicates a warning instead of a real danger [80]. Finally, the price was checked and considered in the decision making. It should be noted that, in a further phase of this research, it is possible to select ILs that do not fulfill these requirements, while they still will deliver significantly better results.

PREVIOUS GAS DEHYDRATION STUDIES

Table 4.1 shows ILs that were used in previous studies describing gas dehydration [17, 65, 81–83]. It is clear that, except for the last one, all cations are imidazolium based.

DORTMUND DATA BANK (DDBST)

The availability of ILs with Modified UNIFAC parameters in DDBST was checked [79]. As expected, imidazolium based Ionic Liquids have the most parameters available. Table 4.2 gives an overview of the most occurring anions and cations. The values represent the activity coefficients at infinite dilution and 25°C, in increasingly order from left to right, bottom to top. In line with previous work [17, 18], this table clearly shows that the activity coefficient mainly depends on the anion instead of the cation. The ILs 1-Ethyl-3-methylimidazolium

Table 4.1: An overview of ILs that were used for gas dehydration in previous work.

Abbreviation	Full Name	Ref
[BEIM][EtSO$_4$]	1-Butyl-3-ethylimidazolium ethyl sulfate	[65]
[BMIM][Ac]	1-Butyl-3-methylimidazolium acetate	[81]
[EMIM][BF$_4$]	1-Ethyl-3-methylimidazolium tetrafluoroborate	[82]
[EMIM][Cl]	1-Ethyl-3-methylimidazolium chloride	[83]
[EMIM][dca]	1-Ethyl-3-methylimidazolium dicyanamide	[82]
[EMIM][EtSO$_4$]	1-Ethyl-3-methylimidazolium ethyl sulfate	[65]
[EMIM][MeSO$_3$]	1-Ethyl-3-methylimidazolium methanesulfonate	[83]
[EMIM][OTF]	1-Ethyl-3-methylimidazolium trifluoromethane sulfonate	[83]
[EMIM][TF$_2$N]	1-Ethyl-3-methylimidazolium bis(trifluoromethanesulfonyl)amide	[17, 82]
[EMIM][TFA]	1-Ethyl-3-methylimidazolium trifluoroacetate	[83]
[N(4)111][Tf$_2$N]	Trimethyl(butyl)ammonium bis(trifluoromethanesulfonyl)amide	[82]

ethyl sulfate ([EMIM][EtSO$_4$]), 1-Ethyl-3-methylimidazolium tetrafluoroborate ([EMIM][BF$_4$]), and 1-Ethyl-3-methylimidazolium bis(trifluoromethanesulfonyl)amide ([EMIM][TF$_2$N]) have been studied for gas dehydration before in previous work (Table 4.1) and have modified UNIFAC parameters. Therefore, these ILs are of particular interest.

Table 4.2: Activity coefficients of water in the given ILs at infinite dilution and 25°C, calculated with modified UNIFAC if parameters were available. For the calculations, the 'Activity Coefficient Calculation' tool from DDBST was used [79]. The ILs are ordered on the activity coefficient, increasing from left to right and from bottom to top.

Anion(down) and Cation(right)	[EMIM]	[PMIM]	[BMIM]	[MMIM]	[HMIM]	[OMIM]	[HOEMIM]	Average
bis(trifluoromethylsulfonyl)imide	3.120	3.268	3.426	2.987	3.761	4.105	2.177	3.263
trifluoromethylsulfonate	0.857	N/A	N/A	N/A	1.117	1.266	N/A	1.080
tetrafluoroborate	1.016	0.928	0.885	1.193	0.867	0.895	1.063	0.978
trifluoromethanesulfonate	N/A	N/A	0.977	0.809	N/A	N/A	N/A	0.893
octyl sulfate	0.304	N/A	0.341	0.287	N/A	N/A	N/A	0.311
hexylsulfate	0.271	N/A	N/A	N/A	N/A	N/A	N/A	0.271
ethylsulfate	0.223	0.231	0.242	N/A	0.271	0.304	N/A	0.254
butylsulfate	0.242	0.255	N/A	N/A	N/A	N/A	N/A	0.249
propylsulfate	0.231	0.242	0.255	N/A	N/A	N/A	N/A	0.243
methylsulfate	0.220	0.223	0.231	0.226	0.255	0.287	N/A	0.241
hydrogensulfate	0.143	0.152	0.164	0.138	0.192	0.224	N/A	0.169
Average	0.663	0.757	0.815	0.940	1.077	1.180	1.620	

AVAILIBILITY AND SAFETY

The ILs used for experiments, are initially selected on the outcomes of previous work, existing modified UNIFAC parameters, and stability. Based on these final criteria, the tetrafluoroborate ([BF$_4$]) cation was no longer considered, as Freire *et al.* showed that BF$_4$-based ILs are not water stable [84]. As safety is of the most importance, the Safety Data Sheets (SDS) of the ILs were checked on the safety criteria mentioned in Section 4.2.4. Finally, the price of the ILs was checked. Both safety and price strongly depend on the way the ILs are synthesized, so if certain ILs look promising, it is interesting to examine what method is the best to synthesize them. Based on all the above mentioned criteria, the ILs, displayed in Table 4.3, were ordered for the experiments.

Table 4.3: The ordered ILs that are used for the experiments. Properties from left to right are Molar weight, melting temperature, density, viscosity, and surface tension all at specified temperature. Properties are from literature, or found on the web via:
a) Iolitec®, b) Sigma-Aldrich®, c) Chemicalbook®

Full name	$M/$(g/mol)	$T_{melt}/$(°C)	$\rho/$(g/cm^3)	$\eta/$(cP)	$\gamma/$(mN/m)
1-Ethyl-3-methylimidazolium acetate	170.21[a]	-45[a]	1.10(25°C)[a]	162(25°C)[85]	42.9(25°C)[86]
1-Butyl-3-methylimidazolium chloride	174.67[a]	65[a]	1.08(25°C)[87]	142(80°C)[85]	48.2(25°C)[88]
1-Ethyl-3-methylimidazolium ethyl sulfate	236.29[a]	<25[a]	1.24(25°C)[a]	94(25°C)[a]	46.9(25°C)[86]
1-Butyl-3-methylimidazolium octyl sulfate	348.50[b]	37[c]	1.07(25°C)[c]	N/A	35.7(30°C)[89]

5

EXPERIMENTS

This chapter describes the experiments that were executed to test the feasibility of high pressure drying of hydrogen gas using Ionic Liquids. The main target of the experiments was to examine if ILs did actually function as an absorbent, when contacted with wet hydrogen gas. Therefore, first experiments were executed that were focused on showing the proof of concept. If the selected ILs did indeed absorb water from the hydrated gas, as expected, the research was extended with an additional experiment, to test if it was also possible to regenerate the IL.

- The main experiment was meant to bubble wet hydrogen gas through an IL and to measure if the resulting hydrogen gas contained less water. The mass transfer from the gas to the liquid was qualitatively determined by measuring if Vapor Liquid Equilibrium was achieved. During these experiments, close attention was paid to properties like viscosity and foam production. This experiment is referred to as the absorption experiment.

- The other experiment was to test if the IL was also capable of releasing the water. To test this, the IL was transferred to a round bottom flask, which was heated and put under vacuum, to shift the VLE of water from the liquid phase to the vapor phase. This experiment is referred to as the desorption experiment.

5.1. ASSUMPTIONS & SIMPLIFICATIONS

The following assumptions and simplifications were made for the experiments in relation to the actual final application, which is HP drying of hydrogen:

1. For safety and simplicity reasons, the absorption experiment is executed at atmospheric pressure, while the final application operates in a pressure range of 800 - 1000 bar. Fortunately, the activity coefficient mostly depends on the temperature and the composition, instead of the pressure. Although these experiments can not be translated one to one to high pressures, these experiments can provide a good impression on how the system would behave at elevated pressures.

2. It is assumed that hydrogen does not dissolve in the Ionic Liquid. This assumption is reasonable, as hygroscopic ILs are selected that are suited for water absorption. Since water is a polar molecule and hydrogen is not, one can assume that the hydrogen dissolved in the IL is negligible [66, 67].

3. Previous studies have shown that the vapor pressure of ILs are so low that they can be neglected [19, 65, 82]. The evaporation of the IL, for the most volatile IL from Table 2.1, was calculated using Raoult's law [46]. This resulted in an IL content in the vapor phase of 2.9×10^{-7} ppm, which is more than a billion times less than water. Therefore, vaporization of ILs is not taken into account in this work.

For another project, a unit was already in place to calibrate and test sensors that can measure contaminants in hydrogen gas up to ppb (parts per billion) level. This unit consists of a number of cylinders that can store hydrogen, contaminated with H_2O, H_2S, CO, and H_2S. This unit has been slightly modified to use it for the absorption experiment.

5.2. Materials & Apparatus

The tested ILs were 1-Ethyl-3-methylimidazolium acetate [EMIM][Acetate], 1-Butyl-3-methylimidazolium chloride [BMIM][Chloride], 1-Ethyl-3-methylimidazolium ethyl sulfate [EMIM][Ethyl Sulfate], and 1-Butyl-3-methylimidazolium octyl sulfate [BMIM][Octyl Sulfate]. The rational for the selection can be found in Section 4.2. The suppliers and purities are specified in Appendix A, along with the specifications of other materials used.

Fig. 5.1 gives an overview of the experimental apparatus. The modified part of the unit is indicated with the dashed rectangle. The left part of the flow diagram is used to regulate the water content in the hydrogen gas. The inlet hydrogen (1) was first purified (2) to remove contaminants using a palladium catalyst. The purified hydrogen was then used to create wet hydrogen (3 and 4) or directly used as a product. The exact procedure for creating wet hydrogen can be found in Appendix A. Using the computer controlled valves (5a and 5b), the wet hydrogen was accurately mixed with dry hydrogen to regulate the desired water content. The hydrogen could then either be directed through the scrubber (7), whose temperature was controlled using a water bath, or bypassed (9). Samples of the resulting hydrogen were then measured by the sensor (10) and finally the hydrogen was directed to the incinerator, where it was burned. Appendix A gives a detailed overview of the used materials and equipment, including a technical drawing of the designed scrubber.
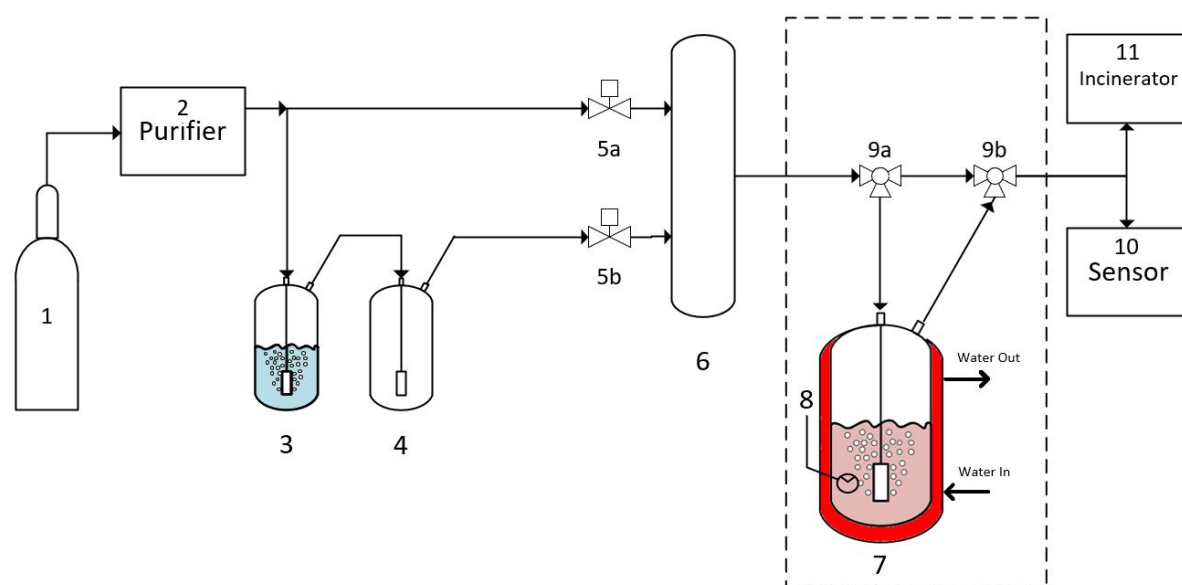
Figure 5.1: Schematic diagram of experimental apparatus for hydrogen dehydration, using ILs. The unit consists of the following components:
1, Hydrogen gas storage; 2, purifier; 3, water scrubber; 4, buffer vessel; 5(a and b), computer valves; 6, mixing vessel; 7, IL scrubber; 8, thermocouple; 9(a and b), three-way hand valves; 10, Sensor; 11, Incinerator. The text above the figure explains how the apparatus works exactly.

5.3. Test Procedure

The absorption and desorption experiments were executed as followed:

5.3.1. Absorption experiments

In this work, the 'dry' IL is defined as the state of the IL, right before it was used in the absorption experiment. After this experiment, the IL is referred to as the 'wet' IL. Note that this classification is not directly related to the absolute water content in the IL. In a typical experiment, a certain amount (about 40 gram) of the 'dry' IL was put into the scrubber (7). Then scrubber 7 was installed in the unit (Fig. 5.1), and the temperature of the scrubber was raised to the desired temperature. When the desired IL temperature, measured by the thermocouple 8, was reached, it was tested if the liquid phase was in equilibrium with the vapor phase. This started by bubbling dry hydrogen gas through the IL in the scrubber. The output water content was measured by sensor 10. After this measurement, the hydrogen flow was bypassed (via valves 9a and 9b) and the water content was increased to 1755 ppm. If the water content was constant (this always took about 5 minutes, due to the memory effect of pipes and valves), the hydrogen gas was again directed over the scrubber. The

VLE was checked by comparing the output water content with the initial output, where dry hydrogen gas was bubbled through the IL. The VLE was achieved, once these measurements were equal. This process is visualized in Section 6.2. If VLE was reached, the measurements could continue. Because the IL is absorbing water from the wet hydrogen gas, the water fraction in the IL gradually increases. The absorption experiment was continued until the water content in the hydrogen gas reached 500 ppm, due to the limitations of the sensor, specified in Appendix A. When this water content was reached, it was tested again if a VLE has been established. This procedure was the same as at the start of the experiment, only now starting with wet hydrogen gas, instead of dry hydrogen. Finally the IL was drained from the scrubber into a round bottom flask, to start the desorption experiment. At the same time, a sample of the 'wet' IL was taken, for the KF titration.

5.3.2. Desorption experiment
For the desorption experiment, the round bottom flask containing the 'wet' IL, was placed in a heating mantle and was via a vacuum adapter connected to a vacuum pump at 15 mbar. The flask was heated up to 150°C for [BMIM][Chloride] and[BMIM][Octyl sulfate]. The temperature of [EMIM][Acetate] was limited to a maximum of 100°C, as the work of Cao and Mu showed that acetate based ILs are less stable and can start to decompose at temperatures lower than 150°C [90].

5.3.3. Karl Fischer titration
The water content in the dry and wet IL was measured using Karl Fischer titration. Because of the high viscosity of the liquids, samples were diluted with methanol. The specifications of the KF coulomat and the methanol are described in Appendix A. Since the ILs are very hygroscopic, contact with the surrounding air should be avoided. Therefore, transfer of IL was always performed in a glove box, or through syringe needles that were flushed with nitrogen prior to use.

6

RESULTS & DISCUSSION

The experimental results are divided into two sections. Section 6.1 outlines the observations of the different Ionic Liquids for the absorption and desorption experiments. These observations include bubble formations, foaming, color change, and crystallization. Section 6.3 reports the more quantitative experimental results. The data from the sensor, that measures the water content in the dehydrated hydrogen gas is used to calculate the VLE of the H_2O - IL mixture.

Table 6.1: The ordered ILs that are used for the experiments. Properties from left to right are Molar weight, melting temperature, density, viscosity, and surface tension all at specified temperature. Properties are from literature, or found on the web via: a) Iolitec[®], b) Sigma-Aldrich[®], c) Chemicalbook[®]

Full name	M/(g/mol)	T_{melt}/(°C)	ρ/(g/cm^3)	η/(cP)	γ/(mN/m)
1-Ethyl-3-methylimidazolium acetate	170.21[a]	-45[a]	1.10(25°C)[a]	162(25°C)[85]	42.9(25°C)[86]
1-Butyl-3-methylimidazolium chloride	174.67[a]	65[a]	1.08(25°C)[87]	142(80°C)[85]	48.2(25°C)[88]
1-Ethyl-3-methylimidazolium ethyl sulfate	236.29[a]	<25[a]	1.24(25°C)[a]	94(25°C)[a]	46.9(25°C)[86]
1-Butyl-3-methylimidazolium octyl sulfate	348.50[b]	37[c]	1.07(25°C)[c]	N/A	35.7(30°C)[89]

6.1. OBSERVATIONS

The experiments are outlined in Chapter 5 and in Appendix A.

[EMIM][EtSO$_4$]

Unfortunately, during the first experiment with [EMIM][EtSO$_4$], we found that the Safety Data Sheet (SDS) was modified by Sigma-Aldrich[®] compared to the date at which we ordered this IL. The SDS was updated with safety classifications GHS05, GHS06, and GHS08, which we concluded to form a too high risk, as discussed in Section 4.2.4. Therefore, we decided to stop the experiments with this particular IL.

6.1.1. BUBBLE FORMATION AND FOAMING

Fig. 6.1 shows the three ILs during the dehydration experiment. The [BMIM][Chloride] clearly shows a different bubble formation than the other two ILs. The hydrogen gas that enters the scrubber forms very large bubbles that slowly rise as the bubbles grow. There is no layer of foam on top of the IL. For the ILs [EMIM][Acetate] and [BMIM][Octyl Sulfate] on the other hand, a clear separation between the fluid and foam is observed. Foam producing can cause two significant problems:

1. If the foam layer grows to a certain height, the IL-foam leaves the scrubber and enters the rest of the system. This causes pollution of the sensor and a loss of IL. Since the VLE calculations assume a constant amount of IL, as explained in Chapter 5, a loss of IL means that the results are not representative. To prevent this overflow, the volume of the IL used for the experiments, which was originally set at 40 ml, needed to be reduced to 25 ml for [BMIM][Octyl Sulfate]. The amount of IL could not be reduced further, otherwise the hydrogen gas inlet was not submerged in the IL.

2. The second problem that occurs due to foaming is low diffusion of water in the IL. Hydrogen gas does not enter the scrubber from the bottom, so there is a layer of IL where hydrogen bubbles are not forced

(a) [BMIM][Chloride]   (b) [EMIM][Acetate]   (c) [BMIM][Octyl Sulfate]
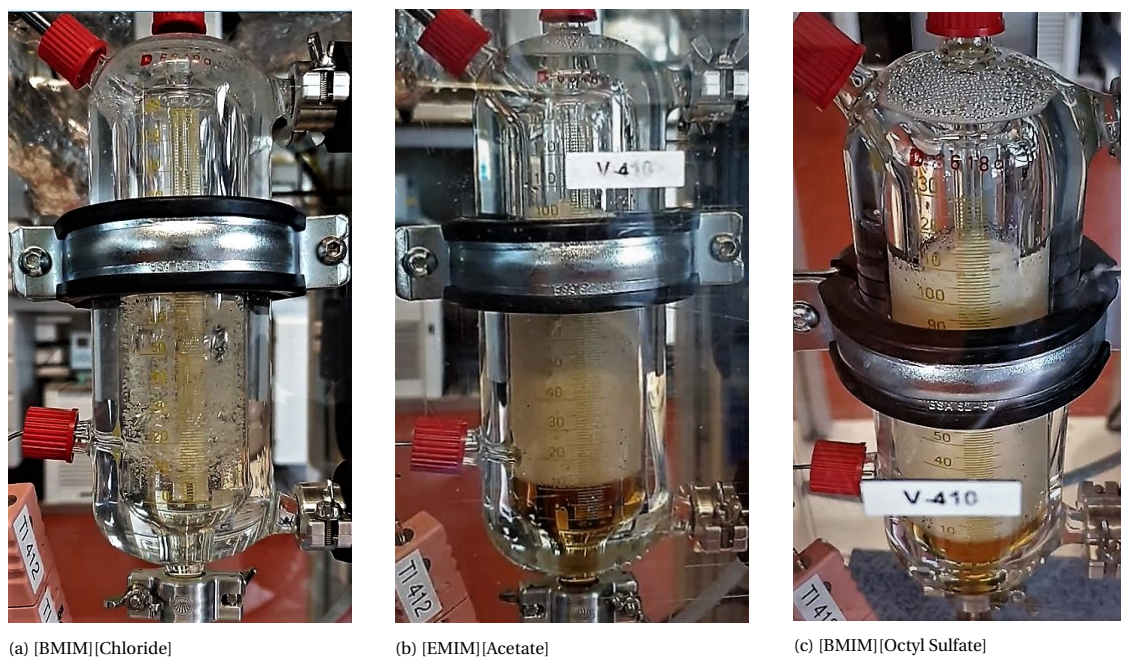
Figure 6.1: Snapshots of the experiments with three different ILs at 70°C and atmospheric pressure. The input water content in the hydrogen gas is 1755ppm and the flow rate is 40 Nl/h

through. The risk is that the foam reaches an equilibrium very quickly, while the liquid at the bottom still has enough capacity to absorb water. Section 5.3.1 describes how it was tested if this was indeed occuring.

It is well known that surface tension, which acts to reduce the surface of a liquid to a minimum, has a large impact on foam production [91]. To prevent problems related to foaming, ILs with a relatively high surface tension must be selected. As mentioned in Chapter 4, it is hard to predict IL properties, such as surface tension. However, many anions of ILs consist of an alkyl group that lowers the surface tension of a molecule [92]. The longer the alkyl chain, the lower the surface tension [92]. It is therefore not surprising that [BMIM][Octyl Sulfate] produces a lot of foam. The IL properties in Table 6.1 confirm the relation between alkyl chain length and surface tension. Note that the properties in Table 6.1 are mostly at at a temperature of 25°C, while the experiments shown in Fig. 6.1 were executed at a temperature of 70 °C. A higher temperature results in a lower viscosity, which also increases foam formation [93]. Furthermore, as temperature rises, cohesive forces between molecules decrease, resulting in a lower surface tension [91]. Fig. 6.2 clearly shows the temperature effect on foam production. To prevent foaming, it is therefore recommended to absorb at low temperatures.

6.1.2. COLOR CHANGE
During the regeneration process, described in Chapter 5, the ILs [EMIM][Acetate] and [BMIM][Octyl Sulfate] changed color. This process is pictured in Fig. 6.3. When heated, the colors transformed from light yellow to very dark brown. Previous work also observed this color change [94]. The color change is possibly due to the impurities in the IL [94].

6.1.3. CRYSTALLIZATION RANGE
A final observation that was made was the large crystallization range of the ILs that have a melting point above room temperature([BMIM][Octyl Sulfate] and [BMIM][Chloride]). Both ILs were sometimes a liquid at room temperature, and sometimes a solid.

(a) [EMIM][Acetate] at 70°C

(b) [EMIM][Acetate] at 30°C
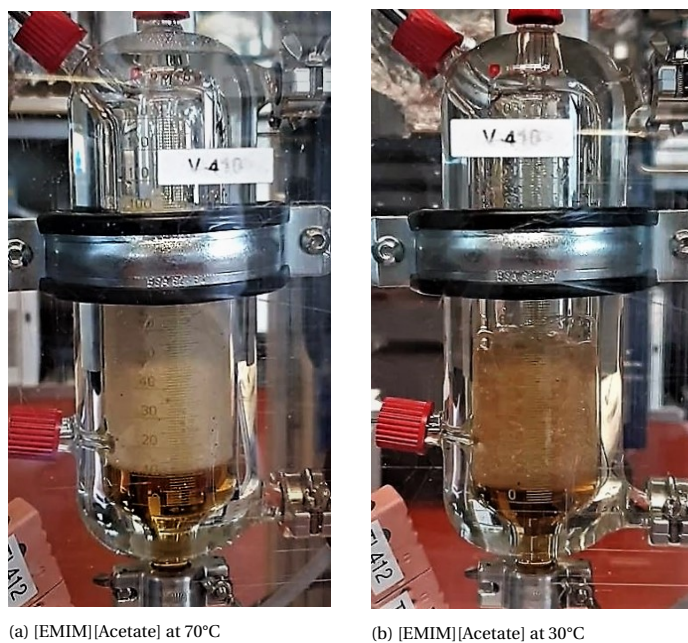
Figure 6.2: Foam production in [EMIM][Acetate] during dehydration experiment. Both experiments are at atmospheric pressure, constant water content and constant flow rate of 40 Nl/h. The only difference is the temperature (70°C in a and 30°C in b)

(a) [EMIM][Acetate]

(b) [BMIM][Octyl Sulfate]
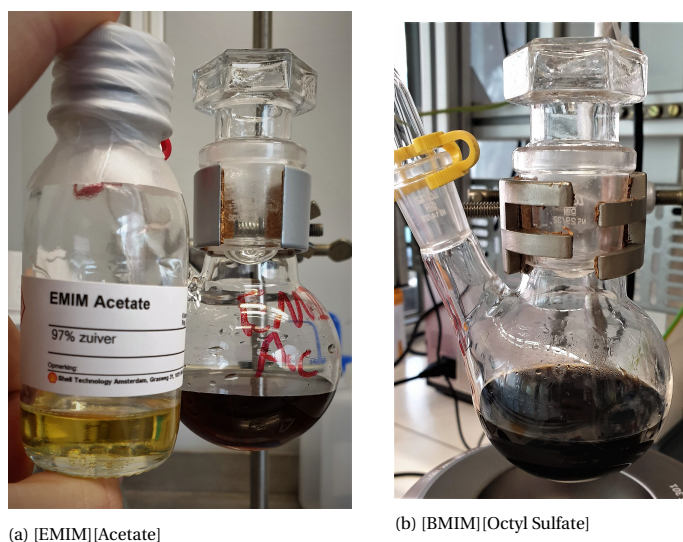
Figure 6.3: Observed color change during the desorption experiment, for the ILs [EMIM][Acetate] (a) and [BMIM][Octyl Sulfate] (b).

6.2. VAPOR LIQUID EQUILIBRIUM

To compare the ILs on a more quantitative basis, the water content in the output stream is measured and subtracted from the input water content. Appendix A describes how the input water content is regulated. A Vapor Liquid Equilibrium between the liquid phase and the vapor phase is essential to draw conclusions on absorption capacity and the activity coefficients of the ILs. Therefore, during every experiment it is tested if, at the specified conditions, equilibrium is achieved. This procedure is described in Section 5.3.1. Fig. 6.4 presents the results of such an experiment for all three ILs. A VLE is achieved if the water content in the resulting hydrogen gas remains constant when the input water content is instantly changed from wet hydrogen to dry hydrogen. Fig. 6.4 shows that [BMIM][Chloride] and [EMIM][Acetate] are in equilibrium with the vapor phase, at the specified conditions. [BMIM][Octyl Sulfate], however, does not achieve VLE. This has two possible reasons. Firstly, the absorption rate of water from the vapor phase to the liquid phase could be too low. Secondly, the diffusion in the IL could be the problem. The latter implies that a certain amount of the IL is in equilibrium, but the water does not diffuse through the rest of the IL quickly enough. The significant foam production, which is visualized in Fig. 6.1c, is the most plausible reason for preventing a fast VLE. The foam is in equilibrium with the hydrogen gas, but the water absorbed by the foam is not (quickly enough) transported to the liquid layer below the foam.
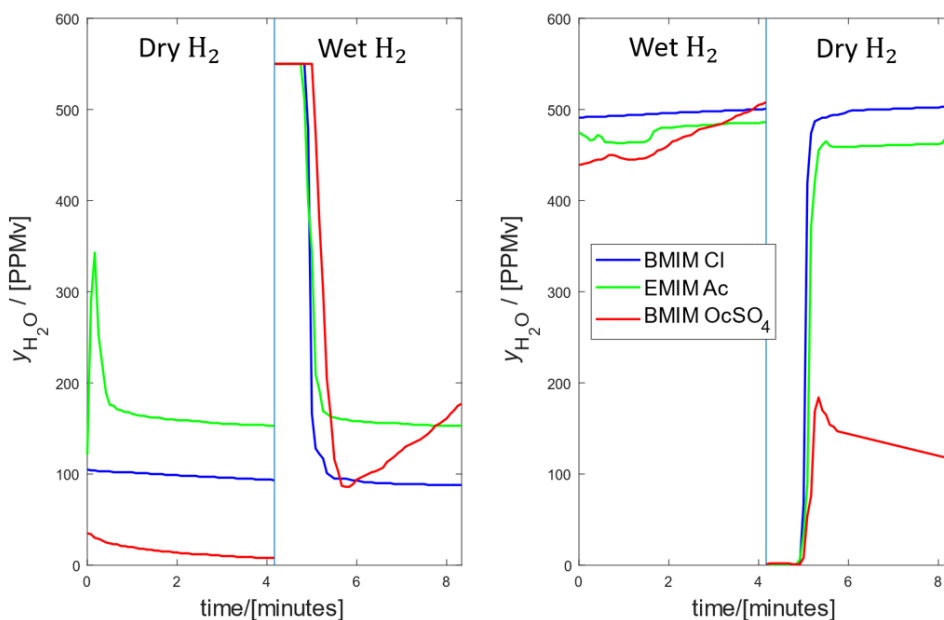
Figure 6.4: Experimental results of the VLE tests. The left figure shows the start of the experiment, where the IL is still dry. The right figure shows the measured water content at the end of the experiment. VLE is achieved, if the output water content remains constant when the input stream is instantly changed from dry to wet hydrogen, or the other way around. The small difference can be explained by a memory effect in the pipes.

6.3. MEASUREMENTS

The VLE experiments showed that the ILs [BMIM][Chloride] and [EMIM][Acetate] achieved VLE during the experiment and are in equilibrium with the hydrogen gas. However, as [EMIM][Acetate] absorbed more water, the foam production increased. Additional experiments at lower temperatures are required to test [EMIM][Acetate]. Therefore, the main focus of this chapter is on the results obtained with [BMIM][Chloride]. Therefore, the $\gamma - \phi$ approach, described in Section 3.3, can be applied to calculate the properties of the ILs. Since the experiments are executed at atmospheric conditions, the Poynting Effect is negligible. Furthermore, the ideal gas law is applied, resulting in fugacity coefficients equal to unity. Therefore the $\gamma - \phi$ equation reduces to Eq. (6.1), which is also referred to as modified Raoult's law [41].

$$y_{H_2O} P = \gamma_{H_2O} x_{H_2O} P_{H_2O}^{sat} \tag{6.1}$$

The output water content in the vapor phase y_{H_2O} is measured by the sensor. Fig. 6.5a shows the water content in the hydrogen gas, after it was bubbled through the IL [BMIM][Chloride]. The input water content is constant over time and the output water content is increasing, as the IL absorbs water. The difference between the water content in the input and the output is the amount of water that is absorbed by the IL. Therefore, we know the increase of the water fraction in the IL over time. The results in Fig. 6.5a show that the experiments are in good agreement with one another. Especially experiments 2 and 3, which both started with a regenerated IL, instead of a new one. It is remarkable that the regenerated ILs start with a lower water content than the new one. The next step is to calculate the VLE from these results. The only parameter that is missing to calculate the activity coefficient is the initial water fraction in the IL. The water content in the IL is measured with the Karl Fischer (KF) titration method. At the end of the experiment, the water content in the IL is measured again. This is to check if the water content is now equal to the initial water content plus the absorbed water. Unfortunately, Fig. 6.5b shows that this is not the case. The KF-results should correspond to the end values of the plotted curves. It is clear that the KF measurements are far off, which may be explained as follows:

1. The water absorbed by the IL is not measured accurately. This is unlikely, because the input water content is constant and the output water content is measured by a sensor that is well calibrated and capable of measuring contaminants like water at ppb level.

2. Another explanation could be the accuracy of the KF titration. At every KF measure, three samples were tested. The measurements had a deviation of around 5%. If the error exceeded this error percentage, additional samples were taken. The dashed lines in Fig. 6.5b represent this 5% error. It is obvious that the difference between the KF samples and the sensor measurements is much larger.

3. A more likely explanation is that the samples absorbed water from surrounding air before they were injected in the KF device. Surrounding air easily contains 10-100 times more water than the hydrogen gas in the experiment. Therefore, the ILs strongly attract water molecules, before and after the experiment. Although air contact was avoided at all times using glove-boxes and needles, it is hard to completely eliminate any form of air contact. Furthermore, due to the occasionally unavailability of the KF-equipment, it was not always possible to directly take the KF samples. Therefore, the time between the experiments and the KF titration differed quite a lot. Although the samples were sealed, some water penetration in the sample is still possible, especially with this long waiting times.

(a) water content in the vapor phase, as a function of time.

(b) mass fraction of water in the IL, as a function of time.
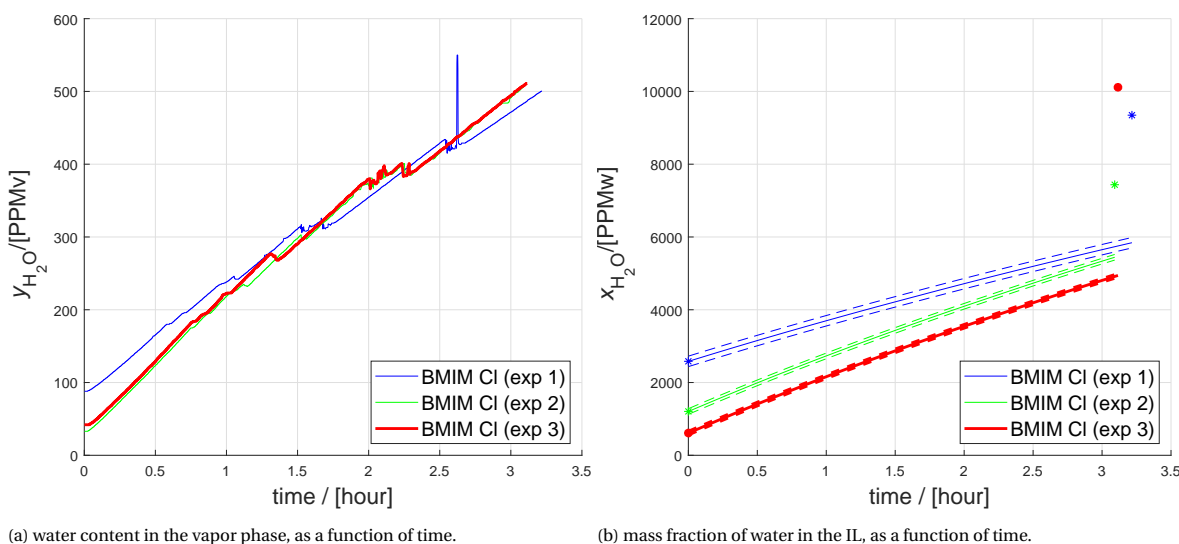
Figure 6.5: Water content in the hydrogen gas, which is bubbled over the IL [BMIM][Chloride] (a). As the IL absorbs water from the hydrogen gas, the mass fraction of water in the IL increases (b). All experiments are at atmospheric pressure and a constant flow rate of 40 Nl/h and a water content input of 1755ppm.

Due to the fact that the absolute water content in the IL is unknown, it is not possible to calculate the activity coefficient very accurately. The lines plotted in Fig. 6.6, showing the VLE of H_2O and the calculated activity coefficients, should coincide. It is clear from Fig. 6.6a, that the different experiments show similar

slopes. If the individual slopes would only be translated in the x-direction, they would coincide very well. This strengthens the theory that the bad results are caused by the absence of the initial water content. Based on the results shown in Fig. 6.6b, it is not possible to determine the activity coefficient as a function of the water fraction in the IL. However, it is fair to say that in this low water fraction region, the activity coefficient is low. Even if it would be off by a factor two, it would still be well below 0.1, which is still very low.
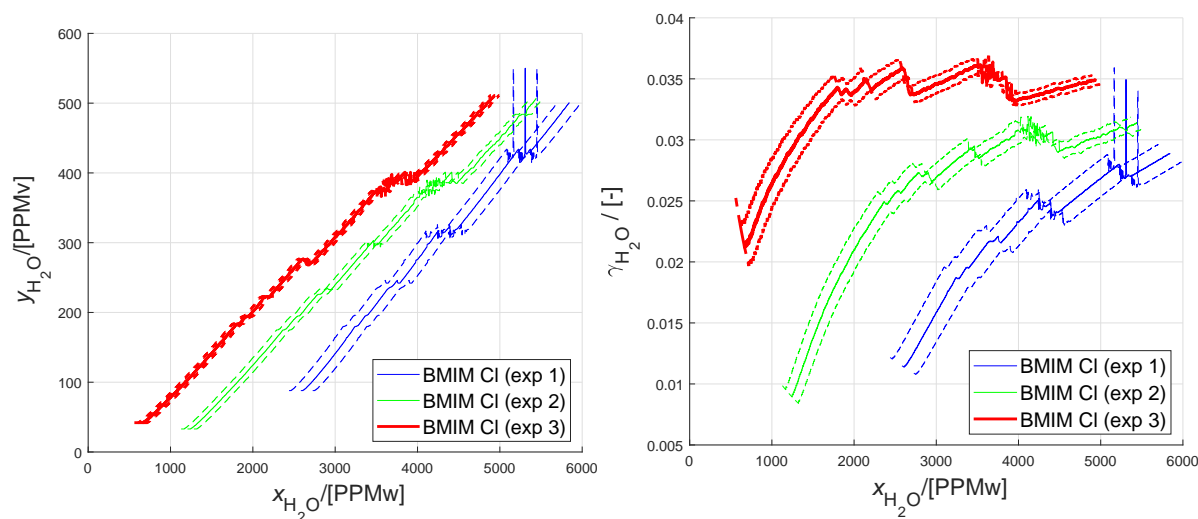
(a) Calculated Vapor Liquid Equilibrium of the IL-H_2O system.

(b) Activity Coefficients, calculated with the Gamma/Phi approach, as a function of the mass fraction of the water in the IL.

Figure 6.6: The measured water content in the vapor phase is plotted against the calculated mass fraction of water in the IL (a). This is calculated by adding the absorbed water to the initial mass fraction of water. The activity coefficient easily follows from modified Raoult's law and is plotted against the mass fraction of water in the IL (b).

6.3.1. EMIM ACETATE
Fig. 6.7a shows the same experiment for [EMIM][Acetate]. The first experiment looks very promising, as it takes two times longer to reach the 500 ppm water content in the vapor phase, compared to the experiment with [BMIM][Chloride]. However, it is much harder to regenerate the IL. The green line in Fig. 6.7a shows the second experiment, so after the IL has been regenerated. It is clear that the IL can not be dried to a water content near the new IL. One reason for this is that the [EMIM][Acetate] is regenerated at 100°C instead of 150°C, due to the fact that it is less stable, as explained in Section 5.3.2. The other reason is that Acetate is very hydrophilic, even more hydrophilic than the Chloride anion [95]. Although this has the advantage that it can absorb a lot of water, a clear downside is that it costs a lot of energy to get the water out again. A third experiment with this IL resulted in a water content at the start of the experiment of 500 ppm. This is the same as the end value of the previous experiment, meaning that no water was removed during regeneration. Another downside of hydrophilic ILs is the effect of the water content on the resulting properties [96]. Increasing the alkyl chain length of the anion creates a more stable and hydrophobic IL, which makes it easier to regenerate the IL [96]. However, as mentioned in Section 6.1.1, a longer alkyl chain reduces the surface tension which results in foam production.

LOWER TEMPERATURES
Fig. 6.7b shows the absorption experiment fro [EMIM][Acetate], executed at 30°C, instead of 70°C. It was not possible to reduce the temperature for [BMIM][Chloride], due to the melting temperature of 65°C. It is clear that a lower temperature results in an enormous increase of the water absorption capacity of the IL. This is due to the fact that the vapor pressure of water drastically decreases with temperature. The experiment at 30°C took almost 30 hours. For safety reasons, the experiments did not continue overnight. Therefore, a single experiment took almost a week, resulting in only a single run. More experiments at multiple temperatures are required to test the temperature dependency on the IL properties, like the activity coefficient.

(a) 70°C

(b) 30°C
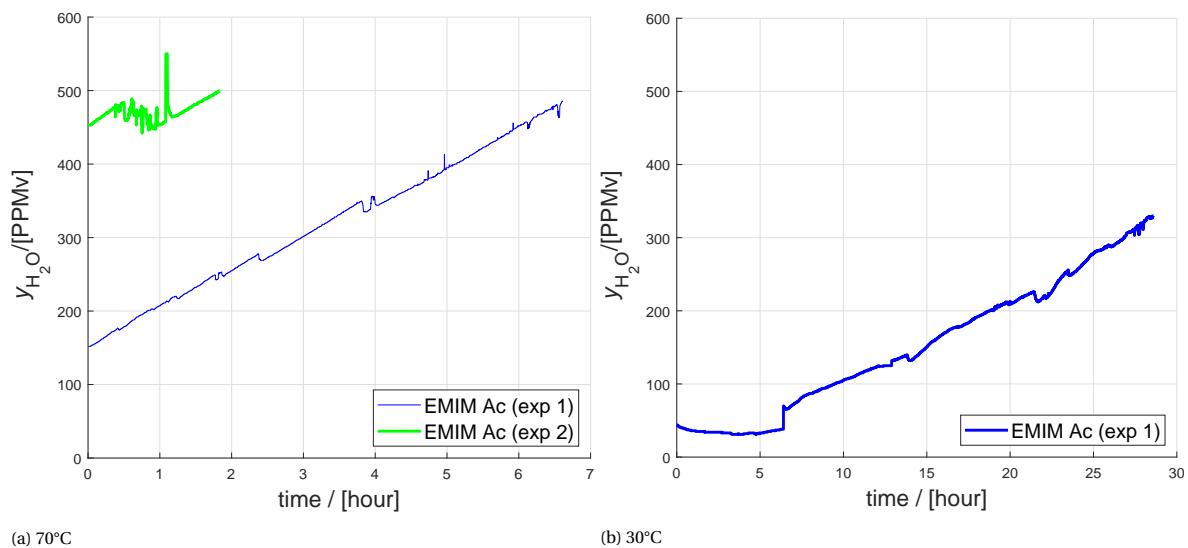
Figure 6.7: Water content in the hydrogen gas, which is bubbled over the IL [EMIM][Acetate], at a temperature of 70°C (a), and 30°C (b). All experiments are at atmospheric pressure and a constant flow rate of 40 Nl/h and a water content input of 1755ppm.

7

CONCLUSIONS

The goal of this project was twofold. The first objective was to obtain a better understanding of the H_2-H_2O system, by calculating the saturated water content in compressed hydrogen. The second objective was to test the feasibility of using Ionic Liquids as a drying agent for HP hydrogen dehydration.

7.1. THERMODYNAMICS

1. Chapter 3 showed that conventional EoS, with classical mixing rules, are not capable of describing the H_2-H_2O system at elevated pressures. The EoS that were tested included Peng-Robinson (PR), Soave's Redlich Kwong (SRK), and Shell's in-house developed (SMIRK) EoS.

2. Molecular simulation results showed excellent agreement with experimental data, especially for the vapor phase. The TIP3P [54] forcefield gave the best results for water, and the Marx [53] forcefield for hydrogen. As expected, the simulation with the highest pressure and lowest temperature conditions, resulted in the lowest water content. Namely 29 μmol per mol H_2-H_2O mixture, at 10 °C and 1000 bar.

7.2. IONIC LIQUIDS

The following conclusions can be drawn from the experimental results.

1. First of all, Ionic Liquids can be used as an absorbent to dehydrate hydrogen gas. As expected, the experiments showed that bubbling wet hydrogen gas through an IL resulted in a dehydrated hydrogen output.

2. Foam production is more relevant than initially expected. Foam production drastically decreases the mass transfer of water through the IL. Due to the lack of diffusion, equilibrium is not achieved, reducing the capacity of the IL for water absorption drastically. Since surface tension is directly related to foam production, this should be an important property to check in the selection process.

3. ILs that are capable of absorbing large amounts of water can dry the hydrogen gas to a very low water content. However, this does not necessarily mean that they are suited for this application. Due to their high attraction to water, it costs a lot of energy to regenerate very hydrophilic anions, like acetate. Non-polar molecules with long alkyl chains are more hydrophobic, but they have the drawback that they produce more foam.

4. The temperature of the absorption process is preferably as low as possible, even though lower temperatures result in higher viscosities. Firstly, surface tension increases with decreasing temperatures, resulting in less foam production (see Section 6.1.1). Secondly and most importantly, the saturated vapor pressure of water decreases drastically with temperature. Referring to the $\gamma-\phi$ equation (Eq. (7.1)), a low K is desired, as it results in a higher water content in the liquid phase. Even if low temperatures result in higher activity coefficients, which is observed by previous studies [75], the saturated vapor pressure of water $P^{\text{sat}}_{H_2O}$ decreases drastically with temperature. For example, the activity coefficient of water in [EMIM][Acetate] γ_{H_2O} decreases by a factor 4 as temperature rises from 10°C to 70°C, while at

the same time, the saturated vapor pressure $P_{H_2O}^{sat}$ increases by a factor 25 [47]. Therefore, for future selection, ILs must have a melting temperature below 0°C.

$$K_{H_2O} = \frac{y_{H_2O}}{x_{H_2O}} = \frac{\gamma_{H_2O} \, \Phi_{H_2O}^{sat} \, P_{H_2O}^{sat}}{\hat{\Phi}_{H_2O} \, P} \exp\left[\frac{V_{H_2O}(P - P_{H_2O}^{sat})}{RT}\right] \tag{7.1}$$

5. Although preliminary experiments show low activity coefficients for water in the tested ILs, no firm conclusions can be drawn on this matter. Additional experiments are required at different temperatures to determine the temperature dependency of the activity coefficient. Furthermore, due to the limited range of the sensor, it was not possible to measure the composition dependency of the ILs, as all ILs were still relatively dry. Due to this low range, it was also not possible to measure the maximum amount of water per unit of weight that the ILs can absorb. Finally, no reliable absolute values were obtained, based on the KF titrations.

Based on the molecular simulation results and the results obtained from the Ionic Liquid experiments, it is too premature to select the best method for high pressure hydrogen dehydration. However, based on the thermodynamics, it can be concluded that most of the water can be removed by condensing the water out. Experiments are required to see if it would be possible to get the water content down to 5 ppm, by reducing the temperature and/or increasing the pressure even further.

If this is not possible, an additional drying unit is still required. It is not possible to point out the best dehydration method, based on this work. There are two drying methods favorable over the others. Firstly Temperature Swing Adsorption (TSA), but only if the purging gas is recycled, to prevent hydrogen losses. The other option is absorption, in which case ILs look like a promising alternative for conventional absorbents, mainly for their negligible vapor pressure.

8

RECOMMENDATIONS

8.1. THERMODYNAMICS

1. The molecular simulation predictions of the vapor phase were in good agreement with experimental data. However, to further improve the molecular simulations, the polarizability of the water molecules must be included.

2. It is highly recommended to do VLE experiments on the H_2-H_2O system at high pressures, for several reasons.

   (a) Even though the molecular simulations are in excellent agreement with the available experimental data, the simulated data are still predictions. Since there is only one paper available that describes the system at pressures exceeding 300 bar, which is also from 1927, more experimental data are required to validate the molecular simulations. For the experiments of Bartlett, compressed hydrogen was bubbled through water and then expanded to atmospheric pressure. The resulting gas was dehydrated by means of phosphorus pentoxide. As a result, the phosphorus pentoxide gained weight, which was equal to the water that was originally in the vapor phase. Although these experiments can be repeated relatively easy, state-of-the-art sensors like the one used in this work, can measure water content at low pressures more accurate. An additional advantage of the experiments would be that the experimental data can be used to fit EoS with more complex physically based mixing rules. These fitted EoS can than easily be integrated within existing tools, which significantly reduces calculating time compared to molecular simulations.

   (b) Since the absorption will take place at temperatures near the melting point of water, ice formation may occur, which is not included in the model. Experiments are required to measure ice formation at temperatures near and below 0°C.

   (c) Finally, as mentioned in Section 3.5.2, gas-gas immiscibility may occur. This can result in the behaviour that if temperature is gradually reduced, the saturated water content will initially decrease, but at a certain moment this can potentially increase again. This phenomenon is also not included in the molecular simulations and therefore experiments are needed.

8.2. IONIC LIQUID SELECTION

1. To select the optimal IL, a software tool is required that is capable of predicting IL properties more accurately. To do this, more experimental data are required that can validate this tool.

2. On top of the criteria stated in Section 4.2, new criteria are added for future selection.

   • The melting point of the IL T_{melt} must be below zero.

   • The surface tension is preferably high, to avoid foam production.

   • The IL must be hygroscopic, but does not necessarily have to be hydrophilic. A balance should be found between the capability of the IL for absorption and for desorption, to avoid high energy requirements for regeneration of the IL.

8.3. IONIC LIQUID EXPERIMENTS

1. For safety reasons, it is recommended to frequently check the SDS of the chemicals one is working with, as we have experienced that these sheets can change over time.

2. An additional sensor would be helpful to continuously measure the input water content. Although the flowrate through the water was unchanged, the water content in the hydrogen input showed some instabilities. If the input and the output would always be measured simultaneously, the results would be more reliable.

3. Unfortunately, it was not possible to obtain valid results for the activity coefficient, as a function of temperature and composition. A few measures are recommended to improve the experiments.

   (a) Firstly, the absolute water content was not accurately measured. It is recommended to install the entire KF equipment in the glove box. During the filling and draining of the scrubber, which should also happen in the glove box, the KF titrations must be executed. This way additional measure are taken to avoid surrounding air contact, and all samples are taken at the same time and conditions. It is also advised to explore other methods to measure the water content in substances.

   (b) To determine the temperature dependency of the activity coefficients, additional experiments at different temperatures are required.

   (c) Finally, a sensor is required that has a higher range, so it is capable of detecting higher levels of water content in the hydrogen gas. This is needed to determine the maximum water content in the IL, as well as to calculate the composition dependency of the activity coefficient.

4. In a further phase of the research, it is recommended to do the absorption experiments at elevated pressure, to check if the activity coefficient does indeed not depend significantly on pressure.

8.4. NEXT PHASE

Based on this work, the following actions are recommended, in order to find the best method for HP drying of hydrogen gas:

1. Even though it is unlikely to get it adjusted, the rational for the 5 ppm restriction needs to be investigated. The risk of ice formation during the refueling process is rejected. This is not possible, as multiple studies showed that the temperature will only rise during this process. Water can provide a transport mechanism for other contaminants, but it is questionable if the water content must be this low to avoid that.

2. The first step is to validate the molecular simulation results with accurate HP VLE experiments. Thereafter, the temperature can be reduced further to see if a water content of 5ppm can be achieved with condensing only.

3. If an additional dehydration step is still required, both TSA and absorption should be investigated more extensively. For absorption, it is recommended to calculate and experimentally validate the vapor pressure of conventional absorbents, like TEG. Even though these absorbents have the disadvantage of contaminating the hydrogen gas, the high pressure and low temperature conditions can result in a very low vapor pressure. At these conditions, the vapor pressure can become so low, that the advantage of ILs almost disappears.

4. If more extensive comparison between TSA and absorption shows that absorption is favorable, but TEG is not suitable due to evaporation, further research in ILs is recommended.

BIBLIOGRAPHY

[1] *Adoption of the Paris Agreement*, Tech. Rep. FCCC/CP/2015/L.9/Rev.1 (United Nations, Framework Convention on Climate Change, Paris, 2015).

[2] *Transforming our world: the 2030 Agenda for Sustainable Development*, Tech. Rep. A/RES/70/1 (United Nations, General Assembly, New York, 2015).

[3] *World Energy Outlook 2018*, Tech. Rep. (International Energy Agency, 2018).

[4] A. Gallo, J. Simões-Moreira, H. Costa, M. Santos, and E. Moutinho dos Santos, *Energy storage in the energy transition context: A technology review,* Renewable and Sustainable Energy Reviews **65**, 800 (2016).

[5] B. Zakeri and S. Syri, *Electrical energy storage systems: A comparative life cycle cost analysis,* Renewable and Sustainable Energy Reviews **42**, 569 (2015).

[6] A. Evans, V. Strezov, and T. J. Evans, *Assessment of utility energy storage options for increased renewable energy penetration,* Renewable and Sustainable Energy Reviews **16**, 4141 (2012).

[7] A. van Wijk and C. Hellinga, *Hydrogen the key to the energy transition,* Tech. Rep. (Delft University of Technology and TVVL, 2018).

[8] T. Mahlia, T. Saktisahdan, A. Jannifar, M. Hasan, and H. Matseelar, *A review of available methods and development on energy storage; technology update,* Renewable and Sustainable Energy Reviews **33**, 532 (2014).

[9] B. Johnston, M. C. Mayo, and A. Khare, *Hydrogen: the energy source for the 21st century,* Technovation **25**, 569 (2005).

[10] J. Adolf, C. Balzer, and J. Louis, *Energy of the Future? Sustainable Mobility through Fuel Cells and* H_2, Tech. Rep. (Shell Deutschland Oil GmbH, Wuppertal Institut, Hamburg, 2017).

[11] P. Bouwman, *Electrochemical Hydrogen Compression (EHC) solutions for hydrogen infrastructure,* Fuel Cells Bulletin **2014**, 12 (2014).

[12] M. Nordio, F. Rizzi, G. Manzolini, M. Mulder, L. Raymakers, M. Van Sint Annaland, and F. Gallucci, *Experimental and modelling study of an electrochemical hydrogen compressor,* Chemical Engineering Journal **369**, 432 (2019).

[13] M. Bampaou, K. D. Panopoulos, A. I. Papadopoulos, P. Seferlis, and S. Voutetakis, *An Electrochemical Hydrogen Compression Model,* Chemical Engineering Transactions **70** (2018), 10.3303/CET1870203.

[14] *Hydrogen fuel - Product specification - Part 2: Proton exchange membrane (PEM) fuel cell applications for road vehicles,* Tech. Rep. ISO 14687-2:2012(E) (International Organization for Standardization, Switzerland, 2012).

[15] E. P. Bartlett, *The concentration of water vapor in compressed hydrogen, Nitrogen and a mixture of these gases in the presence of condensed water,* Journal of the American Chemical Society **49**, 65 (1927).

[16] J. Hallet and W.-C. Tu, *Possible use of ionic liquids to dry hydrogen gas,* Tech. Rep. (Imperial College, 2016).

[17] G. Yu, C. Dai, L. Wu, and Z. Lei, *Natural Gas Dehydration with Ionic Liquids,* Energy and Fuels **31**, 1429 (2017).

[18] J. Han, C. Dai, Z. Lei, and B. Chen, *Gas drying with ionic liquids,* AIChE Journal **64**, 606 (2018).

[19] M. Krannich, F. Heym, and A. Jess, *Characterization of Six Hygroscopic Ionic Liquids with Regard to Their Suitability for Gas Dehydration: Density, Viscosity, Thermal and Oxidative Stability, Vapor Pressure, Diffusion Coefficient, and Activity Coefficient of Water,* Journal of chemical & engineerging data **61**, 1162 (2016).

[20] E. Hendriks, G. M. Kontogeorgis, R. Dohrn, J.-C. De Hemptinne, I. G. Economou, L. Fele, Z. . Ilnik, and V. Vesovic, *Industrial Requirements for Thermodynamics and Transport Properties,* Ind. Eng. Chem. Res **49**, 11131 (2010).

[21] J. S. Lopez-Echeverry, S. Reif-Acherman, and E. Araujo-Lopez, *Peng-Robinson equation of state: 40 years through cubics,* Fluid Phase Equilibria **447**, 39 (2017).

[22] R. Sun, S. Lai, and J. Dubessy, *Calculations of vapor-liquid equilibria of the* $H_2O - N_2$ *and* $H_2O - H_2$ *systems with improved SAFT-LJ EOS,* Fluid Phase Equilibria **390**, 23 (2015).

[23] A. Rahbari, J. Brenkman, R. Hens, M. Ramdin, J. P. V. D. Broeke, R. Schoon, R. Henkes, O. A. Moultos, and T. J. H. Vlugt, *Solubility of Water in Hydrogen at High Pressure : a Molecular Simulation Study,* .

[24] J. D. Seader, *Separation Process Principles, 3rd Edition* (2006).

[25] T. C. Yan and K. Sciamanna, *High Pressure Hydrogen Design,* MIT Practice School Project Report (2017).

[26] C. J. B. Dicken and W. Mérida, *Measured effects of filling time and initial mass on the temperature distribution within a hydrogen cylinder during refuelling,* Journal of Power Sources **165**, 324 (2007).

[27] E. W. Lemmon, I. Bell, M. L. Huber, and M. O. McLinden, *NIST Standard Reference Database 23: Reference Fluid Thermodynamic and Transport Properties-REFPROP, Version 10.0, National Institute of Standards and Technology,* (2018).

[28] M. Monde, P. Woodfield, T. Takano, and M. Kosaka, *Estimation of temperature change in practical hydrogen pressure tanks being filled at high pressures of 35 and 70 MPa,* International Journal of Hydrogen Energy **37**, 5723 (2012).

[29] N. De Miguel, R. Ortiz Cebolla, B. Acosta, P. Moretto, F. Harskamp, and C. Bonato, *Compressed hydrogen tanks for on-board application: Thermal behaviour during cycling,* International Journal of Hydrogen Energy **40**, 6449 (2015).

[30] I. Simonovski, D. Baraldi, D. Melideo, and B. Acosta-Iborra, *Thermal simulations of a hydrogen storage tank during fast filling,* International Journal of Hydrogen Energy **40**, 12560 (2015).

[31] L. M. Robeson, *Polymeric Membranes for Gas Separation,* (2016), 10.1016/B978-0-12-803581-8.03297-5.

[32] M. Harasimowicz, P. Orluk, G. Zakrzewska-Trznadel, and A. G. Chmielewski, *Application of polyimide membranes for biogas purification and enrichment,* Journal of Hazardous Materials **144**, 698 (2007).

[33] M.-B. Hägg and X. He, *Chapter 15. Carbon Molecular Sieve Membranes for Gas Separation,* **2**, 162 (2011).

[34] M. Netusil and P. Ditl, *Comparison of three methods for natural gas dehydration,* Journal of Natural Gas Chemistry **20**, 471 (2011).

[35] C. Heald, H. W. Thompson, P. Roy Soc, and P. G. Menon, *Adsorption of Carbon Monoxide on Alumina at High Pressures,* Tech. Rep. 11 (1962).

[36] J. Vermesse, D. Vidal, and P. Malbrunot, *Gas Adsorption on Zeolites at High Pressure,* Tech. Rep. (1996).

[37] Y. Zhou and L. Zhou, *Fundamentals of High Pressure Adsorption †,* Langmuir **25**, 13461 (2009).

[38] *Triethylene Glycol,* Tech. Rep. XXX-0207X CRCG (The Dow Chemical Company, 2007).

[39] R. Ortiz Cebolla, B. Acosta, N. De Miguel, and P. Moretto, *Effect of precooled inlet gas temperature and mass flow rate on final state of charge during hydrogen vehicle refueling,* International Journal of Hydrogen Energy **40**, 4698 (2015).

[40] *SURFACE VEHICLE TECHNICAL INFORMATION REPORT,* Tech. Rep. (SAE Technical Standards, 2014).

[41] R. Hołyst and A. Poniewierski, *Thermodynamics for Chemists, Physicists and Engineers* (Springer, 2012) pp. 1–343.

[42] W. G. Gillespie P.C., *Vapor-liquid equilibrium data on water-substitute gas components:* $N_2 - H_2O$, $H_2 - H_2O$, $CO - H_2O$, $H_2 - CO - H_2O$, *and* $H_2S - H_2O$, GPA Research Rep. **Rep.No. RR-41**, 1 (1980).

[43] U. V.V., *Equilibrium compositions of vapor-gas mixtures over solutions,* Russ.J.Phys.Chem. **70(7)**, 1240 (1996).

[44] S. L.-T. D. Maslennikova V.Y., Goryunova N.P., *The solubility of water in compressed hydrogen.* Russ.J.Phys.Chem. **50(2)**, 240 (1976).

[45] K. P.-L. E. B. DeVaney W., Berryman J.M., *High temperature v-l-e measurements for substitute gas components,* GPA Research Rep. **Rep.No. RR-30**, 1 (1978).

[46] J. Smith, H. Van Ness, and M. Abbott, *Introduction to Chemical Engineering Thermodynamics. Sixth Edition in SI Units* (2001).

[47] O. J. Poling B.E., Prausnitz J.M., *The Properties of Gases and Liquids, fifth edition.*

[48] C.-t. Lin and T. E. Daubert, *Estimation of Partial Molar Volume and Fugacity Coefficient of Components in Mixtures from the Soave and Peng-Robinson Equations of State,* **1979**, 51 (1980).

[49] A. Drexhage, J.J. and Welsenes, *Physical properties of pure compounds. Parameters for the SMIRK equation of state,* Shell Internal Report (1990).

[50] T. Y. Kwak E H Benmekki and C. A. Ransoori, *VAN DER WAALS MIXING RULES FOR CUBIC EQUATIONS OF STATE (Applications for Supercritical Fluid Extraction Nodeling and Phase Equilibrium Calculations),* Tech. Rep.

[51] M. L. Michelsen, *Fluid Phase Equilibria,* Tech. Rep. (1990).

[52] J. Gross and G. Sadowski, *Perturbed-Chain SAFT: An Equation of State Based on a Perturbation Theory for Chain Molecules,* Ind. Eng. Chem. Res **40**, 1244 (2001).

[53] D. Marx and P. Nielaba, *Path-integral monte carlo techniques for rotational motion in two dimensions: Quenched, annealed, and no-spin quantum-statistical averages,* Phys. Rev. A **45**, 8968 (1992).

[54] W. L. Jorgensen, J. Chandrasekhar, J. D. Madura, R. W. Impey, and M. L. Klein, *Comparison of simple potential functions for simulating liquid water,* The Journal of Chemical Physics **79**, 926 (1983).

[55] J. Rowlinson, J. Baldwin, and A. Buckingham, *Liquids and Liquid Mixture,* 3rd ed. (1982) p. 328.

[56] T. Seward and E. Franck, *The System Hydrogen - Water up to 440°C and 2500 bar Pressure,* Ber. Bunsenges. Phys. Chem. **85**, 2 (1981).

[57] W. B. Streett, A. L. Erickson, and J. L. E. Hill, *PHASE EQUILIBRIA IN FLUID MIXTURES AT HIGH PRESSURES : THE* $He - CH_4$ *SYSTEM,* Phys. Earth Planet. Interiors **6**, 69 (1972).

[58] S. T. Handy, *Ionic Liquids - Classes and Properties* (InTech, 2011).

[59] J. F. Brennecke and E. J. Maginn, *Ionic liquids: Innovative fluids for chemical processing,* AIChE Journal **47**, 2384 (2001).

[60] Y. Y. Abe, T. Takekiyo, Y. Imai, and Hiroshi, *High Pressure Phase Behavior of Two Imidazolium-Based Ionic Liquids, [bmim][BF4] and [bmim][PF6],* Ionic Liquids Classes and Properties (2011), 10.5772/32009, arXiv:9809069v1 [arXiv:gr-qc] .

[61] M. Ramdin, T. W. De Loos, and T. J. H. Vlugt, *State-of-the-Art of* CO_2 *Capture with Ionic Liquids,* Ind. Eng. Chem. Res **51**, 8149 (2012).

[62] M. Hasib-Ur-Rahman, M. Siaj, and F. Larachi, *Ionic liquids for* CO_2 *capture-Development and progress,* Chemical Engineering and Processing **49**, 313 (2010).

[63] J. Huang and T. Rther, *Why are ionic liquids attractive for* CO_2 *absorption? An overview,* Australian Journal of Chemistry **62**, 298 (2009).

[64] E. Torralba-Calleja, J. Skinner, and D. Gutiérrez-Tauste, CO_2 *Capture in Ionic Liquids: A Review of Solubilities and Experimental Methods,* Journal of Chemistry **2013**, 1 (2013).

[65] F. Heym, J. Haber, W. Korth, B. J. Etzold, and A. Jess, *Vapor Pressure of water in mixtures with hydrophilic ionic liquids - A contribution to the design of processes for drying of gases by absorption in ionic liquids,* Chemical Engineering and Technology **33**, 1625 (2010).

[66] J. Kumelan, A. P.-S. K. Kamps, D. Tuma, and G. Maurer, *Solubility of* H_2 *in the Ionic Liquid* [BMIM][PF_6], J. Chem. Eng. Data **41**, 11 (2006).

[67] A. Kordi and F. Sabzi, *Thermodynamic modeling of hydrogen solubility in a series of ionic liquids,* International Journal of Hydrogen Energy , 1 (2018).

[68] V. V. Chaban and O. V. Prezhdo, *Computationally Efficient Prediction of Ionic Liquid Properties,* J. Phys. Chem. Lett **5**, 1973 (2014).

[69] J. Jacquemin, P. Nancarrow, D. W. Rooney, M. F. C. Gomes, P. Husson, V. Majer, A. A. H. Pádua, and C. Hardacre, *Prediction of Ionic Liquid Properties. II. Volumetric Properties as a Function of Temperature and Pressure,* Journal of chemical & engineerging data **53**, 2133 (2008).

[70] A. Fredenslund, R. L. Jones, and J. M. Prausnitz, *Group-Contribution Estimation of Activity Coefficients in Nonideal Liquid Mixtures,* AIChE Journal **21**, 1086 (1975).

[71] H. Grensemann and J. Gmehling, *Performance of a Conductor-Like Screening Model for Real Solvents Model in Comparison to Classical Group Contribution Methods,* Ind. Eng. Chem. Res **44**, 1610 (2005).

[72] J. Lohmann, R. Joh, and J. Gmehling, *From UNIFAC to Modified UNIFAC (Dortmund),* Ind. Eng. Chem. Res **40**, 957 (2001).

[73] A. Klamt, *Conductor-like Screening Model for Real Solvents: A New Approach to the Quantitative Calculation of Solvation Phenomena Starting from the question of why dielectric continuum models give a fairly good description of molecules,* J. Phys. Chem **99**, 2224 (1995).

[74] E. Mullins, R. Oldland, Y. A. Liu, S. Wang, S. I. Sandler, C.-C. Chen, M. Zwolak, and K. C. Seavey, *Sigma-Profile Database for Using COSMO-Based Thermodynamic Methods,* Ind. Eng. Chem. Res **45**, 4389 (2006).

[75] K. Guo, Y. Bi, L. Sun, H. Su, and L. Hungpu, *Experiment and Correlation of Vapor-Liquid Equilibrium of Aqueous Solutions of Hydrophilic Ionic Liquids: 1-Ethyl-3-methylimidazolium Acetate and 1-Hexyl-3-methylimidazolium Chloride,* Journal of chemical & engineering data **57**, 2243 (2012).

[76] G. Gonfa, M. A. Bustam, A. M. Sharif, N. Mohamad, and S. Ullah, *Tuning ionic liquids for natural gas dehydration using COSMO-RS methodology,* Journal of Natural Gas Science and Engineering **27**, 1141 (2015).

[77] M. Mohammadi, M. Asadollahzadeh, and S. Shirazian, *Molecular-level understanding of supported ionic liquid membranes for gas separation,* Journal of Molecular Liquids **262**, 230 (2018).

[78] C. Jork, C. Kristen, D. Pieraccini, A. Stark, C. Chiappe, Y. A. Beste, and W. Arlt, *Tailor-made ionic liquids,* J. Chem. Thermodynamics **37**, 537 (2005).

[79] *Ddbst - dortmund data bank software & separation technology gmbh, activity coefficient calculation,* (2017 (2.9.0.24)).

[80] Sigma-Aldrich, *The Global Harmonised System (GHS),* Tech. Rep.

[81] L. Wu, W. Geng, L. Gao, J. Chen, and H. Zhao, *Study of Gas Dehydration Process by Ionic Liquid Method in a Rotating Packed Bed,* Energy and Fuels **31**, 13400 (2017).

[82] P. Scovazzo, *Testing and evaluation of room temperature ionic liquid (RTIL) membranes for gas dehumidification,* Journal of Membrane Science **355**, 7 (2010).

[83] F. Radakovitsch, F. Heym, and A. Jess, *Gas Drying Using Supported Ionic Liquids,* CHEMICAL ENGINEERING TRANSACTIONS **69** (2018).

[84] M. G. Freire, C. M. S. S. Neves, I. M. Marrucho, J. A. P. Coutinho, and A. M. Fernandes, *Hydrolysis of Tetrafluoroborate and Hexafluorophosphate Counter Ions in Imidazolium-Based Ionic Liquids †,* J. Phys. Chem. A **114**, 3744 (2010).

[85] S. Fendt, S. Padmanabhan, H. W. Blanch, and J. M. Prausnitz, *Viscosities of Acetate or Chloride-Based Ionic Liquids and Some of Their Mixtures with Water or Other Common Solvents,* J. Chem. Eng. Data **56**, 31 (2011).

[86] E. Quijada-Maldonado, S. Van Der Boogaart, J. H. Lijbers, G. W. Meindersma, and A. B. De Haan, *Experimental densities, dynamic viscosities and surface tensions of the ionic liquids series 1-ethyl-3-methylimidazolium acetate and dicyanamide and their binary and ternary mixtures with water and ethanol at T = (298.15 to 343.15 K),* J. Chem. Thermodynamics **51**, 51 (2012).

[87] H. Saba, X. Zhu, Y. Chen, and Y. Zhang, *Determination of physical properties for the mixtures of* [BMIM]Cl *with different organic solvents,* Chinese Journal of Chemical Engineering **23**, 804 (2015).

[88] M. H. Ghatee and A. R. Zolghadr, *Surface tension measurements of imidazolium-based ionic liquids at liquid-vapor equilibrium,* Fluid Phase Equilibria **263**, 168 (2008).

[89] M. P. Singh, S. K. Mandal, Y. L. Verma, A. K. Gupta, R. K. Singh, and S. Chandra, *Viscoelastic, Surface, and Volumetric Properties of Ionic Liquids* [BMIM][OcSO$_4$]*,* [BMIM][PF$_6$]*, and* [EMIM][MeSO$_3$]*,* Journal of chemical & engineering data **59** (2014), 10.1021/je5000617.

[90] Y. Cao and T. Mu, *Comprehensive Investigation on the Thermal Stability of 66 Ionic Liquids by Thermogravimetric Analysis,* Industrial and Engineering Chemistry Research **53**, 8651 (2014).

[91] I. Cantat, S. Cohen-Addad, F. Elias, F. Graner, R. Hohler, O. Pitois, F. Rouyer, and A. Saint-Jalmes, *Foams structure and Dynamics*, edited by S. Cox, September (Oxford, 2010).

[92] M. Moosavi, F. Khashei, A. Sharifi, and M. Mirzaei, *The effects of temperature and alkyl chain length on the density and surface tension of the imidazolium-based geminal dicationic ionic liquids,* The Journal of Chemical Thermodynamics **107**, 1 (2017).

[93] T. F. HOLDEN, N. C. Aceto, and E. F. Schoppet, *EFFECTS OF VISCOSITY AND TEMPERATURE ON THE FOAMING CHARACTERISTICS OF CONCENTRATED WHOLE MILK,* journal of dairy science , 359 (1964).

[94] Z. Zhang, R. Yang, W. Gao, and X. Yao, *Investigation of* [Emim][OAc] *as a mild pretreatment solvent for enhancing the sulfonation efficiency of alkali lignin,* RSC Advances **7**, 31009 (2017).

[95] Y.-S. Ye, J. Rick, and B.-J. Hwang, *Ionic liquid polymer electrolytes,* J. Mater. Chem. A **1**, 2719 (2013).

[96] J. G. Huddleston, A. E. Visser, W. M. Reichert, H. D. Willauer, G. A. Broker, and R. D. Rogers, *Characterization and comparison of hydrophilic and hydrophobic room temperature ionic liquids incorporating the imidazolium cation,* Green Chemistry **3**, 156 (2001).

A

EXPERIMENTAL PROCEDURE

This appendix includes the used materials and apparatus.

A.1. MATERIALS

IONIC LIQUIDS

Ionic Liquid	Purity	Supplier
[BMIM][Chloride]	Purity >98%	Sigma Aldrich
[EMIM][Acetate]	Purity >97%	Alfa Aesar
[BMIM][Octyl Sulfate]	Purity >99%	Alfa Aesar
[EMIM][Ethyl Sulfate]	Purity >95%	Sigma Aldrich

OTHER CHEMICALS

Substance	Purity	Supplier
Hydrogen	hydrogen 3.0 dry, Purity >99.9%, H_2O < 50 ppmw	
Nitrogen	nitrogen 5.0, Purity >99.999%	
Methanol	H_2O < 20 ppmw,	VWR Chemicals
KF coulomat	CombiCoulomat fritless	Merck Milipore

A.2. APPARATUS

Equipment	Specifications	Range
Hydrogen purifier	HEA EP40	max 21 bar and 300°C
Hydrogen sensor	ap2e ProCeas	0-550ppmv - H_2O/CO/CH_4/NH_3/H_2S/CO_2
Water bath	Julabo F32 Mw-basis	10°C - 210°C
Karl Fischer apparatus	coulometric, fritless	
Mass flow controller	Brooks	0-200 Nl/h

A.3. WATER CONTENT REGULATION
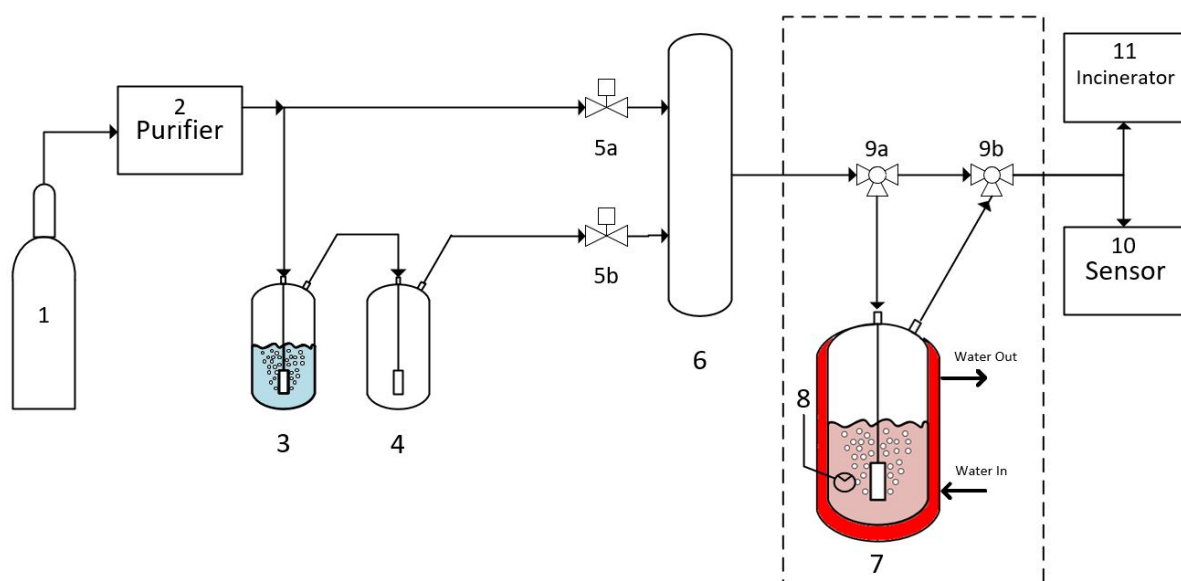
Figure A.1: Schematic diagram of experimental apparatus. 1, Hydrogen gas storage; 2, purifier; 3, water scrubber; 4, buffer vessel; 5(a&b), computer valves; 6, mixing vessel; 7, IL scrubber; 8, thermocouple; 9(a&b), three-way hand valves; 10, Sensor; 11, Incinerator.

The hydrogen gas was hydrated by flowing dry hydrogen gas through water (3) (see Fig. A.1). Thereafter, the hydrogen flowed through cylinder 4, to make sure no liquid water was left in the hydrogen gas. The drawback of this unit was that the sensor could not measure water content >550 ppmv. Higher water content was required though as input, to make sure the ILs could absorb water. This problem was solved by increasing the flow rate of valve 5a significantly. The resulting water content was measured at a flow rate of 150 NL/h for 5a, and 10.67 Nl/h for 5b. This way, it was calculated that the water content of the saturated hydrogen was 6578 ppmv. For the absorption experiment, the flow rate through 5b was alway kept constant, as a change in flow rate could have an impact on the hydration process. The saturated hydrogen was diluted with hydrogen, which resulted in a constant flow rate of 40 Nl/h with a water content of 1755 ppmv.

A.4. IONIC LIQUID SCRUBBER

Technical drawing — Shell Standard Drawing, H2 Contamination Unit (2016), Scrubber V-410.
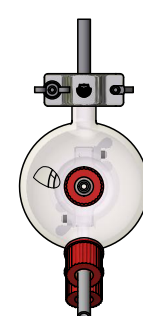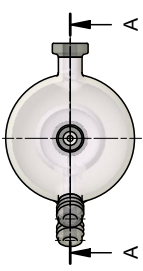
DESIGN CONDITIONS

Registration Number (s): D6618
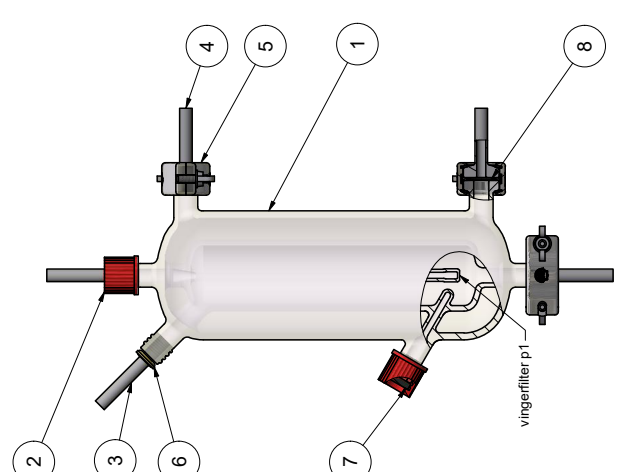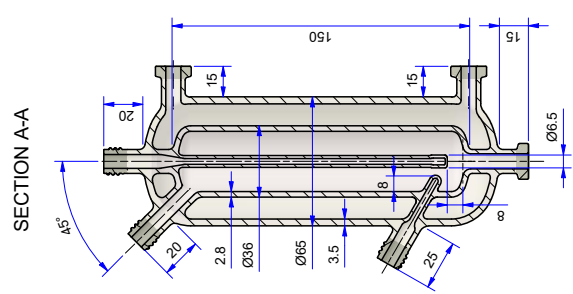
PED Category: Art. 4, Par. 3 — Cat. I ☒ Mod. / Cat. II ☐ Mod. / Cat. III ☐ Mod. / Cat. IV ☐ Mod.
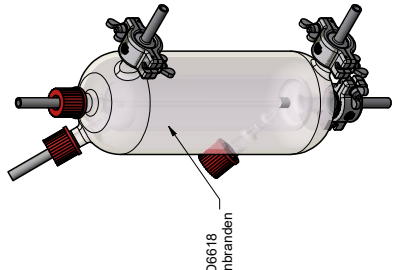
ACC.: DIRECTIVE 2014/68/EU

Vessel Tag no.	Max working Pressure Barg	Design Pressure Barg	Max working Temp. °C	Design Temp. °C	Test Pressure Barg New	Test Pressure Barg Inspection	Vessel Volume Inner Vessel 100ml	Vessel Volume Outer Vessel 60ml
V-410		4		60	5.7			

ITEM	QTY	DESCRIPTION	DIMENSIONS	MATERIAL	REMARKS
8	3	O-ring speedflens 12	10.82 x 1.78	Kalrez 6375	AS 013
7	1	Septum GL14 dop		Siliconen rubber	
6	2	O-ring 6.02x2.62		Kalrez 6375	AS 108
5	3	Assembly Speed Clamp 12		Aluminium	
4	3	Speedflens 12-3_8 tubing		AISI 316	Siliceren
3	2	GL14->1/4" Tubing		AISI 316L	Siliceren
2	3	GL14 open dop		PPS	Schott
1	1	Assembly Scrubber V-410		Borosilicaatglas	

GENERAL TOLERANCES ACC. ISO 2768-mK
SURFACE ROUGHNESS ACC. ISO 1302/4287

PREFERRED RANGE
ROUGHNESS Ra in µm (0,001 mm)   3.2 ▽ 1.6 ▽ 0.8 ▽ 0.4 ▽

ISSUE	DATE			
	20/12/18	Ref. Designer	Ref. Designer	
			APPROVED BY	

PROJECTION METHOD

H2 Contamination Unit (2016)
Scrubber V-410

STANDARD DRAWING

SCALE:
UNITS: mm   ID 6667   Sheet No. 001 of   Size: A3

DRG No. 6667 - 18 - 3100   Rev. 0

SHELL GLOBAL SOLUTIONS INTERNATIONAL B.V.
SHELL INTERNATIONAL EXPLORATION AND PRODUCTION B.V.

SECTION A-A

D6618 inbranden

vingerfilter p1

B

SOLUBILITY OF WATER IN HYDROGEN AT HIGH PRESSURE: A MOLECULAR SIMULATION STUDY

The following paper is submitted to the Journal of Chemical and Engineering Data.
https://pubs.acs.org/journal/jceaax

Solubility of Water in Hydrogen at High Pressure: a Molecular Simulation Study

Ahmadreza Rahbari,[†] Jeroen Brenkman,[‡] Remco Hens,[†] Mahinder Ramdin,[†] Leo J. P. van den Broeke,[†] Rogier Schoon,[‡] Ruud Henkes,[‡] Othonas A. Moultos,[†] and Thijs J. H. Vlugt[*,†]

†*Engineering Thermodynamics, Process & Energy Department, Faculty of Mechanical, Maritime and Materials Engineering, Delft University of Technology, Leeghwaterstraat 39, 2628CB, Delft, The Netherlands*

‡*Shell Global Solutions International, PO Box 38000, 1030BN, Amsterdam, the Netherlands*

E-mail: t.j.h.vlugt@tudelft.nl

Abstract

Hydrogen is one of the most popular alternatives for energy storage. Due to its low volumetric energy density, hydrogen should be compressed for practical storage and transportation purposes. Recently, Electrochemical Hydrogen Compressors (EHC) have been developed that are capable of compressing hydrogen up to $P = 1000$ bar, and have the potential of reducing compression costs to 3 kWh/kg. As EHC compressed hydrogen is saturated with water, the maximum water content in gaseous hydrogen should meet the fuel requirements issued by the International Organization for Standardization (ISO) when refuelling Fuel Cell Electric Vehicles (FCEV). The ISO 14687-2:2012 standard has limited the water concentration in hydrogen gas to 5 μmol water per mol hydrogen fuel mixture. Knowledge on the vapor liquid equilibrium of $H_2O - H_2$ mixtures is crucial for designing a method to remove H_2O from compressed H_2. To the best of our knowledge,

the only experimental high pressure data ($P > 300$ bar) for $H_2O - H_2$ phase coexistence is from 1927 [J. Am. Chem. Soc., 1927, 49, pp 65-78]. In this paper, we have used molecular simulation and thermodynamic modelling to study the phase coexistence of the $H_2O - H_2$ system for temperatures between $T = 283$ K to $T = 423$ K and pressures between $P = 10$ bar and $P = 1000$ bar. It is shown that the PR-EoS and SRK-EoS with van der Waals mixing rules fail to accurately predict the equilibrium coexistence compositions of the liquid and gas phase, with or without fitted binary interaction parameters. We have shown that the solubility of water in compressed hydrogen is adequately predicted using force field based molecular simulations. The modelling of phase coexistence of $H_2O - H_2$ mixtures will be improved by using polarizable models for water. In the Supporting Information, we present a detailed overview of available experimental VLE and solubility data for the $H_2O - H_2$ system at high pressures.

1   Introduction

The world population is expected to grow rapidly, from 7.6 billion currently, to about 9.8 billion in 2050.[1] Due to increasing prosperity, the worldwide consumption of energy per individual will also increase. Even in the current modern world, several billion people still do not have access to basic needs, such as clean water, sanitation, nutrition, health care, and education.[2] These are all examples of the Sustainable Development Goals, adopted by all United Nations Member States in 2015.[2] Access to energy is a key enabler to reach these basic needs. The worldwide energy demand is therefore expected to increase by 40% by 2040.[3] At the same time, CO_2 emissions need to be reduced to reach the goals of the Paris agreement.[4] 80% of the total primary energy supply is currently produced by fossil fuels, such as coal, oil, and natural gas.[3] To reach the goals of the Paris agreement, attempts are made to replace fossil fuels with renewable alternatives such as wind and solar (PV) energy. Current expectations are that by 2040, 40% of the total generated electricity will be from renewable energy sources.[3]

Unlike fossil fuels, energy production from intermittent renewable sources, including wind power and solar energy, critically depend on the availability of these sources leading to an uncontrollable energy output.[5] For direct integration to the power grid, uncontrollable availability of intermittent renewable energy sources within 10% of the installed capacity is acceptable without major technical problems.[5] However, large scale integration of intermittent energy sources above this limit is expected to cause frequent mismatches between the supply and demand of energy. To avoid this, integration of energy storage technologies is proposed as one of the promising solutions for stable and flexible supply of electricity.[6,7] Different types of technologies have been developed for electrical energy storage including: hydro storage, flywheels, batteries, and hydrogen produced by electrolysis etc.[5,6,8,9] One of the most popular alternatives for energy storage is hydrogen.[8] Hydrogen has the advantage that it can be stored for long periods and converted to electricity without pollution.[10] Hydrogen has a broad span of applications, like fuel cells, fuel for heating, transportation, or even as a raw material for the chemical industry.[5,10,11] Since hydrogen has a very low density at standard conditions, it has a very low volumetric energy density. For practical storage and transportation purposes, the density of hydrogen must be increased significantly.[12] The density of hydrogen can be increased by compression, cooling, or a combination of both, depending on the scale and application.[12] One of the emerging applications for hydrogen is found in sustainable transportation.[10] In Fuel Cell Electric Vehicles (FCEV), hydrogen is stored in compressed form in pressurized cylinders at $P = 350$ bar or $P = 700$ bar.[12] In practice, a passenger car needs a tank capacity of around 100 to 150 litres to store 4 to 6 kg of hydrogen, which provides a range of approximately 500 km.[12] High pressure storage tanks with pressures of at least $P = 875$ bar[12,13] are installed at refuelling stations, to fuel a vehicle within the target time of three to five minutes.[12] Conventional compressor types that are currently used are piston, compressed air, diaphragm, or ionic compressors, depending mainly on the capacity of the refuelling station.[12] The conventional compressor requires on average 6 kWh/kg of energy to compress hydrogen from 10 to 400 bar.[13]

An alternative compressor is the Electrochemical Hydrogen Compressor (EHC). HyET has developed an EHC that works with pressures up to 1000 bar, and has the potential of bringing compression costs down to 3 kWh/kg.[13] The working principle of an EHC operation is similar to a Proton Exchange Membrane (PEM) fuel cell.[14] A single EHC stack consists of a low pressure and a high pressure side, separated by a membrane that is only permeable for hydrogen protons, and not for molecules. The membrane is positioned between two platinum catalysts containing electrodes. Once a potential difference is applied over the electrodes, a hydrogen molecule splits into two protons. The protons then travel through the membrane where conversion to hydrogen molecules takes place at elevated pressure.[14] In the EHC, the proton transfer through the membrane is enabled by water. The EHC has several advantages compared to traditional technologies:[13,15–17] *(1)* the EHC has a higher efficiency, especially at high compression ratios.[18] In theory, the compression ratio using EHC can go to infinity, from an electrochemical perspective. The mechanical strength and back diffusion losses are the main limitations for higher pressure ratios for the EHC;[18] *(2)* due to the highly selective membrane that only allows the permeation of protons, contaminants are prevented from passing the membrane.[18] This means that the EHC performs both as a compressor and a purifier of hydrogen gas;[18] *(3)* the compressor has no moving parts, resulting in lower maintenance costs and making lubricants, which may contaminate the compressed hydrogen, redundant; *(4)* the EHC operates silently, since it has no rotating parts. This makes the EHC suitable for locations such as refuelling stations, where acoustical emission is a constraint; *(5)* the EHC is a compact device that is well suited to scale up.[18] Disadvantages of the EHC are similar to those of fuel cells, mainly high material costs. For instance, the platinum catalyst which is required to resist the corrosive environments in the compressor, is very expensive.[18] Another disadvantage is related to the proton transport through the membrane. Water enables the proton transport through the membrane and therefore the membrane always needs to be hydrated.[19] Therefore, the resulting hydrogen gas is saturated with water which can be an issue depending on the application. The International Organization for Standardization

(ISO) stated that water provides a transport mechanism for water-soluble contaminants such as K^+ and Na^+ when present as an aerosol.[20] Both K^+ and Na^+ can affect the fuel cell and are not recommended to exceed 0.05 µmol K^+ or Na^+ per mol hydrogen fuel mixture.[20] To avoid potential issues, the ISO has directed the maximum allowed concentration of impurities for gaseous hydrogen, including water in Table 1 of the ISO 14687-2:2012.[20] The maximum concentration of water in the gaseous hydrogen, used for PEM fuel cells in road vehicles is limited to 5 µmol water per mol hydrogen fuel mixture.[20] This poses two important questions: *(1)* what is the solubility of water in hydrogen at high pressures? *(2)* if this solubility is too large, what is the best method to reduce the water content? To answer these questions, an accurate description of Vapor Liquid Equilibrium (VLE) of the $H_2O - H_2$ system at high pressures is required. Published experimental data that describe these systems is scarce. To the best of our knowledge, the only experimental data describing phase coexistencce of $H_2O - H_2$ for pressures exceeding 300 bar are from 1927 (limited to $T = 323$ $K^{[21]}$). Wiebe and Gaddy studied also the solubility of hydrogen gas in liquid water at high pressures up to $P = 1013.25$ bar.[22] Therefore, molecular simulation and thermodynamic modelling are needed to determine the water content in the compressed hydrogen. In industrial applications, cubic type Equations of State (EoS) are one the most commonly used methods to study VLE, because of their simplicity.[23–27] In this work, the Peng-Robinson (PR) EoS and the Soave Redlich-Kwong (SRK) EoS with van der Waals mixing rules are used to predict the phase coexitence of $H_2O - H_2$ at elevated pressures. However, molar volumes of the liquid phase and fugacity coefficients at high pressures obtained from PR-EoS and SRK-EoS modelling (with conventional mixing rules) are known to deviate significantly from experiments.[28–31]

In this work, it is shown that both the PR-EoS and SRK-EoS fail to describe the liquid phase and the gas phase compositions, with or without fitted binary interaction parameters (k_{ij}'s). Since water is a highly polar molecule, either modifications of the conventional mixing rules are required,[24] or more physically based models (*i.e.* SAFT types $EoS^{[32]}$ or molecular $simulations^{[33]}$) should be used to describe the phase behavior of the $H_2O - H_2$ system.[32] It

was found that a temperature dependent parameter k_{ij} is still required for SAFT type EoS modelling.[34] Therefore, force field based molecular simulation could be considered as a natural tool to study the phase coexistence of the $H_2O - H_2$ system. In this work, different molecular force fields for water and hydrogen are considered for describing the phase coexistence compositions of the liquid and gas phase of the $H_2O - H_2$ system, especially at high pressures. To evaluate the accuracy of the results from molecular simulations, we have performed an extensive literature survey on the VLE of $H_2O - H_2$ mixtures, at high pressures.[21,22,35–42] In this work, it is shown that the best predictions of the VLE of the $H_2O - H_2$ system at high pressures (in both phases) are obtained using molecular simulations. No adjustable k_{ij}'s were used for molecular simulations in this study.

This paper is organized as follows. In Section 2, the molecular simulation techniques used in this study are explained and simulation details (molecular simulations and EoS modelling) and force field details for water and hydrogen are provided. Our results obtained from molecular simulations and EoS modelling are presented and compared with experimental data in Section 3. Our conclusions are summarized in Section 4. In the Supporting Information, we present a detailed overview of available experimental VLE and solubility data for the $H_2O - H_2$ system at high pressures.

2 Modelling and Methodology

2.1 Simulation Techniques

The natural choice for VLE phase equilibrium calculations is the Gibbs Ensemble (GE) method introduced by Panagiotopoulos,[43–45] which is used extensively in molecular simulation studies.[33] In the GE, the vapor and liquid phase are simulated in two simulation boxes, which can exchange molecules, volume and energy. At coexistence, the pressures, temperatures and chemical potentials of each component are equal in both boxes.[33] The GE is reliable, and the finite size effects are small unless conditions close to the critical point are considered.[46,47] To

6

accurately predict coexistence densities, simulations in the GE rely on sufficient molecule exchanges between the two phases.[33,44] The well-known drawback of the conventional GE is that at high densities, particle insertions/deletions have a low acceptance probability, also leading to poor estimates of chemical potentials in both phases. Although chemical potentials of different component types are not strictly needed for calculating the coexistence densities, the equality of chemical potentials is an important condition for phase equilibrium. Chemical potential calculations in the GE follow from a modification of the Widom's Test Particle Insertion (WTPI),[33,48] taking fluctuations in density into account. It is well known that WTPI method often performs poorly for dense liquids.[49,50]

Based on the work of Shi and Maginn,[51,52] Vlugt and co-workers expanded the conventional GE with so-called fractional molecules to improve the efficiency of molecule exchanges between the simulation boxes.[53,54] In contrast to the normal or "whole" molecules, the interactions of fractional molecules are scaled between zero and one with a coupling parameter λ_i. $\lambda_i = 0$ means that the fractional molecule of type i has no interactions with the surrounding molecules and acts as an ideal gas molecule. $\lambda_i = 1$ means that the fractional molecule of type i has fully scaled interactions and interacts as a whole molecule. The fractional molecule of each component type can be in either one of the phases.[53] In addition to the conventional thermalization trial moves (translation, rotation and volume changes), three additional trial moves are associated with the fractional molecule of each component: *(1)* changes in λ_i while keeping the positions and orientations of all molecules including the fractional molecule(s) fixed; *(2)* Reinsertion of the fractional molecule to a randomly selected position in the other simulation box (phase) while keeping the value of λ_i, positions and orientations of all other molecules fixed; *(3)* Changing the identity of the fractional molecule with a randomly selected molecule of the same type in the other box, while keeping the value of λ_i, positions and orientations of all molecules fixed. The use of fractional molecules significantly improves the efficiency of the VLE calculations and the calculations of chemical potentials at coexistence. For details, the reader is referred to Refs.[49,53,55]

Since molecule exchanges in the Continuous Fractional Component GE (CFCGE) are performed using fractional molecules with scaled interactions, molecule transfers between coexisting phases are facilitated leading to a more efficient sampling of coexistence densities. The chemical potential of component type i in phase j (gas or liquid) is obtained from:[53,54]

$$\mu_{ij} = k_{\mathrm{B}} T \ln \frac{\langle \rho_{ij} \rangle}{\rho_0} - k_{\mathrm{B}} T \ln \left(\frac{p(\lambda_{ij} = 1)}{p(\lambda_{ij} = 0)} \right) \tag{1}$$

where k_{B} is the Boltzmann constant, ρ_{ij} is the number density of component i in phase j and $p(\lambda_{ij})$ is the probability distribution of λ_{ij} in phase j. The term ρ_0 is an arbitrary reference density to make the argument of the logarithm dimensionless. The first term on the right hand side of Eq. 1 is the ideal gas contribution of the chemical potential (μ_{ij}^{id}). The second term on the right hand side of Eq. 1 is the excess chemical potential (μ_{ij}^{ex}). The brackets $\langle \cdots \rangle$ denote an ensemble average. The fugacity coefficient of component type i in phase j follows from:

$$\phi_{ij} = \frac{1}{Z_{\mathrm{mix}}} \times \frac{p(\lambda_{ij} = 0)}{p(\lambda_{ij} = 1)} \tag{2}$$

where Z_{mix} is the compressibility factor of the mixture. Eq. 2 is derived in the Supporting Information. Based on the limited experimental solubility data available in literature at $T = 323$ K and pressures above $P = 300$ bar,[21] we know that the solubility of water in the gas phase at high pressures ($P = 100$ bar to $P = 1000$ bar) is about a couple of hundred PPMs (molar), or less. At lower temperatures, due to the low the solubility of water in hydrogen, a very large number of hydrogen molecules (up to a million) in the gas phase would be required in the simulations to have on average a single water molecule in the gas phase. The solubility of hydrogen in the liquid phase is also very low, e.g. mole fractions ranging from between 0.003 to 0.115 at $T = 323$ K and pressures between of $P = 25$ bar and $P = 1000$ bar. This makes most simulations of the $\mathrm{H_2O - H_2}$ system in the CFCGE at low temperatures and high pressures impractical, as a very large system is needed to have at least

8

a single component of each type in each box. One could in principle simulate the VLE of $H_2O - H_2$ in the CFCGE using a smaller system size. This would lead to poor statistics for the average number of H_2 molecules in the liquid phase, and H_2O molecules in the gas phase. To circumvent these issues, both the gas and liquid phases (almost pure hydrogen gas and pure liquid water, respectively) are simulated independently in the Continuous Fractional Component NPT (CFCNPT) ensemble.[55] By varying the mixture composition in the gas and liquid phases around the equilibrium state, the coexistence compositions are obtained by imposing equal chemical potentials for both phases. Vlugt and co-workers considered the conventional NPT ensemble expanded with a fractional molecule,[55] similar to earlier work with the GE.[53] Similar to the CFCGE, trial moves for the fractional molecule are performed in addition to the usual thermalization moves. The only difference is that in the simulations in the CFCNPT ensemble, the trial moves related to the fractional molecule are performed in the same simulation box. By applying the CFCMC method to the NPT ensemble, one can calculate the chemical potential of each species (similar to Eq. 1). For details the reader is referred to Refs.[55,56]

At high pressures we know that the solute is almost pure in both phases, *i.e.* hydrogen in the gas phase and water in the liquid phase. For a solution close to infinite dilution, one can express the variation of the excess chemical potential of the solute, *i.e.* hydrogen in the liquid phase and water in the gas phase as a function of the number density of the solute:

$$\mu_{ij}^{\text{ex}}(\rho_{ij}) = A_{ij} + B_{ij}\rho_{ij} + C_{ij}\rho_{ij}^2 + \cdots \tag{3}$$

To obtain the terms A_{ij}, B_{ij}, $\cdots$, multiple simulations are performed at constant temperature and pressure, for different concentrations of the solute. In the region of interest (very dilute solutions) $\mu_{ij}^{\text{ex}}(\rho_{ij})$ depends linearly on the number density. As the solvent in both phases is almost a pure component, one can assume that the excess chemical potential of the solvent is independent of the number of few solute molecules in that phase. The coexistence densities

are then obtained by imposing equal chemical potentials of each component using Eq. 3. Note that at conditions where both methods are applicable to obtain phase coexistence (*i.e.* simulations in the GE and the CFC*NPT* ensemble), we have verified that both methods (*i.e.* GE and imposing equal chemical potentials) yield the same results.

2.2   Simulation Details

Depending on the temperature and pressure, molecular simulations are performed in the CFCGE or in the CFC*NPT* ensemble. All simulations were performed using our in-house code. It was verified that our results are identical to those from the RASPA software package.[57,58] In all simulations, periodic boundary conditions were used. All molecules are rigid and the interactions between the molecules only consist of LJ and Coulombic interactions. LJ potentials were truncated but not shifted. Analytic tail corrections and the Lorentz-Berthelot mixing rules were applied.[33,59] To treat the electrostatic interactions, the Ewald summation was used with a relative precision of 1×10^{-6}. In CFCGE simulations of $H_2O - H_2$ mixtures, fractional molecules of water and hydrogen are present which are used to facilitate molecule exchanges between the phases. To protect the charges from overlapping, the (repulsive) LJ interactions of the fractional molecules are switched on before the electrostatics.[60–65] For details about scaling the LJ and Coulombic interactions of the fractional molecule, the reader is referred to Refs.[54,56,66] Details about the force field parameters for different water and hydrogen models and cutoff radii for LJ interactions are provided in tables S1 and S2 of the Supporting Information.

Simulations in the CFCGE ensemble were started with 730 molecules of water and 600 molecules of hydrogen. For all temperatures and pressures, 10^5 equilibration cycles were carried out followed by $4 \cdot 10^6$ production cycles. Each MC cycle consists of N_{MC} Monte Carlo trial moves, where N_{MC} equals the total number of molecules, with a minimum of 20. Trial moves in the CFCGE simulations were selected with the following probabilities: 1% volume changes, 35% translations, 30% rotations, 17% λ changes, 8.5% reinsertions of fractional

molecules at randomly selected positions in the other box, and 8.5% identity changes of fractional molecules between the boxes. Independent CFCNPT simulations of the liquid phase, close to infinite dilution of hydrogen, were performed with 730 water molecules with $N_{H_2} \in \langle 0, 10 \rangle$ hydrogen molecules. Similarly, independent CFCNPT simulations of the gas phase, close to infinite dilution of water, were performed with 600 hydrogen molecules with $N_{H_2O} \in \langle 0, 7 \rangle$ water molecules. Trial moves in the CFCNPT simulations were selected with the following probabilities: 1% volume changes, 35% translations, 30% rotations, 17% λ changes, 8.5% reinsertions of fractional molecules at randomly selected positions, and 8.5% identity changes of fractional molecules.

2.3 Force Fields

To model the VLE of $H_2O - H_2$ mixtures, molecular force fields are considered to predict the density and composition of the gas and liquid phases. As the most commonly used force fields are developed based on single-phase coexistence data,[67,68] we have screened these force fields using single-phase hydrogen (gas phase) and single-phase water (liquid phase) simulations. Force fields for water and hydrogen are selected based on predicting bulk properties of pure phases such as densities, chemical potentials and fugacity coefficients. The densities and fugacity coefficients of molecular hydrogen in the gas phase are computed at different pressures using several force fields from the literature. The results are compared with REFPROP.[69,70] Common force fields for molecular hydrogen in literature include single site,[71–73] two-site[74] and multi-site potentials with (permanent) charge interactions.[75–77] Single-site hydrogen models are capable of predicting bulk thermodynamic properties of hydrogen accurately. The single-site hydrogen model by Buch[71] reproduces the bulk properties of hydrogen accurately up to high pressures. Multi-site hydrogen potentials that consider charge-quadrupoles and polarizability are more relevant for modeling hydrogen sorption in highly heterogeneous systems.[74,75,77–80] The densities and the excess chemical potentials predicted by different force fields of water in the liquid phase are computed as a function of pressure.

The results are compared to those obtained from REFPROP.[69,81] Even though water is a flexible and polarizable molecule, to date most molecular simulations studies consider rigid molecular potentials of water with constant point-charges.[68,82–85] It is computationally advantageous to use these simplified water potentials, which can predict thermodynamic and transport properties of water in good agreement with experiments. To obtain a more physical description of water, polarizable force fields have been developed to account for polarization effects.[68,86–95] Compared to the fixed-charge water potentials, thermodynamic properties of polarizable force fields are not fully known.[87] Commonly used fixed-charge force fields for water are three-site potentials: TIP3P,[96] SPC[97,98] and SPC/E,[99] four-site potentials: TIP4P/2005,[83] TIP4P/Ew,[100] OPC,[67] and a five-site potential: TIP5P/Ew.[101] In our previous studies,[49,56] we have shown that the computed excess chemical potentials of water for the three-site potentials TIP3P and SPC are in good agreement with values obtained from an empirical Helmholtz equation of state[81] based on experimental data.[70] It is well-known that the TIP4P/2005 water outperforms the three-site models for predicting bulk properties of water such as the density.[83] In our previous studies, we have shown that the computed excess chemical potentials of water obtained from four-site and five-site potentials show larger deviations from experimental data compared to three-site potentials[49] .

2.4 Equation of State Modelling

The PR-EoS[102] and SRK-EoS[103] with the conventional van der Waals mixing rules are used to predict the $H_2O - H_2$ VLE. These equations of state are the most widely used in industry and perform best for describing the VLE of non-polar mixtures.[104] It is well-known that the molar volume of the liquid phase predicted by cubic equations of state is inaccurate.[105,106] Since the solubility of small gas nonpolar molecules in the liquid phase are dominated by entropic effects (*i.e.*, molar volume), the solubility of H_2 in H_2O is predicted poorly. We have used both zero k_{ij}'s and k_{ij}'s fitted on high pressure experimental data. Details on the EoS modelling are provided in the Supporting Information.

3 Results and Discussion

3.1 Molecular Simulations

The densities and the fugacity coefficients of pure hydrogen between $P = 100$ bar and $P = 1000$ bar obtained from CFCNPT simulations and EoS modelling are compared to those obtained from REFPROP,[107] see Fig. 1. Since the differences between the results obtained for $P < 400$ bar is very small, only the results between $P = 400$ bar and $P = 1000$ bar are shown, and the raw data are provided in table S3 of the Supporting Information. Hydrogen models used for this study include single-site models: $i.e.$ Hirschfelder,[72] Vrabec,[73] Buch,[71] two-site model: $i.e.$ Cracknell[74] and the multi-site model of Marx.[77] It is clear that the densities obtained using the Buch[71] and Marx[77] force fields are in excellent agreement with experimental data up to $P = 1000$ bar. The results obtained from the PR-EoS and SRK-EoS deviate from experimental data for $P > 400$ bar. The calculated fugacity coefficients of pure hydrogen in the gas phase are best predicted using the Buch[71] and Marx[77] force fields. The calculated fugacity coefficients from the SRK-EoS are in excellent agreement with experiments. The simulation results show that both the Buch and Marx force fields outperform the other molecular models in predicting bulk densities and fugacity coefficients of hydrogen at high pressures. This means that considering a quadrupole moment for hydrogen does not strictly improve the bulk properties of hydrogen in the gas phase. Including the quadrupole moment may improve the prediction of phase coexistence in the liquid phase, as observed by Sun et al.[34] Therefore, the Marx force field is considered further for VLE simulations of $H_2O - H_2$ mixtures.

The densities and chemical potentials of TIP3P,[96] SPC,[98] SPC/E,[99] TIP4P/2005,[83] TIP4P/Ew,[108] OPC[67] and TIP5P/Ew[101] force fields between $P = 100$ bar and $P = 1000$ bar obtained from CFCNPT simulations are compared to the IAPWS empirical EoS,[69,81] see Fig. 2. Raw data are provided in table S4 in the Supporting Information. It is shown

in Fig. 2(a) that the force fields TIP5P/Ew and TIP4P/2005 clearly outperform the TIP3P and SPC force fields in predicting the density of liquid water (on average around 2%) over the whole pressure range. The TIP4P/2005 water is parameterized based on temperature of maximum density of liquid water, the stability of several ice polymorphs etc.[83] The TIP5P/Ew model is obtained from reparametrization of the TIP5P model[109] which is also a very accurate model capable of predicting maximum density of liquid water around 4° C.[101] Note that the deviations of the densities obtained from the TIP3P and SPC models decrease with increasing pressure. As shown in Fig. 2, the chemical potential of water is best predicted using the TIP3P and SPC force fields over the whole temperature range. This observation is also in agreement with previous works.[49,56] The performance of the TIP3P and the SPC force fields are very similar in calculating the densities and chemical potentials of water. The TIP3P force field has been parameterized to the vaporization energy and density of liquid water.[96] This is consistent with the fact that the computed chemical potential of TIP3P water is in better agreement with IAPWS empirical EoS, compared to TIP4P/2005 or TIP5P/Ew models. Raw data for Fig. 2 are provided in table S4 of the Supporting Information. As shown in Fig. 2, the average deviation of the chemical potential of TIP3P force field from the IAPWS empirical EoS[69,81] is about +50 K (in units of energy/k_{B}) for the whole pressure range. The average deviations of the chemical potentials for the TIP4P/2005 and TIP5P/Ew force fields from IAPWS empirical EoS are ca. −500 K and +250 K, respectively. The performance of the SPC/E force field is very similar to the TIP4P/2005 force field for predicting the densities and chemical potentials of water. For the 4-site water force fields, the densities and chemical potentials of the TIP4P/2005 force field show the best agreement with the experiments. Due to overall difference between the predicted densities and chemical potentials of these water models, it is not a priori clear which water model is best fitted for predicting the VLE of $H_2O − H_2$ mixtures. Therefore, three water models are considered (TIP3P,TIP4P/2005,TIP5P/Ew) in combination with the Marx force field (for hydrogen) for phase coexistence calculations of $H_2O − H_2$ mixtures, using molecular simulations.

The water content in the gas phase and the solubility of hydrogen in the liquid phase for the mixture defined by the TIP3P-Marx force fields are obtained from phase coexistence equilibrium calculations, see Fig. 3. To check the consistency between the results with both methods, phase coexistence calculations at $T = 323$ K and $P > 100$ bar are performed for both (*i.e.* CFCGE and CFCNPT). It is shown that both methods yield the same results within the error bars. At $T = 283$ K, all simulations are performed only in the CFCNPT ensemble for the whole pressure range. At $T = 310$ K and $P > 100$ bar, phase coexistence calculations are also performed using simulations in the CFCNPT ensemble. At $T = 366$ K and $T = 423$ K, phase coexistence calculations are performed using simulations in the CFCGE. Raw data from experimental results are provided in tables S5 and S6 of the Supporting Information, and the simulations results are provided in table S7 in the Supporting Information. Based on available experimental data at pressures above $P = 300$ bar,[21] it is clear that the predicted solubility of TIP3P water in the gas phase is in good agreement with experimental data. At $T = 283$ K, no experimental solubilities have been found, and therefore only the results obtained from molecular simulations are shown. For all isotherms of water vapor in the gas phase, it can be observed that the water content is slightly overpredicted at low pressures. At high pressures, the solubility of water in the gas phase is marginally underpredicted. From the condition of chemical equilibrium, we know that the chemical potential of water in the gas phase is equal to the chemical potential of water in the liquid phase. Therefore, it seems that good performance of the TIP3P force field to predict the isotherms of water in the gas phase is most likely related to how accurate it can predict μ_{H_2O} in the liquid phase. Based on the results shown in Figs. 2 and 3 it can be concluded that parametrization of the TIP3P force field based on the evaporation energy as one of the target quantities is essential for predicting the VLE of $H_2O - H_2$ mixtures. For all temperatures in this study (between $T = 283$ K and $T = 423$ K), it is observed that the solubility of water in the gas phase at coexistence is significantly higher than 5 μmol water per mol hydrogen (as allowed by the ISO standard[20]). Therefore, an additional step for removing water is needed.

The calculated isotherms for hydrogen in the liquid phase (TIP3P-Marx) are clearly overpredicted compared to experimental data as shown in Fig. 3(b). To the best of our knowledge, experimental solubility data for hydrogen isotherms in the liquid phase at pressures above ca. $P = 140$ bar are not available in the literature, except at $T = 323$ K.[21] The deviation from experimental solubilities of hydrogen at $T = 323$ K ranges from about 36% to 18% between $P = 50$ bar and $P = 1000$ bar, respectively. At $T = 366$ K, the deviation from experimental data is about 50% between $P = 50$ bar and $P = 100$ bar. At $T = 423$ K the deviation from experimental data is about 110% between $P = 50$ bar and $P = 80$ bar. Therefore, it can be concluded that the deviation of simulation results from experimental data increases with increasing temperature. Based on these results, it can also be concluded that the deviation from experimental solubilities decreases with increasing pressure. Similarly, better agreement is observed between experimental densities of water and those obtained based on TIP3P water at high pressures as also shown in Fig. 2. This suggests that predicting the density of the liquid phase (almost pure water) accurately may result in predicting the mixture compositions in better agreement with experiments.

The solubilities obtained from phase coexistence at equilibrium for the $H_2O - H_2$ mixture defined by the TIP4P/2005-Marx force fields are shown in Fig. 4. Raw data are provided in table S8 of the Supporting Information. For this mixture, all simulations are performed in the CFCGE, at $T = 323$ K, $T = 366$ K and $T = 423$ K. It is clear from Fig. 4 that the solubilities of water in the gas phase are significantly underestimated for the whole pressure range. This is mainly due to the fact that the chemical potential of TIP4P/2005 water is significantly underpredicted, as shown in Fig. 2. Since the predicted water solubilities in the gas phase are systematically lower for the TIP4P/2005-Marx mixture (see Figs. 3a and 4a), the statistics for water solubilities obtained from CFCGE simulations are worse. This sampling issue is explained in Section 2.1. Similarly, the computed isotherms of hydrogen in the liquid phase are slightly underpredicted. For the mixture defined by TIP4P2005-Marx force fields, better agreement with experiments is observed for solubilities in the liquid phase for all temperatures.

At $T = 366$ K, the deviation from experimental data is about 14% between $P = 50$ bar and $P = 100$ bar. At $T = 423$ K the deviation from experimental data is about 5% between $P = 50$ bar and $P = 80$ bar.

The solubilities obtained from phase coexistence at equilibrium for $H_2O - H_2$ mixture defined by TIP5P/Ew-Marx force fields are shown in Fig. 5. Raw data are provided in table S9 of the Supporting Information. For this mixture, all simulations are performed in the CFCGE, at $T = 323$ K, $T = 366$ K and $T = 423$ K. In sharp contrast to the TIP4P/2005-Marx mixture, both calculated solubilities in the liquid and gas using the TIP5P/Ew-Marx mixture are overpredicted. The solubilities of hydrogen in the liquid phase are very similar to those obtained form the TIP3P-Marx force fields. To explain the results in a coherent way, it is important to consider the predicted water isotherms in the gas phase in Figs. 3 to 5 and the calculated chemical potentials of pure water in Fig. 2(b) simultaneously. From these figures, it can be concluded that underpredicting the solubilties in the gas phase is directly related to underpredcting the chemical potential of water (TIP4P/2005). Similarly, overpredicting the solubilties of water in the gas phase is directly related to overpredcting the chemical potential of water (TIP5P/Ew).

3.2 Equation of State Modelling

The water content in the gas phase and the solubility of hydrogen in the liquid phase are also calculated using the PR-EoS and SRK-EoS. High pressure experimental solubilites at $T = 323$ K were used to obtain the Binary Interaction Parameters (k_{ij}'s) for the PR-EoS and SRK-EoS. For $T = 323$ K, the isotherms of water and hydrogen in the gas and liquid phase are shown in Fig. 6 using both zero k_{ij}'s and non-zero k_{ij}'s. In Fig. 6, it is shown that the predicted solubilities in the liquid phase are significantly lower compared to experiments, using zero k_{ij}'s. The solubility of (nonpolar) gases is dominated by entropic effects which are related to the molar volume.[110] It is well-known that the predicted volumes of the liquid phase from PR-EoS or SRK-EoS, using conventional mixing rules, have significant errors.[24,25,106]

Since 2017, more than 220 modifications of mixing rules for pure components and extensions to mixtures with the PR-EoS have been reported in literature.[24] This clearly indicates the need for more physically based models for thermodynamic modelling. In addition, the $H_2O - H_2$ system is highly polar in the liquid phase, and the performance of the conventional mixing rules for PR-EoS and SRK-EoS for polar mixture are known to be poor.[24] Therefore, it is expected that PR-EoS or SRK-EoS are not able to predict solubilities of hydrogen in liquid water accurately. With the fitted k_{ij}'s, the obtained solubilities of hydrogen in the liquid phase are in excellent agreement with experimental data for $p < 400$ bar. However, the solubilities in the gas phase deviate significantly using the fitted k_{ij}'s. Therefore, calculations of VLE of $H_2O - H_2$ mixtures using PR-EoS and SRK-EoS do not yield satisfactory results for both phases simultaneously, with or without adjusted k_{ij}'s.

4 Conclusions

Molecular simulations are used to model the VLE behavior of $H_2O - H_2$ mixtures for pressures between $P = 10$ bar and $P = 1000$ bar. In tables S5 and S6, a detailed overview of available experimental data has been provided for this system. It is shown that commonly used cubic EoS, with conventional mixing rules fail to predict the composition of the gas and the liquid phases accurately. For the different molecular models for hydrogen, the Buch force field[71] (single-site model) and the Marx force field (including quadrupole moment) predict the density and fugacity coefficient of hydrogen in good agreement with experiments up to $P = 1000$ bar. In this study, no force field for rigid water with fixed point charges could accurately predict both the chemical potential and the density of water. The computed chemical potentials of TIP3P water[96] have the best agreement with experimental data from REFPROP[69] with a deviation of about $+50$ K (μ/k_B) for pressures between $P = 100$ bar and $P = 1000$ bar. This may be partly due to the fact that one of the target fitting parameters for the TIP3P force field is the heat of vaporization, unlike the TIP4P/2005 and TIP5P/Ew

force fields. The computed chemical potentials (μ/k_{B}) of the TIP4P/2005 and TIP5P/Ew deviate on average by -500 K and $+250$ K from experimental data in this pressure range, respectively. Both the TIP4P/2005 and TIP5P/Ew force fields can predict the density of liquid water in good agreement with the experiments for the whole pressure range. From the simulations result, it is observed that solubilities of water in the gas phase are systematically underpredicted when using the TIP4P/2005 force field. This force field also underpredicts the chemical potential of liquid water compared to experiments. The highest solubilities in the gas phase are predicted using the TIP5P/Ew force field with the largest values for the calculated chemical potential of water. The best agreement between the predicted gas phase compositions and experiments for the whole pressure range are observed for the TIP3P fore field. This suggests that a suitable water force field for studying the VLE of $H_2O - H_2$ mixtures can be screened based on the chemical potential of the water model in the liquid phase. Based on the screening of seven water force fields in this study, it turns out that the TIP3P and SPC force fields (with very similar values for chemical potential of liquid water) can best predict the equilibrium vapor phase coexistence composition of the $H_2O - H_2$ system. For all temperatures in this study, we observed that the solubility of water in the gas phase at coexistence is significantly higher than 5 μmol water per mol hydrogen (as allowed by the ISO standard). Therefore, an additional step for removing extra water from the gas phase is required. Despite the fact that the molecular simulations significantly outperform cubic EoS modelling for the VLE of $H_2O - H_2$ mixtures, the predicted liquid phase compositions need further improvements. The solubilities of hydrogen in the liquid phase are overpredicted using the TIP3P-Marx and TIP5P/Ew-Marx force fields. The best agreement between the calculated liquid phase composition and experiments is observed for the TIP4P/2005-Marx system (although the predicted solubilities are slightly lower). Further improvements in simulations of $H_2O - H_2$ systems may be realized taking polarizability of water molecules into account. Therefore, further molecular simulations of the $H_2O - H_2$ are recommended using polarizable force fields for water, especially to improve the predictions

for the liquid phase composition.

Acknowledgement

Supporting Information Available

Derivation of Eq. 2; force field parameters for water and hydrogen, calculated densities and fugacity coefficients for pure hydrogen in the gas phase (different force fields); calculated densities and chemical potentials for pure liquid water (different force fields); experimental solubilities of hydrogen in the $H_2O - H_2$ mixture (liquid phase) at coexistence; experimental solubilities of water vapor in the $H_2O - H_2$ mixture (gas phase) at coexistence; raw data for the computed coexistence compositions of $H_2O - H_2$ mixtures at equilibrium using MC simulations; equation of state parameters for the PR-EoS and SRK-EoS
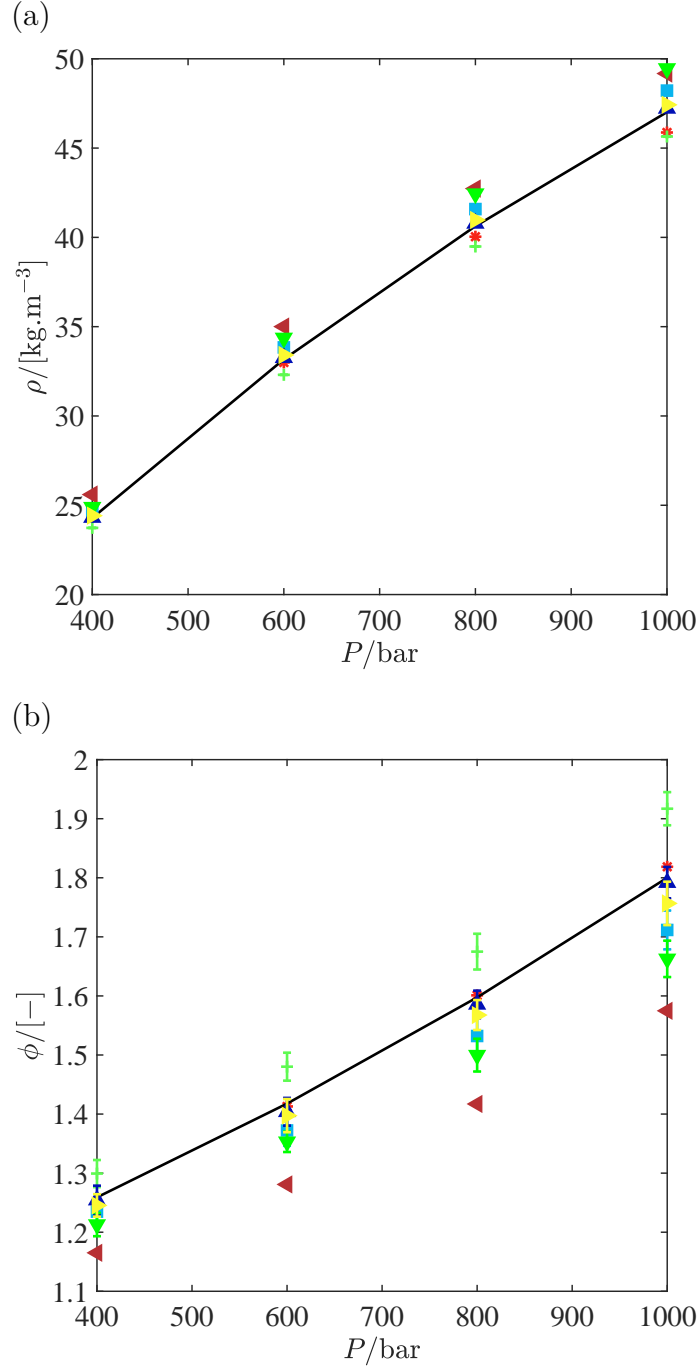
Figure 1: Comparison of different models to predict (a): the density and (b): the fugacity coefficient of pure hydrogen in the gas phase at $T = 323$ K and pressures ranging between $P = 10$ and $P = 1000$ bar. PR-EoS (left-pointing triangle), SRK-EoS (asterisk), experimental data from REFPROP[69,70] (lines), molecular force fileds: Hirschfelder[72] (squares), Vrabec[73] (Plus signs), Buch[71] (upward-pointing triangles), Cracknell[74] (downward-pointing triangles) and Marx[77] (right-pointing triangles). Parameters for the EoS are provided in table S10 of the Supporting Information. Raw simulation data are provided in table S3 of the Supporting Information.
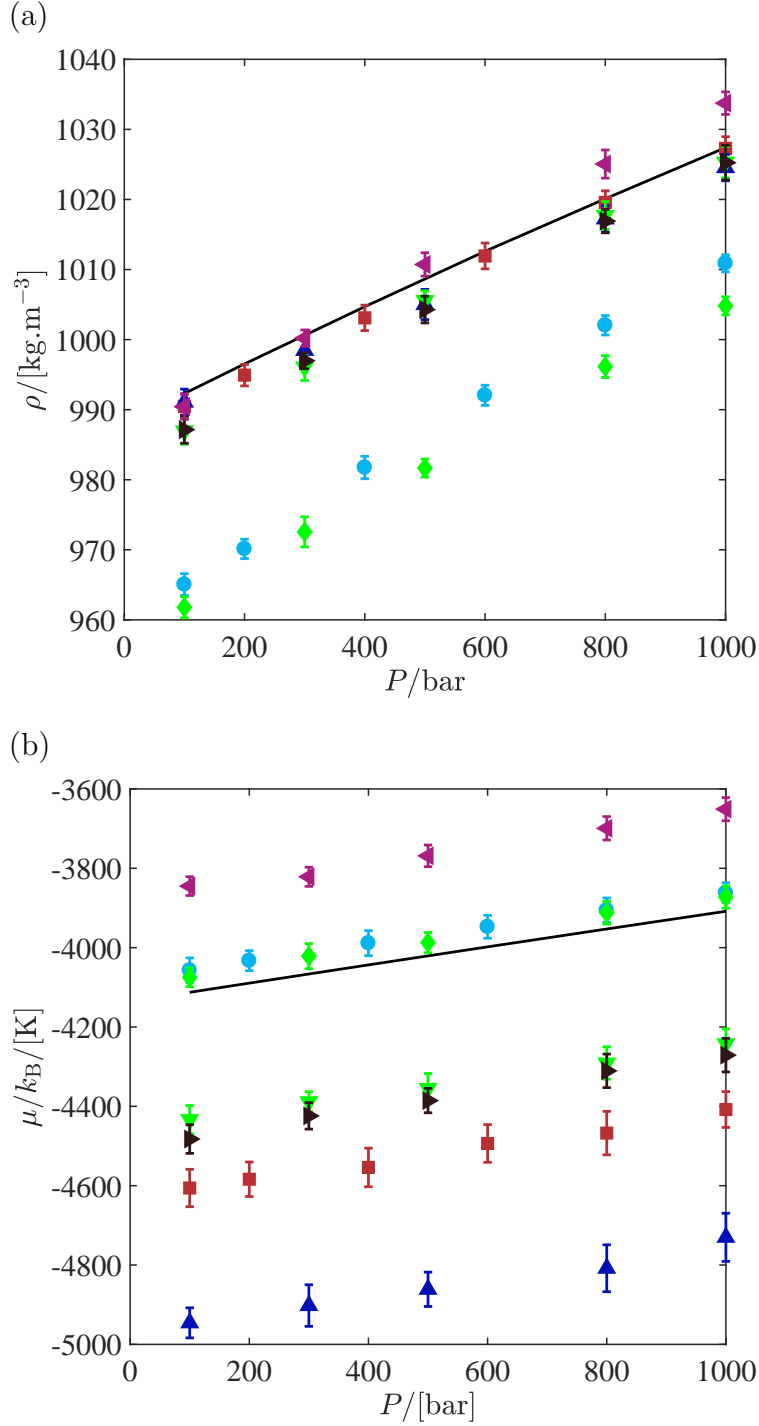
Figure 2: Comparison of different force fields of water to predict (a): the density and (b): the chemical potential in the liquid phase at $T = 323$ K and pressures ranging between $P = 10$ and $P = 1000$ bar: TIP3P[96] (diamonds), SPC[98] (circles), SPC/E[99] (right-pointing triangles), TIP4P/2005[83] (squares), TIP4P/Ew[108] (downward-pointing triangles), OPC[67] (upward-pointing triangles), TIP5P/Ew[101] (left-pointing triangles). In both subfigures, the lines are obtained from REFPROP.[69,70] Raw data are provided in table S4 of the Supporting Information.
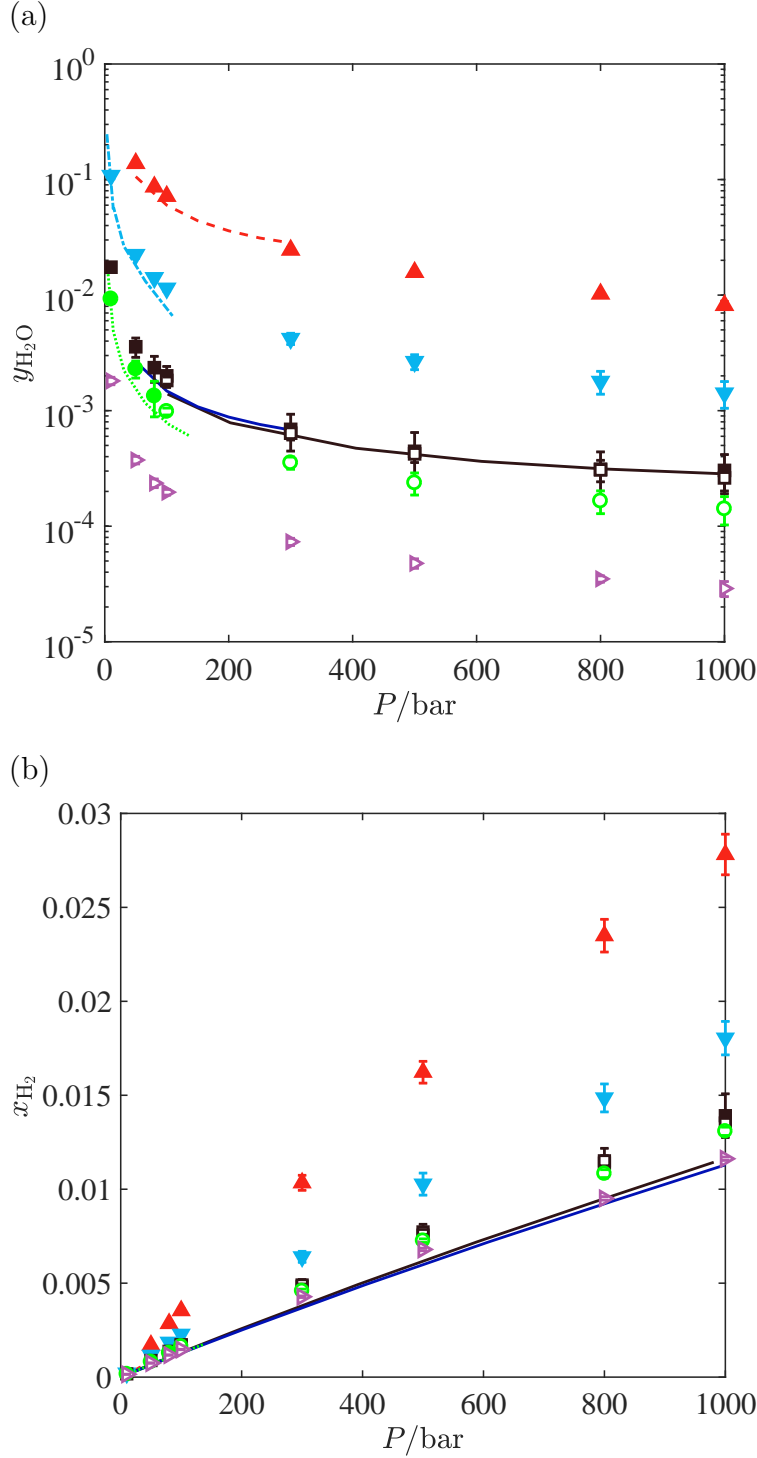
Figure 3: Vapor-Liquid equilibrium of $H_2O - H_2$ (TIP3P[96]-Marx[77]) at pressures ranging between $P = 10$ and $P = 1000$ bar. (a): y_{H_2O} in the gas phase and (b): x_{H_2} in the liquid phase. $T = 423$ K (upward-pointing triangles), $T = 366$ K (downward-pointing triangles), $T = 323$ K (squares), $T = 310$ K (circles), $T = 283$ (right-pointing triangles). Experimental data for $T = [423, 366, 323, 310]$ K are shown with dashed lines, dash-dot lines, solid lines and dotted lines, respectively. Published high pressure data are only available for $T = 323$ K.[21] Raw data are provided in tables S5, S6 and S7 of the Supporting Information.
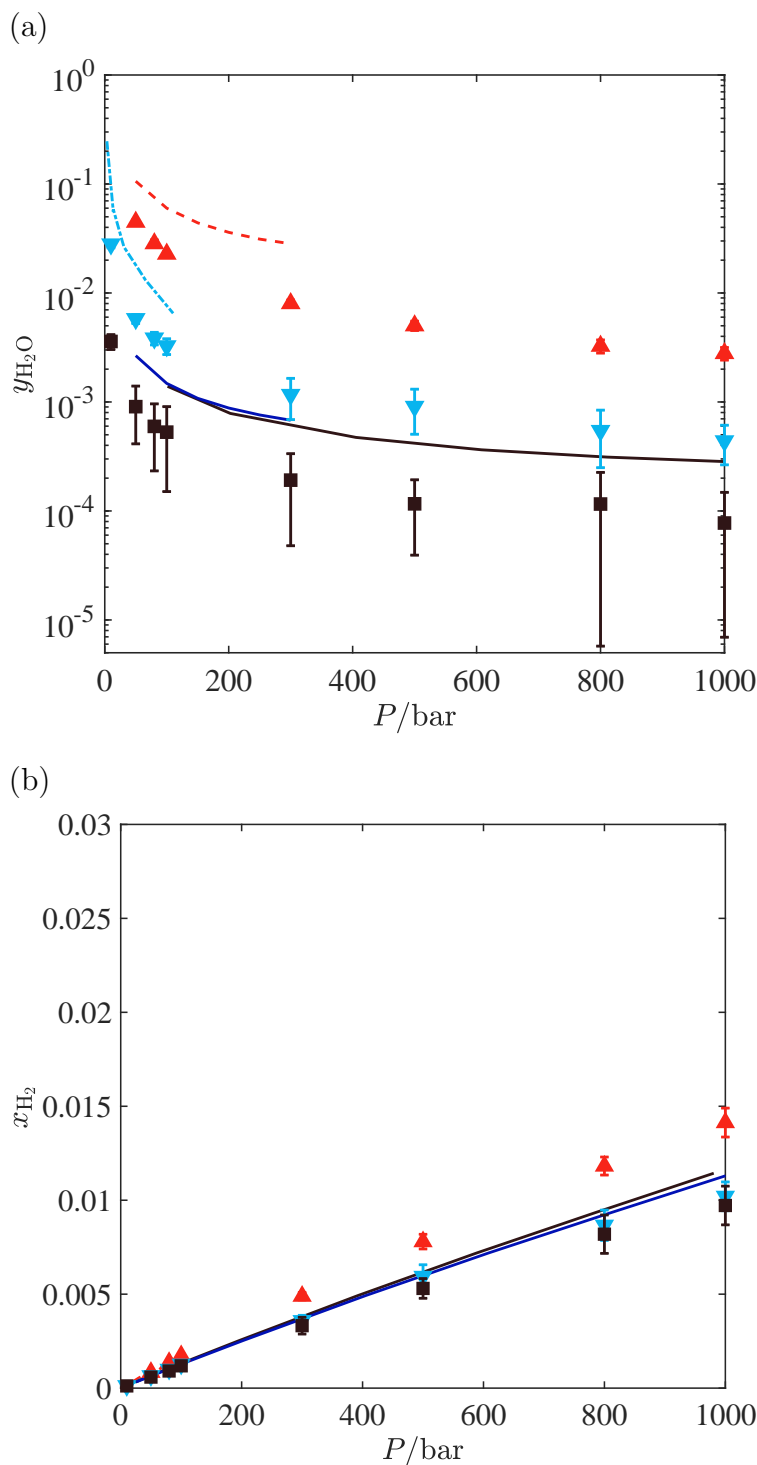
Figure 4: Vapor-Liquid equilibrium of $H_2O - H_2$ (TIP4P/2005[83]-Marx[77]) at pressures ranging between $P = 10$ and $P = 1000$ bar. (a): y_{H_2O} in the gas phase and (b): x_{H_2} in the liquid phase. $T = 423$ K (upward-pointing triangles), $T = 366$ K (downward-pointing triangles), $T = 323$ K (squares). Experiential data for $T = [423, 366, 323, 310]$ K are shown with dashed lines, dash-dot lines, solid lines and dotted lines, respectively. Published high pressure data are only available for $T = 323$ K.[21] Raw data are provided in tables S5, S6 and S8 of the Supporting Information..

24

(a)

(b)
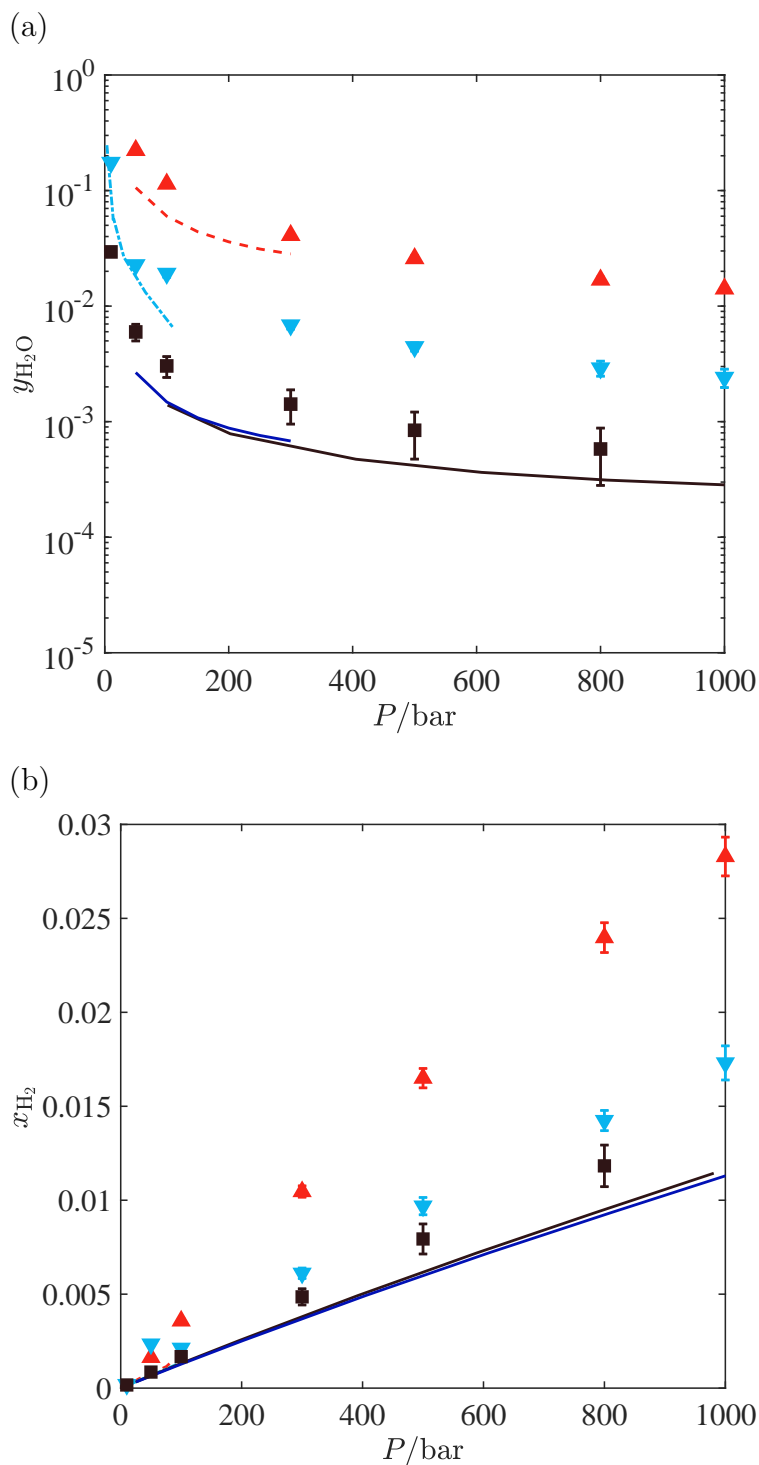
Figure 5: Vapor-Liquid equilibrium of $H_2O - H_2$ (TIP5P/Ew[101]-Marx[77]) at pressures ranging between $P = 10$ and $P = 1000$ bar. (a): y_{H_2O} in the gas phase and (b): x_{H_2} in the liquid phase. $T = 423$ K (upward-pointing triangles), $T = 366$ K (downward-pointing triangles), $T = 323$ K (squares). Experiential data for $T = [423, 366, 323, 310]$ K are shown with dashed lines, dash-dot lines, solid lines and dotted lines, respectively. Published high pressure data are only available for $T = 323$ K.[21] Raw data are provided in table S5, S6, S9 of the Supporting Information.

25

(a)

(b)
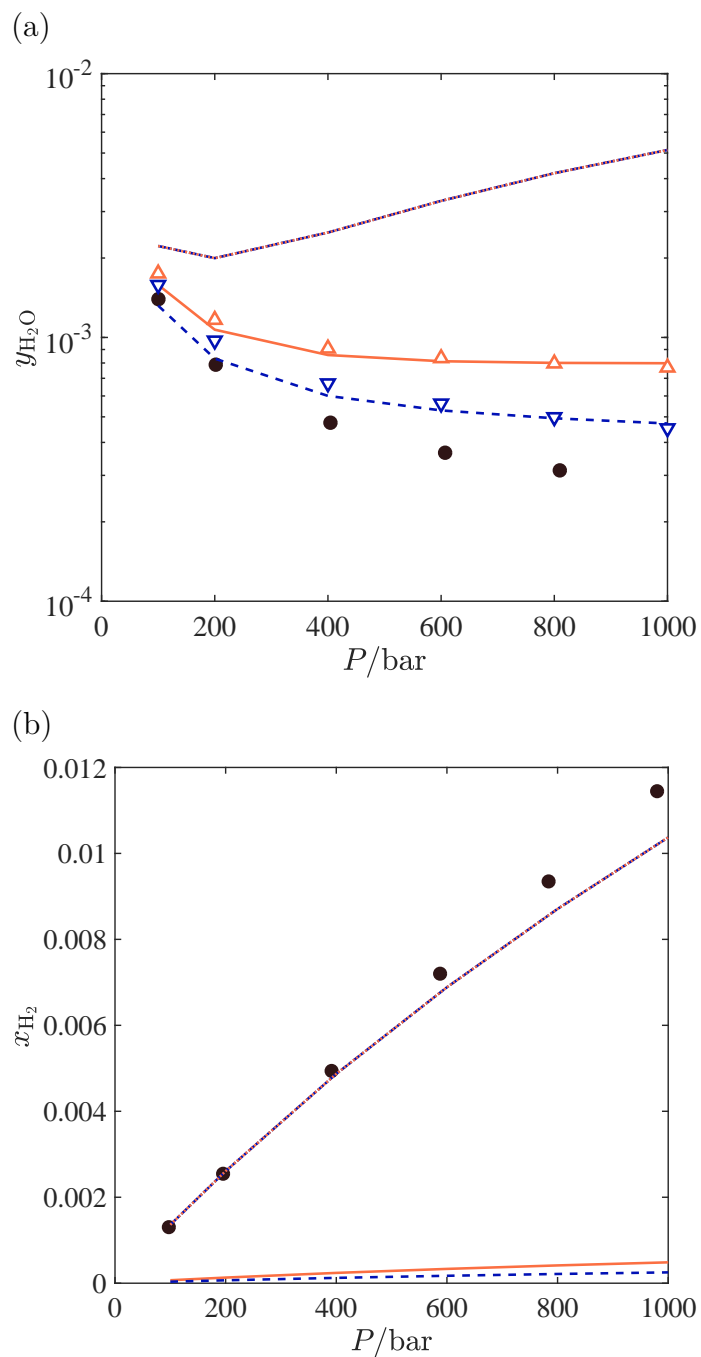
Figure 6: VLE of $H_2O - H_2$ at $T = 323$ K and pressures ranging between $P = 100$ and $P = 1000$ bar, obtained from EoS modelling. (a): mole fraction of water in the gas phase, (b): mole fraction of hydrogen in the liquid phase. Experimental solubilities are shown with circles. In both subfigures, the results are shown for $k_{ij} = 0$: PR-EoS[102] (lines), SRK-EoS[103] (dashed lines). The results from the γ-ϕ method are shown with open symbols: PR-EoS (upward-pointing triangles) and the SRK-EoS (downward-pointing triangles). The results for the fitted BIP for the PR-EoS ($k_{ij} = -0.89$) are shown with dash-dot lines. The results for the fitted BIP for the SRK-EoS ($k_{ij} = -1.51$) are shown with dotted lines.

26

References

(1) *World Population Prospects: The 2017 Revision, Key Findings and Advance Tables, ESA/P/WP/248.*; 2017; `https://population.un.org/wpp/Publications/Files/WPP2017_KeyFindings.pdf`.

(2) *United Nations. (2015) General Assembly Resolution A/RES/70/1. Transforming our world: the 2030 Agenda for Sustainable Development*; 2015; `http://www.un.org/ga/search/view_doc.asp?symbol=A/RES/70/1&Lang=E`.

(3) *World Energy Outlook 2018*; 2018; `www.iea.org/weo`.

(4) *Adoption of the Paris Agreement,* FCCC/CP/2015/L.9/Rev.1; 2015; `https://unfccc.int/resource/docs/2015/cop21/eng/l09r01.pdf`.

(5) Gallo, A.; Simões-Moreira, J.; Costa, H.; Santos, M.; Moutinho dos Santos, E. Energy storage in the energy transition context: A technology review. *Renew. Sust. Energy Rev.* **2016**, *65*, 800–822.

(6) Zakeri, B.; Syri, S. Electrical energy storage systems: A comparative life cycle cost analysis. *Renew. Sust. Energy Rev.* **2015**, *42*, 569 – 596.

(7) Evans, A.; Strezov, V.; Evans, T. J. Assessment of utility energy storage options for increased renewable energy penetration. *Renew. Sust. Energy Rev.* **2012**, *16*, 4141 – 4147.

(8) Mahlia, T.; Saktisahdan, T.; Jannifar, A.; Hasan, M.; Matseelar, H. A review of available methods and development on energy storage; technology update. *Renew. Sust. Energy Rev.* **2014**, *33*, 532 – 545.

(9) Chen, H.; Cong, T. N.; Yang, W.; Tan, C.; Li, Y.; Ding, Y. Progress in electrical energy storage system: A critical review. *Progress in Natural Science* **2009**, *19*, 291 – 312.

(10) Johnston, B.; Mayo, M. C.; Khare, A. Hydrogen: the energy source for the 21st century. *Technovation* **2005**, *25*, 569 – 585.

(11) Rahbari, A.; Ramdin, M.; van den Broeke, L. J. P.; Vlugt, T. J. H. Combined steam reforming of methane and formic acid To produce syngas with an adjustable H_2:CO ratio. *Ind. Eng. Chem. Res.* **2018**, *57*, 10663–10674.

(12) Adolf, J.; Balzer, C.; Louis, J. *Energy of the Future? Sustainable Mobility through Fuel Cells and H_2*; 2017.

(13) Bouwman, P. Electrochemical Hydrogen Compression (EHC) solutions for hydrogen infrastructure. *Fuel Cells Bulletin* **2014**, *2014*, 12–16.

(14) Bampaou, M.; Panopoulos, K. D.; Papadopoulos, A. I.; Seferlis, P.; Voutetakis, S. An electrochemical hydrogen compression model. *Chem. Eng. Trans.* **2018**, *70*.

(15) Ströbel, R.; Oszcipok, M.; Fasil, M.; Rohland, B.; Jörissen, L.; Garche, J. The compression of hydrogen in an electrochemical cell based on a PE fuel cell design. *J. Power Sources* **2002**, *105*, 208 – 215, 7th Ulmer Elektrochemische Tage.

(16) Suermann, M.; Kiupel, T.; Schmidt, T. J.; Büchi, F. N. Electrochemical hydrogen compression: efficient pressurization concept derived from an energetic evaluation. *J. Electrochem. Soc.* **2017**, *164*, F1187–F1195.

(17) Rohland, B.; Eberle, K.; Ströbel, R.; Scholta, J.; Garche, J. Electrochemical hydrogen compressor. *Electrochim. Acta.* **1998**, *43*, 3841 – 3846.

(18) Nordio, M.; Rizzi, F.; Manzolini, G.; Mulder, M.; Raymakers, L.; Van Sint Annaland, M.; Gallucci, F. Experimental and modelling study of an electrochemical hydrogen compressor. *Chem. Eng. J.* **2019**, *369*, 432–442.

(19) Casati, C.; Longhi, P.; Zanderighi, L.; Bianchi, F. Some fundamental aspects in

electrochemical hydrogen purification/compression. *J. Power Sources* **2008**, *180*, 103–113.

(20) *Hydrogen fuel - Product specification - Part 2: Proton exchange membrane (PEM) fuel cell applications for road vehicles*; International Standard, 2012; Vol. 2012; `www.iso.org/committee/54560/x/catalogue/`.

(21) Bartlett, E. P. The concentration of water vapor in compressed hydrogen, Nitrogen and a mixture of these gases in the presence of condensed water. *Journal of the American Chemical Society* **1927**, *49*, 65–78.

(22) Wiebe, R.; Gaddy, V. L. The solubility of hydrogen in water at 0, 50, 75 and 100° from 25 to 1000 atmospheres. **2005**, *56*, 76–79.

(23) Hendriks, E.; Kontogeorgis, G. M.; Dohrn, R.; de Hemptinne, J.-C.; Economou, I. G.; Žilnik, L. F.; Vesovic, V. Industrial requirements for thermodynamics and transport properties. *Ind. Eng. Chem. Res.* **2010**, *49*, 11131–11141.

(24) Lopez-Echeverry, J. S.; Reif-Acherman, S.; Araujo-Lopez, E. Peng-Robinson equation of state: 40 years through cubics. *Fluid Phase Equilib.* **2017**, *447*, 39 – 71.

(25) Iwai, Y.; Margerum, M. R.; Lu, B. C.-Y. A new three-parameter cubic equation of state for polar fluids and fluid mixtures. *Fluid Phase Equilib.* **1988**, *42*, 21 – 41.

(26) Diamantonis, N. I.; Boulougouris, G. C.; Mansoor, E.; Tsangaris, D. M.; Economou, I. G. Evaluation of cubic, SAFT, and PC-SAFT equations of state for the vapor-liquid equilibrium modeling of CO_2 mixtures with other gases. *Ind. Eng. Chem. Res.* **2013**, *52*, 3933–3942.

(27) Kwak, T.; Mansoori, G. A. Van der Waals mixing rules for cubic equations of state. Applications for supercritical fluid extraction modelling. *Chem. Eng. Sci.* **1986**, *41*, 1303–1309.

(28) Harstad, K. G.; Miller, R. S.; Bellan, J. Efficient high-pressure state equations. *AIChE J.* **1997**, *43*, 1605–1610.

(29) Jhaveri, B. S.; Youngren, G. K. Three-parameter modification of the Peng-Robinson equation of state to improve volumetric predictions. *SPE reservoir engineering* **1988**, *3*, 1033–1040.

(30) Poling, B. E.; Prausnitz, J. M.; O'Connell, J. P. *The properties of gases and liquids*, 5th ed.; McGraw-Hill New York: New York, USA, 2001.

(31) Valderrama, J. O. The State of the Cubic Equations of State. *Ind. Eng. Chem. Res.* **2003**, *42*, 1603–1618.

(32) Gross, J.; Sadowski, G. Perturbed-Chain SAFT: An equation of state based on a perturbation theory for chain molecules. *Ind. Eng. Chem. Res.* **2001**, *40*, 1244–1260.

(33) Frenkel, D.; Smit, B. *Understanding molecular simulation: from algorithms to applications*, 2nd ed.; Academic Press: San Diego, California, 2002.

(34) Sun, R.; Lai, S.; Dubessy, J. Calculations of vapor-liquid equilibria of the H_2O-N_2 and H_2O-H_2 systems with improved SAFT-LJ EOS. *Fluid Phase Equilib.* **2015**, *390*, 23 – 33.

(35) Meyer, M.; Tebbe, U.; Piiper, J. Solubility of inert gases in dog blood and skeletal muscle. *Pflügers Archiv European Journal of Physiology* **1980**, *384*, 131–134.

(36) Gillespie, P. C.; Wilson, G. M. *Vapor-Liquid Equilibrium Data on Water-Substitue Gas Components*; 1980; pp RR_41, 1–34.

(37) Kling, G.; Maurer, G. The solubility of hydrogen in water and in 2-aminoethanol at temperatures between 323 K and 423 K and pressures up to 16 M Pa. *Chem. Thermodynamics* **1991**, *23*, 531–541.

(38) Devaney, W.; Berryman, J. M.; Kao, P.-L.; Eakin, B. *High Temperature V-L-E Measurements for Substitute Gas Components*; 1978; pp 1–27.

(39) Jung, J. Loslichkeit von Kohlenmonoxid und Wasserstoff in Wasser zwisen 0 C und 300 C. Ph.D. thesis, RWTH Aachen, 1962.

(40) Ipatev, V.; Teodorovich, V. Equilibrium compositions of vapor-gas mixtures over solutions. *Zh.Obshch.Khim.* **1934**, *4*, 395–399.

(41) Ugrozov, V. V. Equilibrium compositions of vapor-gas mixtures over solutions. **1996**, *70*, 1240–1241.

(42) Maslennikova, V. Y.; Goryunova, N.; Subbotina, L.; Tsiklis, D. The solubility of water in compressed hydrogen. *Russian Journal of Physical Chemistry* **1976**, *50*, 240–243.

(43) Panagiotopoulos, A. Z. Molecular simulation of phase equilibria: simple, ionic and polymeric fluids. *Fluid Phase Equilib.* **1992**, *76*, 97–112.

(44) Panagiotopoulos, A. Z. Direct determination of fluid-Phase equilibria by simulation in the Gibbs ensemble - a Review. *Mol. Simul.* **1992**, *9*, 1–23.

(45) Panagiotopoulos, A. Z. Direct determination of phase coexistence properties of fluids by Monte Carlo simulation in a new ensemble. *Mol. Phys.* **1987**, *61*, 813–826.

(46) Recht, J.; Panagiotopoulos, A. Z. Finite-size effects and approach to criticality in Gibbs ensemble simulations. *Mol. Phys.* **1993**, *80*, 843–852.

(47) Siepmann, J. I.; McDonald, I. R.; Frenkel, D. Finite-size corrections to the chemical potential. *J. Phys.: Condens. Matt.* **1992**, *4*, 679.

(48) Smit, B.; Frenkel, D. Calculation of the chemical potential in the Gibbs ensemble. *Mol. Phys.* **1989**, *68*, 951–958.

(49) Rahbari, A.; Poursaeidesfahani, A.; Torres-Knoop, A.; Dubbeldam, D.; Vlugt, T. J. H. Chemical potentials of water, methanol, carbon dioxide and hydrogen sulphide at low temperatures using continuous fractional component Gibbs ensemble Monte Carlo. *Mol. Simul.* **2018**, *44*, 405–414.

(50) Coskuner, O.; Deiters, U. K. Hydrophobic interactions by Monte Carlo simulations. *Zeitschrift für Phys. Chem.* **2006**, *220*, 349–369.

(51) Shi, W.; Maginn, E. J. Continuous Fractional Component Monte Carlo: an adaptive biasing method for open system atomistic simulations. *J. Chem. Theory Comput.* **2007**, *3*, 1451–1463.

(52) Shi, W.; Maginn, E. J. Improvement in molecule exchange efficiency in Gibbs ensemble Monte Carlo: development and implementation of the continuous fractional component move. *J. Comput. Chem.* **2008**, *29*, 2520–2530.

(53) Poursaeidesfahani, A.; Torres-Knoop, A.; Dubbeldam, D.; Vlugt, T. J. H. Direct free energy calculation in the Continuous Fractional Component Gibbs ensemble. *J. Chem. Theory Comput.* **2016**, *12*, 1481–1490.

(54) Poursaeidesfahani, A.; Hens, R.; Rahbari, A.; Ramdin, M.; Dubbeldam, D.; Vlugt, T. J. H. Efficient application of Continuous Fractional Component Monte Carlo in the reaction ensemble. *J. Chem. Theory Comput.* **2017**, *13*, 4452–4466.

(55) Rahbari, A.; Hens, R.; Nikolaidis, I. K.; Poursaeidesfahani, A.; Ramdin, M.; Economou, I. G.; Moultos, O. A.; Dubbeldam, D.; Vlugt, T. J. H. Computation of partial molar properties using continuous fractional component Monte Carlo. *Mol. Phys.* **2018**, *116*, 3331–3344.

(56) Rahbari, A.; Hens, R.; Jamali, S. H.; Ramdin, M.; Dubbeldam, D.; Vlugt, T. J. H. Effect of truncating electrostatic interactions on predicting thermodynamic properties of water-methanol systems. *Mol. Simul.* **2019**, *45*, 336–350.

(57) Dubbeldam, D.; Calero, S.; Ellis, D. E.; Snurr, R. Q. RASPA: molecular simulation software for adsorption and diffusion in flexible nanoporous materials. *Mol. Simul.* **2015**, *42*, 81–101.

(58) Dubbeldam, D.; Torres-Knoop, A.; Walton, K. S. On the inner workings of Monte Carlo codes. *Mol. Simul.* **2013**, *39*, 1253–1292.

(59) Allen, M. P.; Tildesley, D. J. *Computer simulation of liquids*, 2nd ed.; Oxford university press: Oxford, United Kingdom, 2017.

(60) Klimovich, P. V.; Shirts, M. R.; Mobley, D. L. Guidelines for the analysis of free energy calculations. *J Comput. Aided. Mol. Des.* **2015**, *29*, 397–411.

(61) Naden, L. N.; Pham, T. T.; Shirts, M. R. Linear basis function approach to efficient alchemical free energy calculations. 1. Removal of uncharged atomic sites. *J. Chem. Theory Comput.* **2014**, *10*, 1128–1149.

(62) Naden, L. N.; Shirts, M. R. Linear basis function approach to efficient alchemical free energy calculations. 2. Inserting and deleting particles with Coulombic interactions. *J. Chem. Theory Comput.* **2015**, *11*, 2536–2549.

(63) Shirts, M. R.; Pande, V. S. Solvation free energies of amino acid side chain analogs for common molecular mechanics water models. *J. Chem. Phys.* **2005**, *122*, 134508.

(64) Shirts, M. R.; Pitera, J. W.; Swope, W. C.; Pande, V. S. Extremely precise free energy calculations of amino acid side chain analogs: Comparison of common molecular mechanics force fields for proteins. *J. Chem. Phys.* **2003**, *119*, 5740–5761.

(65) Shirts, M. R.; Mobley, D. L.; Chodera, J. D. In *Annual Reports in Computational Chemistry*; Spellmeyer, D., Wheeler, R., Eds.; Elsevier: United States, 2007; pp 41–59.

(66) Rahbari, A.; Hens, R.; Dubbeldam, D.; Vlugt, T. J. H. Improving the accuracy of

computing chemical potentials in CFCMC simulations. Mol. phys. in press (uploaded as SI for review only).

(67) Izadi, S.; Anandakrishnan, R.; Onufriev, A. V. Building Water Models: a different approach. *J. Phys. Chem. Lett.* **2014**, *5*, 3863–3871.

(68) Vega, C.; Abascal, J. L. F.; Conde, M. M.; Aragones, J. L. What ice can teach us about water interactions: a critical comparison of the performance of different water models. *Faraday Discuss.* **2009**, *141*, 251–276.

(69) Lemmon, E. W.; Span, R. Short fundamental equations of state for 20 industrial fluids. *J. Chem. Eng. Data* **2006**, *51*, 785–850.

(70) Lemmon, E. W.; Huber, M. L.; McLinden, M. O. NIST reference fluid thermodynamic and transport properties–REFPROP. *NIST standard reference database* **2002**, *23*, v7.

(71) Buch, V. Path integral simulations of mixed para-D_2 and ortho-D_2 clusters: The orientational effects. *J. Chem. Phys.* **1994**, *100*, 7610–7629.

(72) Hirschfelder, C.; Curtiss, F.; Bird, R. B. *Molecular Theory of Gases and Liquids*; Wiley: New York, 1954.

(73) Köster, A.; Thol, M.; Vrabec, J. Molecular Models for the Hydrogen Age: Hydrogen, Nitrogen, Oxygen, Argon, and Water. *J. Chem. Eng. Data* **2018**, *63*, 305–320.

(74) Cracknell, R. F. Molecular simulation of hydrogen adsorption in graphitic nanofibres. *Phys. Chem. Chem. Phys.* **2001**, *3*, 2091–2097.

(75) Belof, J. L.; Stern, A. C.; Space, B. An accurate and transferable intermolecular diatomic hydrogen potential for condensed phase simulation. *J. Chem. Theory Comput.* **2008**, *4*, 1332–1337.

(76) Forrest, K. A.; Pham, T.; McLaughlin, K.; Belof, J. L.; Stern, A. C.; Zaworotko, M. J.; Space, B. Simulation of the mechanism of gas sorption in a metal-organic framework

with open metal sites: molecular hydrogen in PCN-61. *J. Phys. Chem. C* **2012**, *116*, 15538–15549.

(77) Marx, D.; Nielaba, P. Path-integral Monte Carlo techniques for rotational motion in two dimensions: Quenched, annealed, and no-spin quantum-statistical averages. *Phys. Rev. A* **1992**, *45*, 8968–8971.

(78) Camp, J.; Stavila, V.; Allendorf, M. D.; Prendergast, D.; Haranczyk, M. Critical factors in computational characterization of hydrogen storage in metal-organic frameworks. *J. Phys. Chem. C* **2018**, *122*, 18957–18967.

(79) Yang, Q.; Zhong, C. Molecular simulation of carbon dioxide/methane/hydrogen mixture adsorption in metal-organic frameworks. *J. Phys. Chem. B* **2006**, *110*, 17776–17783.

(80) Darkrim, F.; Levesque, D. Monte Carlo simulations of hydrogen adsorption in single-walled carbon nanotubes. *J. Chem. Phys.* **1998**, *109*, 4981–4984.

(81) Wagner, W.; Pruß, A. The IAPWS formulation 1995 for the thermodynamic properties of ordinary water substance for general and scientific use. *J. Phys. Chem. Ref. Data* **2002**, *31*, 387–535.

(82) Vega, C.; Abascal, J. L. F. Simulating water with rigid non-polarizable models: a general perspective. *Phys. Chem. Chem. Phys.* **2011**, *13*, 19663–19688.

(83) Abascal, J. L. F.; Vega, C. A general purpose model for the condensed phases of water: TIP4P/2005. *J. Chem. Phys.* **2005**, *123*, 234505.

(84) Tsimpanogiannis, I. N.; Moultos, O. A.; Franco, L. F. M.; de M. Spera, M. B.; Erdős, M.; Economou, I. G. Self-diffusion coefficient of bulk and confined water: a critical review of classical molecular simulation studies. *Mol. Simul.* **2019**, *45*, 425–453.

(85) Vega, C. Water: one molecule, two surfaces, one mistake. *Mol. Phys.* **2015**, *113*, 1145–1163.

(86) Bauer, B. A.; Patel, S. Properties of water along the liquid-vapor coexistence curve via molecular dynamics simulations using the polarizable TIP4P-QDP-LJ water model. *J. Comput. Phys.* **2009**, *131*, 084709.

(87) Jiang, H.; Moultos, O. A.; Economou, I. G.; Panagiotopoulos, A. Z. Hydrogen-bonding polarizable intermolecular potential model for water. *J. Phys. Chem. B* **2016**, *120*, 12358–12370.

(88) Chen, B.; Xing, J.; Siepmann, J. I. Development of polarizable water force fields for phase equilibrium calculations. *J. Phys. Chem. B* **2000**, *104*, 2391–2401.

(89) Yesylevskyy, S. O.; Schäfer, L. V.; Sengupta, D.; Marrink, S. J. Polarizable Water Model for the Coarse-Grained MARTINI Force Field. *PLoS Comput. Biol.* **2010**, 1–17.

(90) Gladich, I.; Roeselová, M. Comparison of selected polarizable and nonpolarizable water models in molecular dynamics simulations of ice I_{h}. *Phys. Chem. Chem. Phys.* **2012**, *14*, 11371–11385.

(91) Kunz, A.-P. E.; van Gunsteren, W. F. Development of a nonlinear classical polarization model for liquid water and aqueous solutions: COS/D. *J. Phys. Chem. A* **2009**, *113*, 11570–11579.

(92) Lamoureux, G.; MacKerell, A. D.; Roux, B. A simple polarizable model of water based on classical Drude oscillators. *J. Chem. Phys.* **2003**, *119*, 5185–5197.

(93) Lamoureux, G.; Harder, E.; Vorobyov, I. V.; Roux, B.; MacKerell, A. D. A polarizable model of water for molecular dynamics simulations of biomolecules. *Chem. Phys. Lett.* **2006**, *418*, 245 – 249.

(94) Ren, P.; Ponder, J. W. Polarizable atomic multipole water model for molecular mechanics simulation. *J. Phys. Chem. B* **2003**, *107*, 5933–5947.

(95) Laury, M. L.; Wang, L.-P.; Pande, V. S.; Head-Gordon, T.; Ponder, J. W. Revised parameters for the AMOEBA polarizable atomic multipole water model. *J. Phys. Chem. B* **2015**, *119*, 9423–9437.

(96) Jorgensen, W. L.; Chandrasekhar, J.; Madura, J. D.; Impey, R. W.; Klein, M. L. Comparison of simple potential functions for simulating liquid water. *J. Chem. Phys.* **1983**, *79*, 926–935.

(97) Jorgensen, W. L.; Chandrasekhar, J.; Madura, J. D.; Impey, R. W.; Klein, M. L. Comparison of simple potential functions for simulating liquid water. *J. Comput. Phys.* **1983**, *79*, 926–935.

(98) Mark, P.; Nilsson, L. Structure and dynamics of the TIP3P, SPC, and SPC/E water models at 298 K. *J. Phys. Chem. A* **2001**, *105*, 9954–9960.

(99) Berendsen, H. J. C.; Grigera, J. R.; Straatsma, T. P. The missing term in effective pair potentials. *J. Phys. Chem.* **1987**, *91*, 6269–6271.

(100) Horn, H. W.; Swope, W. C.; Pitera, J. W.; Madura, J. D.; Dick, T. J.; Hura, G. L.; Head-Gordon, T. Development of an improved four-site water model for biomolecular simulations: TIP4P-Ew. *J. Comput. Phys.* **2004**, *120*, 9665–9678.

(101) Rick, S. W. A reoptimization of the five-site water potential (TIP5P) for use with Ewald sums. *J. Comput. Phys.* **2004**, *120*, 6085–6093.

(102) Peng, D.-Y.; Robinson, D. B. A new two-constant equation of state. *Ind. Eng. Chem. Fundam.* **1976**, *15*, 59–64.

(103) Soave, G. Equilibrium constants from a modified Redlich-Kwong equation of state. *Chem. Eng. Sci.* **1972**, *27*, 1197 – 1203.

(104) Twu, C. H.; Coon, J. E.; Bluck, D. Comparison of the Peng-Robinson and Soave-Redlich-Kwong equations of state using a new zero-pressure-based mixing Rule for the

prediction of high-pressure and high-temperature phase equilibria. *Ind. Eng. Chem. Res.* **1998**, *37*, 1580–1585.

(105) Péneloux, A.; Rauzy, E.; Fréze, R. A consistent correction for Redlich-Kwong-Soave volumes. *Fluid Phase Equilib.* **1982**, *8*, 7 – 23.

(106) Lin, C.-T.; Daubert, T. E. Estimation of partial molar volume and fugacity coefficient of components in mixtures from the soave and Peng-Robinson equations of state. *Ind. Eng. Chem. Process Des. Dev.* **1980**, *19*, 51–59.

(107) Leachman, J. W.; Jacobsen, R. T.; Penoncello, S.; Lemmon, E. W. Fundamental equations of state for parahydrogen, normal hydrogen, and orthohydrogen. *J. Phys.: Chem. Ref. Data.* **2009**, *38*, 721–748.

(108) Horn, H. W.; Swope, W. C.; Pitera, J. W.; Madura, J. D.; Dick, T. J.; Hura, G. L.; Head-Gordon, T. Development of an improved four-site water model for biomolecular simulations: TIP4P-EW. *J. Chem. Phys.* **2004**, *120*, 9665–9678.

(109) Mahoney, M. W.; Jorgensen, W. L. A five-site model for liquid water and the reproduction of the density anomaly by rigid, nonpolarizable potential functions. *J. Chem. Phys.* **2000**, *112*, 8910–8922.

(110) Wilhelm, E.; Waghorne, E.; Hefter, G.; Hummel, W.; Maurer, G.; Rebelo, L. P. N.; da Ponte, M. N.; Battino, R.; Clever, L.; van Hook, A.; Domanska-Zelazna, U.; Tomkins, R. P. T.; Richon, D.; de Stafani, V.; Coquelet, C.; Costa Gomes, M.; Siepmann, J. I.; Anderson, K. E.; Eckert, F.; Grolier, J.-P.; Boyer, S.; Salminen, J.; Dohrn, R.; Leiberich, R.; Fele Zilnik, L.; Fages, J.; Macedo, M. E.; Gmehling, J.; Brennecke, J.; Cordes, W.; Prausnitz, J.; Goodwin, A. R.; Marsh, K.; Peters, C. J.; Voigt, W.; Koenigsberger, E.; May, P.; Kamps, A. P.-S.; Shariati, A.; Raeissi, S.; Padua, A. A. H.; Sauceau, M.; Pinho, S. P. P.; Kaskiala, T.; Kobylin, P. In *Developments*

and Applications in Solubility; Letcher, T. M., Ed.; The Royal Society of Chemistry, 2007.

for Table of Contents use only
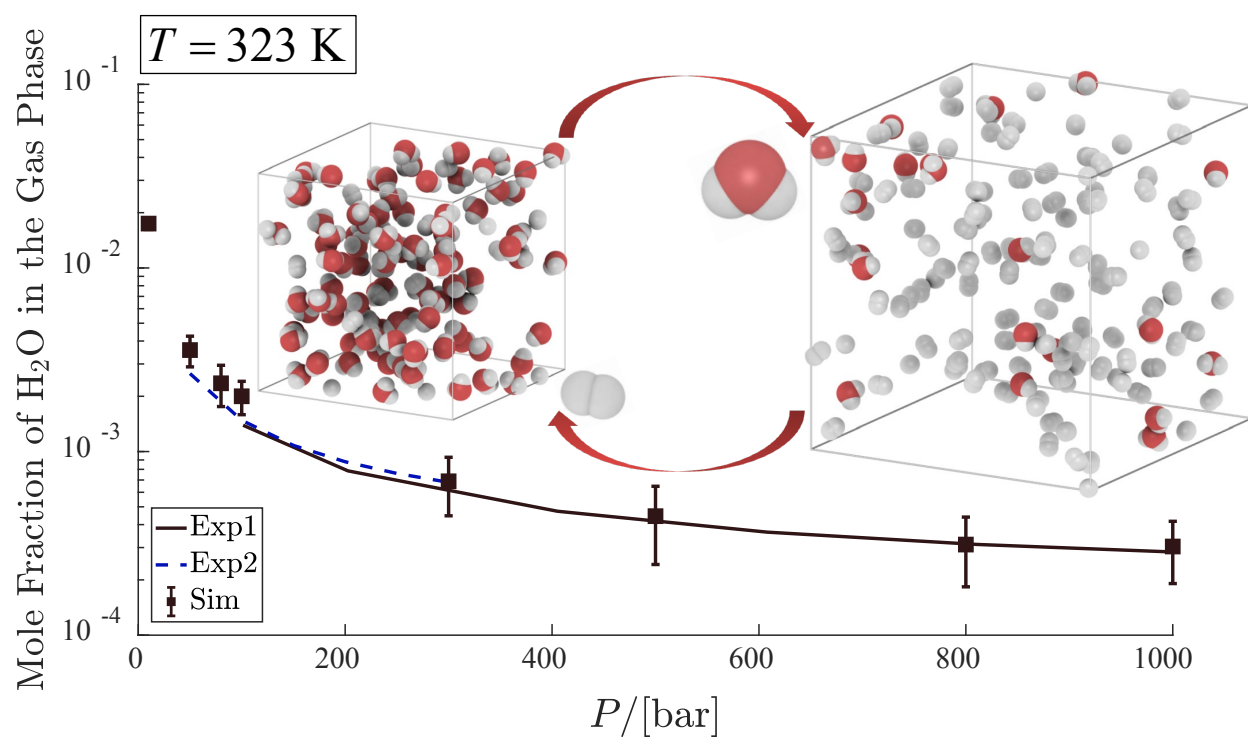
Supporting Information for: Solubility of Water in Hydrogen at High Pressure: a Molecular Simulation Study

Ahmadreza Rahbari,[†] Jeroen Brenkman,[‡] Remco Hens,[†] Mahinder Ramdin,[†] Leo J. P. van den Broeke,[†] Rogier Schoon,[‡] Ruud Henkes,[‡] Othonas A. Moultos,[†] and Thijs J. H. Vlugt[*,†]

†*Engineering Thermodynamics, Process & Energy Department, Faculty of Mechanical, Maritime and Materials Engineering, Delft University of Technology, Leeghwaterstraat 39, 2628CB, Delft, The Netherlands*

‡*Shell Global Solutions International, PO Box 38000, 1030BN, Amsterdam, the Netherlands*

E-mail: t.j.h.vlugt@tudelft.nl

Fugacity Coefficient

Consider a multicomponent system that is simulated in an ensemble that is either open (e.g. grand-canonical ensemble) or closed (NPT ensemble). In this system, we would like to calculate the fugacity coefficient ϕ_i of component i. We assume that a fractional molecule of component i is present. The chemical potential of component i equals[1,2]

$$\mu_i = \mu_i^0 + RT \ln \frac{\langle \rho_i \rangle}{\rho_0} + \mu_{\text{ex}}^i = \mu_i^0 + RT \ln \frac{\langle \rho_i \rangle}{\rho_0} - RT \ln \frac{p(\lambda_i = 1)}{p(\lambda_i = 0)} \tag{S1}$$

in which μ_i^0 is the reference state of the chemical potential, $\langle \rho_i \rangle$ is the average number density of i, μ_{ex}^i is the excess chemical potential of i, ρ_0 is an arbitrary reference density (to make the argument of the logarithm dimensionless), and $p(\lambda_i)$ is the probability distribution of the coupling parameter of the fractional molecule of i. In classical thermodynamics, the chemical potential of i is usually expressed as[3,4]

$$\mu_i = \mu_i^\star + RT \ln \left(\frac{y_i P \phi_i}{P_0} \right) \tag{S2}$$

in which $\mu_i^\star$ is a reference chemical potential (which is different from μ_i^0), y_i is the mole fraction of i, P is the pressure, and P_0 is a reference pressure (usually 1 bar). The reference chemical potentials μ_i^0 and $\mu_i^\star$ only depend on the temperature and not on the pressure or composition of the system. To find an expression for the fugacity coefficient ϕ_i, consider a system in which the pressure P is approaching zero while the composition of the mixture is constant. In this limit, $\phi_i = 1$ and $\mu_{\text{ex}}^i = 0$. We have

$$\mu_i^0 + RT \ln \frac{\langle \rho_i \rangle}{\rho_0} = \mu_i^\star + RT \ln \left(\frac{y_i P}{P_0} \right) \tag{S3}$$

In this limit, the ideal gas law can also be used to calculate the average number density of i,

$$\langle \rho_i \rangle = \frac{y_i P}{RT} \tag{S4}$$

This leads to

$$\mu_i^0 - \mu_i^\star = RT \ln \left(\frac{\rho_0 RT}{P_0} \right) \tag{S5}$$

This equation can be used to eliminate the reference state in Eq. S2 leading to

$$\mu_{\text{ex}}^i = RT \ln \left(\frac{y_i P \phi_i}{RT \langle \rho_i \rangle} \right) \tag{S6}$$

so

$$\phi_i = \frac{RT \langle \rho_i \rangle}{y_i P} \exp\left[\mu_{\mathrm{ex}}^i/(RT)\right] \tag{S7}$$

If the system consists of N_t molecules in total (including component i, and not counting fractional molecules), we have $\langle \rho_i \rangle \approx N_i / \langle V \rangle$ ($\langle V \rangle$ being the average volume) and $y_i = N_i / N_t$. We finally have

$$\phi_i = \frac{N_t RT}{P \langle V \rangle} \exp\left[\mu_{\mathrm{ex}}^i/(RT)\right] = \frac{\exp\left[\mu_{\mathrm{ex}}^i/(RT)\right]}{Z_m} \tag{S8}$$

in which $Z_m = \frac{P \langle V \rangle}{N_t RT}$ is the compressibility of the mixture. The fugacity coefficient ϕ_i thus depends on both the excess chemical potential of i and the overall deviation from ideal gas behavior of the mixture.

Table S1: Force field parameters for the water models used in this study. L is the dummy site for four-site models. For the TIP5P/Ew[5] model, L and M are the dummy sites. θ is the angle between atoms OHO, in degrees. For four-site water models $\varepsilon = 0.5\theta$. φ is the angle between the point charges of the dummy sites for the TIP5P/Ew. A cutoff radius of 12 Å was used for all LJ interactions. Analytic tail corrections and the Lorentz-Berthelot mixing rules were applied.[6,7]

Force Field Parameters	TIP3P[8]	SPC[9]	SPC/E[10]	OPC[11]	TIP4P/2005[12]	TIP4P/Ew[13]	TIP5P/Ew[5]
$\epsilon_{OO}/k_B/[\mathrm{K}]$	76.500	78.203	78.175	107.086	93.196	81.899	89.57888
$\sigma_{OO}/[\text{Å}]$	3.151	3.1656	3.166	3.1666	3.1589	3.1644	3.097
$q_O/[\mathrm{e}]$	-0.834	-0.82	-0.8476	-1.3582	-		-
$q_H/[\mathrm{e}]$	0.417	0.41	0.4238	0.6791	0.5564	0.52422	-
$q_L/[\mathrm{e}]$	-	-	-	-1.3582	-1.1128	-1.04844	-0.241
$q_M/[\mathrm{e}]$	-	-	-	-	-	-	0.241
$r_{OH}/[\text{Å}]$	0.957		1	0.8724	0.9572	0.9572	
$r_{OL}/[\text{Å}]$	-	-	-	0.1594	0.1546	0.125	
θ	104.52	109.47	109.47	103.6	104.52	104.52	104.52
φ	-	-	-	51.8	52.26	52.26	109.47

Table S2: Force field parameters for the hydrogen models used in this study. Dummy site L is the geometric center of mass for the Marx model. The H-H bond length of the two-site and three-site force fields is 0.74 Å. A cutoff radius of 12 Å was used for all LJ interactions. Analytic tail corrections and the Lorentz-Berthelot mixing rules were applied.[6,7]

Force Field Parameters	Buch[14]	Hirschfelder[15]	Vrabec[16]	Cracknell[17]	Marx[18]
$\epsilon_{HH}/k_B/[K]$	34.2	38	25.84	12.5	-
$\sigma_{HH}/[\text{Å}]$	2.96	2.915	3.0366	2.59	-
$q_H/[e]$	-	-	-	-	0.468
$q_L/[e]$	-	-	-	-	-0.936
$\epsilon_{LL}/k_B/[K]$	-	-	-	-	36.7
$\sigma_{LL}/[\text{Å}]$	-	-	-	-	2.958

Table S3: Calculated densities and fugacity coefficients of different hydrogen models obtained from CFC*NPT* simulations at $T = 323$ K and pressures between $P = 100$ and $P = 1000$ bar. The results from equation of state modelling are obtained using parameters from table S10. σ_x is the uncertainty of x. Results from cubic EoS and REFPROP[19,20] are also included.

$P/[\text{bar}]$	$\langle\rho\rangle/[\text{kg/m}^3]$	$\sigma_{\langle\rho\rangle}$	$\mu/k_\text{B}/[\text{K}]$	σ_ϕ
Hirschfelder[15]				
100	7.121	0.001	1.05	0.02
200	13.556	0.002	1.10	0.02
400	24.650	0.006	1.23	0.02
600	33.84	0.01	1.37	0.03
800	41.58	0.01	1.53	0.03
1000	48.22	0.02	1.71	0.03
Vrabec[16]				
100	7.027	0.001	1.06	0.02
200	13.239	0.002	1.14	0.02
400	23.733	0.005	1.30	0.02
600	32.30	0.01	1.48	0.02
800	39.49	0.01	1.67	0.03
1000	45.65	0.01	1.92	0.03
Buch[14]				
100	7.088	0.001	1.05	0.02
200	13.443	0.003	1.12	0.02
400	24.314	0.006	1.25	0.02
600	33.26	0.01	1.40	0.02
800	40.78	0.01	1.59	0.02
1000	47.22	0.01	1.79	0.03
Cracknell[17]				
100	7.133	0.001	1.05	0.02
200	13.611	0.003	1.10	0.02
400	24.891	0.005	1.21	0.02
600	34.37	0.01	1.35	0.02
800	42.45	0.01	1.50	0.03
1000	49.45	0.01	1.66	0.03
Marx[18]				
100	7.100	0.002	1.05	0.02
200	13.482	0.004	1.11	0.02
400	24.416	0.010	1.25	0.02
600	33.41	0.02	1.40	0.03
800	40.97	0.02	1.57	0.03
1000	47.42	0.02	1.76	0.04

$P/[\text{bar}]$	$\langle\rho\rangle/[\text{kg/m}^3]$	$\sigma_{\langle\rho\rangle}$	$\mu/k_\text{B}/[\text{K}]$	σ_ϕ
PR-EoS[21]				
100	7.35	-	1.03	-
200	14.05	-	1.07	-
400	25.60	-	1.17	-
600	35.00	-	1.28	-
800	42.73	-	1.42	-
1000	49.17	-	1.57	-
SRK-EoS[22]				
100	7.19	-	1.05	-
200	13.58	-	1.11	-
400	24.36	-	1.25	-
600	33.00	-	1.41	-
800	40.04	-	1.60	-
1000	45.87	-	1.82	-
REFPROP[19,20]				
100	7.10	-	1.06	-
200	13.46	-	1.12	-
400	24.29	-	1.26	-
600	33.17	-	1.42	-
800	40.63	-	1.60	-
1000	47.01	-	1.80	-

Table S4: Calculated densities and chemical potentials of different water models obtained from CFCNPT simulations at $T = 323$ K and pressures between $P = 100$ and $P = 1000$ bar. σ_x is the uncertainty of x. Results from cubic EoS and REFPROP[19,20] are also included.

$P/[\text{bar}]$	$\langle\rho\rangle/[\text{kg/m}^3]$	$\sigma_{\langle\rho\rangle}$	$\mu/k_{\text{B}}/[\text{K}]$	σ_μ
TIP3P[9]				
100	965	2	-4057	31
200	970	1	-4033	25
400	982	2	-3989	32
600	992	1	-3948	29
800	1002	1	-3905	30
1000	1011	1	-3861	25
SPC[8]				
100	962	2	-4075	24
300	973	2	-4021	32
500	982	1	-3987	26
800	996	2	-3912	29
1000	1005	1	-3873	28
SPC/E[10]				
100	987	2	-4482	36
300	997	1	-4424	33
500	1004	2	-4385	31
800	1017	2	-4311	42
1000	1025	2	-4271	42
TIP4P/2005[12]				
100	990	2	-4606	47
200	995	2	-4584	44
400	1003	2	-4554	49
600	1012	2	-4494	48
800	1020	2	-4467	55
1000	1027	2	-4408	45
TIP4P/Ew[13]				
100	987	2	-4433	35
300	996	2	-4388	25
500	1006	1	-4355	38
800	1018	2	-4291	41
1000	1025	2	-4242	38
OPC[11]				
100	991	2	-4946	38
300	998	2	-4902	52
500	1005	2	-4861	43

$P/$[bar]	$\langle\rho\rangle/$[kg/m^3]	$\sigma_{\langle\rho\rangle}$	$\mu/k_{\mathrm{B}}/$[K]	σ_μ
800	1017	2	-4808	59
1000	1025	2	-4730	61
TIP5P/Ew[5]				
100	990	2	-3845	24
300	1000	1	-3821	24
500	1011	2	-3769	27
800	1025	2	-3699	30
1000	1034	2	-3651	29
REFPROP[19,23]				
100	992.31	-	-4112.58	-
200	996.53	-	-4089.42	-
400	1004.7	-	-4043.47	-
600	1012.6	-	-3997.99	-
800	1020.1	-	-3952.96	-
1000	1027.4	-	-3908.32	-

Table S5: Experimental solubilities of hydrogen in $H_2O - H_2$ mixtures (liquid phase) at coexistence. Experimental data are converted to mole fractions for different temperatures and pressures. For the original units for each data set, see the indicated references below. For conversion to mole fractions, standard conditions at $T = 273.15$ K and $P = 1.01325$ atm are considered, unless otherwise mentioned in the reference.

T/[K]	P/[bar]	x_{H_2}	Ref
273.15	25	4.31×10^{-4}	[24]
273.15	51	8.63×10^{-4}	[24]
273.15	101	1.71×10^{-3}	[24]
273.15	203	3.35×10^{-3}	[24]
273.15	405	6.40×10^{-3}	[24]
273.15	608	9.25×10^{-3}	[24]
273.15	811	1.19×10^{-2}	[24]
273.15	1013	1.42×10^{-2}	[24]
298.15	25	3.50×10^{-4}	[24]
298.15	51	6.94×10^{-4}	[24]
298.15	101	1.39×10^{-3}	[24]
298.15	203	2.71×10^{-3}	[24]
298.15	405	5.24×10^{-3}	[24]
298.15	608	7.64×10^{-3}	[24]
298.15	811	9.90×10^{-3}	[24]
298.15	1013	1.20×10^{-2}	[24]
310.15	1.013	1.33×10^{-5}	[25]
310.93	3.4	4.50×10^{-5}	[26]
310.93	13.8	1.81×10^{-4}	[26]
310.93	31.0	4.10×10^{-4}	[26]
310.93	65.5	8.62×10^{-4}	[26]
310.93	103.4	1.33×10^{-3}	[26]
310.93	137.9	1.76×10^{-3}	[26]
323.15	25	3.26×10^{-4}	[24]
323.15	31.8	4.02×10^{-4}	[27]
323.15	51	6.49×10^{-4}	[24]
323.15	60.3	7.63×10^{-4}	[27]
323.15	101	1.29×10^{-3}	[24]
323.15	119.3	1.51×10^{-3}	[27]
323.15	203	2.54×10^{-3}	[24]
323.15	405	4.92×10^{-3}	[24]
323.15	608	7.18×10^{-3}	[24]
323.15	811	9.34×10^{-3}	[24]
323.15	1013	1.14×10^{-2}	[24]
348.15	25	3.32×10^{-4}	[24]
348.15	51	6.63×10^{-4}	[24]
348.15	101	1.32×10^{-3}	[24]

Continued on next page

T/[K]	P/[bar]	x_{H_2}	Ref
348.15	203	2.60×10^{-3}	[24]
348.15	405	5.04×10^{-3}	[24]
348.15	608	7.35×10^{-3}	[24]
348.15	811	9.54×10^{-3}	[24]
348.15	1013	1.17×10^{-2}	[24]
366.48	3.4	3.74×10^{-5}	[26]
366.48	13.8	2.0×10^{-4}	[28]
366.48	13.8	1.80×10^{-4}	[26]
366.48	27.6	3.7×10^{-4}	[28]
366.48	31.0	4.26×10^{-4}	[26]
366.48	55.2	7.5×10^{-4}	[28]
366.48	65.5	8.93×10^{-4}	[26]
366.48	110.3	1.50×10^{-3}	[28]
366.48	137.9	1.840×10^{-3}	[26]
373.15	21	3.01×10^{-4}	[29]
373.15	25	3.70×10^{-4}	[24]
373.15	31	4.48×10^{-4}	[29]
373.15	42	5.94×10^{-4}	[29]
373.15	42	5.17×10^{-4}	[30]
373.15	51	7.30×10^{-4}	[24]
373.15	57.0	8.20×10^{-4}	[27]
373.15	62	8.77×10^{-4}	[29]
373.15	62	7.61×10^{-4}	[30]
373.15	82	1.15×10^{-3}	[29]
373.15	82	1.02×10^{-3}	[30]
373.15	101	1.45×10^{-3}	[24]
373.15	102	1.32×10^{-3}	[30]
373.15	120.9	1.75×10^{-3}	[27]
373.15	153.7	2.23×10^{-3}	[27]
373.15	203	2.85×10^{-3}	[24]
373.15	405	5.46×10^{-3}	[24]
373.15	608	7.96×10^{-3}	[24]
373.15	811	1.03×10^{-2}	[24]
373.15	1013	1.25×10^{-2}	[24]
398.15	23	3.44×10^{-4}	[29]
398.15	33	5.04×10^{-4}	[29]
398.15	43	6.54×10^{-4}	[29]
398.15	52	7.18×10^{-4}	[30]
398.15	63	9.32×10^{-4}	[29]
398.15	82	1.13×10^{-3}	[30]
398.15	83	1.21×10^{-3}	[29]
398.15	87	1.21×10^{-3}	[30]
398.15	102	1.43×10^{-3}	[30]

Continued on next page

T/[K]	P/[bar]	x_{H_2}	Ref
422.04	31.0	5.00×10^{-4}	26
422.04	65.5	1.16×10^{-3}	26
422.04	103.4	1.88×10^{-3}	26
423.15	21	3.26×10^{-4}	29
423.15	30	4.95×10^{-4}	29
423.15	31	4.370×10^{-4}	30
423.15	40	6.55×10^{-4}	29
423.15	42	5.98×10^{-4}	30
423.15	52	7.79×10^{-4}	30
423.15	51.8	9.00×10^{-4}	27
423.15	54.3	9.79×10^{-4}	27
423.15	55	8.75×10^{-4}	29
423.15	62	9.43×10^{-4}	30
423.15	76	1.15×10^{-3}	29
423.15	75.9	1.35×10^{-3}	27
423.15	82	1.34×10^{-3}	30
423.15	87.1	1.60×10^{-3}	27
448.15	22	3.28×10^{-4}	29
448.15	29	4.83×10^{-4}	29
448.15	39	6.59×10^{-4}	29
448.15	52	7.46×10^{-4}	30
448.15	60	9.56×10^{-4}	29
448.15	62	9.43×10^{-4}	30
448.15	80	1.24×10^{-3}	29
473.15	26	3.30×10^{-4}	29
473.15	31	1.00×10^{-3}	29
473.15	36	5.74×10^{-4}	29
473.15	42	5.52×10^{-4}	30
473.15	46	8.44×10^{-4}	29
473.15	52	7.51×10^{-4}	30
473.15	76	1.22×10^{-3}	29
473.15	82	1.24×10^{-3}	30
473.15	102	1.40×10^{-3}	30
473.15	118	1.62×10^{-3}	30
477.59	27.6	3.5×10^{-4}	28
477.59	31.0	4.29×10^{-4}	26
477.59	55.2	1.05×10^{-3}	28
477.59	65.5	1.46×10^{-3}	26
477.59	103.4	2.57×10^{-3}	26
477.59	110.3	2.71×10^{-3}	28
498.15	33	3.22×10^{-4}	29
498.15	36	4.47×10^{-4}	29
498.15	41	5.91×10^{-4}	29

Continued on next page

T/[K]	P/[bar]	x_{H_2}	Ref
498.15	51	8.10×10^{-4}	[29]
498.15	62	9.93×10^{-4}	[30]
498.15	71	1.21×10^{-3}	[29]
498.15	92	1.45×10^{-3}	[30]
523.15	44	2.70×10^{-4}	[29]
523.15	47	4.45×10^{-4}	[29]
523.15	52	6.50×10^{-4}	[29]
523.15	60	8.93×10^{-4}	[29]
523.15	70	1.18×10^{-3}	[29]
548.15	63	3.01×10^{-4}	[29]
548.15	65	4.70×10^{-4}	[29]
548.15	68	6.54×10^{-4}	[29]
548.15	72	8.48×10^{-4}	[29]
548.15	80	1.19×10^{-3}	[29]
573.15	89	2.86×10^{-4}	[29]
573.15	91	5.42×10^{-4}	[29]
573.15	93	7.24×10^{-4}	[29]
573.15	96	8.80×10^{-4}	[29]
573.15	100	1.25×10^{-3}	[29]
574.81	110.3	1.41×10^{-3}	[28]
588.70	110.3	2.26×10^{-3}	[28]
588.71	137.9	2.98×10^{-3}	[26]

Table S6: Experimental solubilities of water in $H_2O - H_2$ mixtures (gas phase) at coexistence. Experimental data are converted to mole fractions for different temperatures and pressures. For the original units for each data set, see references below. For conversion to mole fractions, standard conditions at $T = 273.15$ K and $P = 1.01325$ atm are considered, unless otherwise mentioned in the reference.

$T/[\text{K}]$	$P/[\text{bar}]$	x_{H_2}	Ref
310.93	3.4	1.96×10^{-2}	26
310.93	13.8	4.88×10^{-3}	26
310.93	31.0	2.22×10^{-3}	26
310.93	65.5	1.16×10^{-3}	26
310.93	103.4	7.6×10^{-4}	26
310.93	137.9	6.0×10^{-4}	26
310.95	13.8	4.88×10^{-3}	31
310.95	31.0	2.22×10^{-3}	31
310.95	65.5	1.16×10^{-3}	31
310.95	103.4	7.60×10^{-4}	31
323.15	50	2.66×10^{-3}	32
323.15	100	1.48×10^{-3}	32
323.15	101.3	1.38×10^{-3}	33
323.15	150	1.08×10^{-3}	32
323.15	200	8.8×10^{-4}	32
323.15	202.7	7.84×10^{-4}	33
323.15	250	7.6×10^{-4}	32
323.15	300	6.8×10^{-4}	32
323.15	405.3	4.64×10^{-4}	33
323.15	608.0	3.61×10^{-4}	33
323.15	1013.3	2.80×10^{-4}	33
343.15	50	6.60×10^{-3}	32
343.15	100	3.58×10^{-3}	32
343.15	150	2.57×10^{-3}	32
343.15	200	2.07×10^{-3}	32
343.15	250	1.77×10^{-3}	32
343.15	300	1.57×10^{-3}	32
366.45	13.8	3.86×10^{-3}	31
366.45	31.0	2.64×10^{-3}	31
366.45	65.5	1.32×10^{-3}	31
366.45	137.9	6.68×10^{-3}	31
366.48	3.4	2.47×10^{-1}	26
366.48	13.8	5.54×10^{-2}	28
366.48	13.8	5.86×10^{-2}	26
366.48	27.6	3.08×10^{-2}	28
366.48	31.0	2.64×10^{-2}	26
366.48	55.2	1.63×10^{-2}	28

Continued on next page

T/[K]	P/[bar]	y_{H_2O}	Ref
366.48	65.5	1.32×10^{-2}	[26]
366.48	110.3	6.51×10^{-3}	[28]
366.48	137.9	6.68×10^{-3}	[26]
422.04	31.0	1.570×10^{-1}	[26]
422.04	65.5	7.53×10^{-2}	[26]
422.04	103.4	5.13×10^{-2}	[26]
423.15	50	1.06×10^{-1}	[32]
423.15	100	6.00×10^{-2}	[32]
423.15	150	4.40×10^{-2}	[32]
423.15	200	3.60×10^{-2}	[32]
423.15	250	3.12×10^{-2}	[32]
423.15	300	2.83×10^{-2}	[32]
448.15	50	2.06×10^{-1}	[32]
448.15	100	1.21×10^{-1}	[32]
448.15	150	9.27×10^{-2}	[32]
448.15	200	7.80×10^{-2}	[32]
448.15	250	6.88×10^{-2}	[32]
448.15	300	6.23×10^{-2}	[32]
473.15	50	2.66×10^{-1}	[32]
473.15	100	1.48×10^{-1}	[32]
473.15	150	1.08×10^{-1}	[32]
473.15	200	8.8×10^{-2}	[32]
473.15	250	7.6×10^{-2}	[32]
473.15	300	6.9×10^{-2}	[32]
477.59	27.6	6.34×10^{-1}	[28]
477.59	31.0	5.55×10^{-1}	[26]
477.59	55.2	3.26×10^{-1}	[28]
477.59	65.5	2.85×10^{-1}	[26]
477.59	103.4	1.88×10^{-1}	[26]
477.59	110.3	1.72×10^{-1}	[28]
498.15	50	5.54×10^{-1}	[32]
498.15	100	3.22×10^{-1}	[32]
498.15	150	2.44×10^{-1}	[32]
498.15	200	2.08×10^{-1}	[32]
498.15	250	1.83×10^{-1}	[32]
498.15	300	1.67×10^{-1}	[32]
523.15	50	8.26×10^{-1}	[32]
523.15	100	4.96×10^{-1}	[32]
523.15	150	3.83×10^{-1}	[32]
523.15	200	3.27×10^{-1}	[32]
523.15	250	2.94×10^{-1}	[32]
523.15	300	2.71×10^{-1}	[32]
548.15	100	6.86×10^{-1}	[32]

Continued on next page

$T/[K]$	$P/[bar]$	y_{H_2O}	Ref
548.15	150	5.36×10^{-1}	[32]
548.15	200	4.61×10^{-1}	[32]
548.15	250	4.16×10^{-1}	[32]
548.15	300	3.86×10^{-1}	[32]
573.15	100	9.00×10^{-1}	[32]
573.15	150	7.22×10^{-1}	[32]
573.15	200	6.33×10^{-1}	[32]
573.15	250	5.82×10^{-1}	[32]
573.15	300	5.51×10^{-1}	[32]
574.81	110.3	8.45×10^{-1}	[28]
588.7	110.3	9.67×10^{-1}	[28]
588.71	137.9	8.10×10^{-1}	[26]

Table S7: Computed compositions of $H_2O - H_2$ mixtures at coexistence using MC simulations. x_{H_2} is the mole fraction of hydrogen in the liquid phase, y_{H_2O} is the mole fraction of water in the gas phase. The $H_2O - H_2$ mixture is defined by the TIP3P[9]-Marx[18] force fields. The simulation techniques are described in the main text. σ_x is the uncertainty of x.

T/[K]	P/[bar]	x_{H_2}/[$-$]	$\sigma_{x_{H_2}}$	y_{H_2O}/[$-$]	$\sigma_{y_{H_2O}}$	Sim. Tech.
283	10	1.510×10^{-4}	9×10^{-7}	1.8×10^{-3}	1×10^{-4}	CFCNPT
283	50	7.48×10^{-4}	6×10^{-6}	3.7×10^{-4}	3×10^{-5}	CFCNPT
283	80	1.174×10^{-3}	8×10^{-6}	2.4×10^{-4}	2×10^{-5}	CFCNPT
283	100	1.47×10^{-3}	1×10^{-5}	2.0×10^{-4}	1×10^{-5}	CFCNPT
283	300	4.28×10^{-3}	4×10^{-5}	7.3×10^{-5}	5×10^{-6}	CFCNPT
283	500	6.79×10^{-3}	7×10^{-5}	4.8×10^{-5}	4×10^{-6}	CFCNPT
283	800	9.51×10^{-3}	9×10^{-5}	3.5×10^{-5}	2×10^{-6}	CFCNPT
283	1000	1.162×10^{-2}	9×10^{-5}	2.9×10^{-5}	4×10^{-6}	CFCNPT
310	10	1.6×10^{-4}	2×10^{-5}	9.3×10^{-3}	8×10^{-4}	GE
310	50	8.1×10^{-4}	8×10^{-5}	2.3×10^{-3}	4×10^{-4}	GE
310	80	1.29×10^{-3}	9×10^{-5}	1.3×10^{-3}	5×10^{-4}	GE
310	100	1.6×10^{-3}	1×10^{-4}	1.2×10^{-3}	3×10^{-4}	GE
310	100	1.64×10^{-3}	2×10^{-5}	9.8×10^{-4}	7×10^{-5}	CFCNPT
310	300	4.59×10^{-3}	9×10^{-5}	3.5×10^{-4}	4×10^{-5}	CFCNPT
310	500	7.3×10^{-3}	1×10^{-4}	2.4×10^{-4}	5×10^{-5}	CFCNPT
310	800	1.08×10^{-2}	2×10^{-4}	1.7×10^{-4}	4×10^{-5}	CFCNPT
310	1000	1.31×10^{-2}	2×10^{-4}	1.4×10^{-4}	5×10^{-5}	CFCNPT
323	10	1.7×10^{-4}	1×10^{-5}	1.74×10^{-2}	1×10^{-3}	GE
323	50	8.8×10^{-4}	7×10^{-5}	3.57×10^{-3}	7×10^{-4}	GE
323	80	1.4×10^{-3}	1×10^{-4}	2.35×10^{-3}	6×10^{-4}	GE
323	100	1.7×10^{-3}	1×10^{-4}	2.00×10^{-3}	4×10^{-4}	GE
323	300	4.8×10^{-3}	4×10^{-4}	6.89×10^{-4}	2×10^{-4}	GE
323	500	7.6×10^{-3}	6×10^{-4}	4.45×10^{-4}	2×10^{-4}	GE
323	800	1.14×10^{-2}	8×10^{-4}	3.12×10^{-4}	1×10^{-4}	GE
323	1000	1.4×10^{-2}	1×10^{-3}	3.04×10^{-4}	1×10^{-4}	GE
323	100	1.72×10^{-3}	2×10^{-5}	1.8×10^{-3}	1×10^{-4}	CFCNPT
323	300	4.90×10^{-3}	5×10^{-5}	6.4×10^{-4}	8×10^{-5}	CFCNPT
323	500	7.7×10^{-3}	1×10^{-4}	4.2×10^{-4}	7×10^{-5}	CFCNPT
323	800	1.15×10^{-2}	3×10^{-4}	3.1×10^{-4}	6×10^{-5}	CFCNPT
323	1000	1.35×10^{-2}	2×10^{-4}	2.6×10^{-4}	6×10^{-5}	CFCNPT
366	10	2.1×10^{-4}	1×10^{-5}	1.08×10^{-1}	7×10^{-3}	GE
366	50	1.16×10^{-3}	5×10^{-5}	2.2×10^{-2}	2×10^{-3}	GE
366	80	1.86×10^{-3}	8×10^{-5}	1.41×10^{-1}	9×10^{-4}	GE
366	100	2.28×10^{-3}	8×10^{-5}	1.14×10^{-1}	6×10^{-4}	GE
366	300	6.4×10^{-3}	3×10^{-4}	4.2×10^{-1}	5×10^{-4}	GE
366	500	1.03×10^{-2}	6×10^{-4}	2.7×10^{-1}	4×10^{-4}	GE
366	800	1.49×10^{-2}	7×10^{-4}	1.8×10^{-1}	4×10^{-4}	GE

Continued on next page

$T/[\mathrm{K}]$	$P/[\mathrm{bar}]$	$x_{\mathrm{H_2}}/[-]$	$\sigma_{x_{\mathrm{H_2}}}$	$y_{\mathrm{H_2O}}/[-]$	$\sigma_{y_{\mathrm{H_2O}}}$	Sim. Tech.
366	1000	1.80×10^{-2}	9×10^{-4}	1.4×10^{-1}	4×10^{-4}	GE
423	50	1.70×10^{-3}	5×10^{-5}	1.38×10^{-1}	6×10^{-3}	GE
423	80	2.85×10^{-3}	9×10^{-5}	8.6×10^{-2}	4×10^{-3}	GE
423	100	3.5×10^{-3}	1×10^{-4}	7.2×10^{-2}	3×10^{-3}	GE
423	300	1.03×10^{-2}	4×10^{-4}	2.5×10^{-2}	1×10^{-3}	GE
423	500	1.62×10^{-2}	6×10^{-4}	1.58×10^{-2}	8×10^{-4}	GE
423	800	2.35×10^{-2}	9×10^{-4}	1.02×10^{-2}	5×10^{-4}	GE
423	1000	2.8×10^{-2}	1×10^{-3}	8.2×10^{-3}	6×10^{-4}	GE

Table S8: Computed compositions of $H_2O - H_2$ mixtures at coexistence using MC simulations. x_{H_2} is the mole fraction of hydrogen in the liquid phase, y_{H_2O} is the mole fraction of water in the gas phase. The $H_2O - H_2$ mixture is defined by the TIP4P/2005[12]-Marx[18] force fields. σ_x is the uncertainty of x.

T/[K]	P/[bar]	x_{H_2}/[−]	$\sigma_{x_{H_2}}$	y_{H_2O}/[−]	$\sigma_{y_{H_2O}}$	Sim. Tech.
323	10	1.2×10^{-4}	1×10^{-5}	3.6×10^{-3}	6×10^{-4}	GE
323	50	5.9×10^{-4}	9×10^{-5}	9×10^{-4}	5×10^{-4}	GE
323	80	9.1×10^{-4}	9×10^{-5}	6×10^{-4}	4×10^{-4}	GE
323	100	1.2×10^{-3}	1×10^{-4}	5×10^{-4}	4×10^{-4}	GE
323	300	3.3×10^{-3}	4×10^{-4}	2×10^{-4}	1×10^{-4}	GE
323	500	5.3×10^{-3}	5×10^{-4}	1×10^{-4}	1×10^{-4}	GE
323	800	8.0×10^{-3}	1×10^{-3}	1×10^{-4}	1×10^{-4}	GE
323	1000	1.0×10^{-4}	1×10^{-3}	8×10^{-5}	1×10^{-4}	GE
366	10	1.3×10^{-4}	1×10^{-5}	2.8×10^{-2}	2×10^{-3}	GE
366	50	6.6×10^{-4}	4×10^{-5}	5.8×10^{-3}	5×10^{-4}	GE
366	80	1.0×10^{-3}	6×10^{-5}	3.8×10^{-3}	5×10^{-4}	GE
366	100	1.27×10^{-3}	8×10^{-5}	3.3×10^{-3}	5×10^{-4}	GE
366	300	3.6×10^{-3}	3×10^{-4}	1.2×10^{-3}	5×10^{-4}	GE
366	500	5.9×10^{-3}	6×10^{-4}	9×10^{-4}	4×10^{-4}	GE
366	800	8.7×10^{-3}	8×10^{-4}	5×10^{-4}	3×10^{-4}	GE
366	1000	1.02×10^{-2}	8×10^{-4}	4×10^{-4}	2×10^{-4}	GE
423	50	8.4×10^{-4}	4×10^{-5}	4.5×10^{-2}	2×10^{-3}	GE
423	80	1.37×10^{-3}	6×10^{-5}	2.8×10^{-2}	2×10^{-3}	GE
423	100	1.73×10^{-3}	8×10^{-5}	2.3×10^{-2}	1×10^{-3}	GE
423	300	4.9×10^{-3}	2×10^{-4}	8.0×10^{-3}	6×10^{-4}	GE
423	500	7.8×10^{-3}	4×10^{-4}	5.0×10^{-3}	5×10^{-4}	GE
423	800	1.18×10^{-2}	5×10^{-4}	3.3×10^{-3}	4×10^{-4}	GE
423	1000	1.41×10^{-2}	8×10^{-4}	2.8×10^{-3}	4×10^{-4}	GE

Table S9: Computed compositions of $H_2O - H_2$ mixtures at coexistence using MC simulations. x_{H_2} is the mole fraction of hydrogen in the liquid phase, y_{H_2O} is the mole fraction of water in the gas phase. The $H_2O - H_2$ mixture is defined by the TIP5P/Ew[5]-Marx[18] force fields. σ_x is the uncertainty of x.

$T/[K]$	$P/[bar]$	$x_{H_2}/[-]$	$\sigma_{x_{H_2}}$	$y_{H_2O}/[-]$	$\sigma_{y_{H_2O}}$	Sim. Tech.
323	10	1.67×10^{-4}	8×10^{-6}	2.9×10^{-2}	2×10^{-3}	GE
323	50	8.5×10^{-4}	6×10^{-5}	6×10^{-3}	1×10^{-3}	GE
323	100	1.7×10^{-3}	1×10^{-4}	3.0×10^{-3}	6×10^{-4}	GE
323	300	4.9×10^{-3}	4×10^{-4}	1.4×10^{-3}	5×10^{-4}	GE
323	500	7.9×10^{-3}	8×10^{-4}	8×10^{-4}	4×10^{-4}	GE
323	800	1.2×10^{-2}	1×10^{-3}	6×10^{-4}	3×10^{-4}	GE
366	10	1.9×10^{-4}	1×10^{-5}	1.75×10^{-1}	7×10^{-3}	GE
366	50	2.34×10^{-3}	7×10^{-5}	2.27×10^{-2}	9×10^{-4}	GE
366	100	2.12×10^{-3}	9×10^{-5}	1.9×10^{-2}	1×10^{-3}	GE
366	300	6.1×10^{-3}	3×10^{-4}	6.8×10^{-3}	5×10^{-4}	GE
366	500	9.7×10^{-3}	5×10^{-4}	4.4×10^{-3}	4×10^{-4}	GE
366	800	1.42×10^{-2}	5×10^{-4}	2.9×10^{-3}	4×10^{-4}	GE
366	1000	1.73×10^{-2}	9×10^{-4}	2.4×10^{-3}	4×10^{-4}	GE
423	50	1.64×10^{-3}	6×10^{-5}	2.2×10^{-1}	1×10^{-2}	GE
423	100	3.6×10^{-3}	1×10^{-4}	1.14×10^{-1}	5×10^{-3}	GE
423	300	1.05×10^{-2}	3×10^{-4}	4.1×10^{-2}	2×10^{-3}	GE
423	500	1.65×10^{-2}	5×10^{-4}	2.6×10^{-2}	1×10^{-3}	GE
423	800	2.40×10^{-2}	8×10^{-4}	1.7×10^{-2}	1×10^{-3}	GE
423	1000	2.8×10^{-2}	1×10^{-3}	1.41×10^{-2}	7×10^{-4}	GE

Table S10: Parameters used for equation of state modeling: critical temperatures (T_c), pressures (P_c), and acentric factors (ω) the components at the standard reference state (1 bar).[34–36]

Component	T_c /[K]	P_c /[Pa]	ω
H_2	33.14	1296400	-0.219
H_2O	647.1	22064000	0.3443

References

(1) Poursaeidesfahani, A.; Hens, R.; Rahbari, A.; Ramdin, M.; Dubbeldam, D.; Vlugt, T. J. H. Efficient application of Continuous Fractional Component Monte Carlo in the Reaction Ensemble. *J. Chem. Theory Comput.* **2017**, *13*, 4452–4466.

(2) Poursaeidesfahani, A.; Torres-Knoop, A.; Dubbeldam, D.; Vlugt, T. J. H. Direct Free Energy Calculation in the Continuous Fractional Component Gibbs Ensemble. *J. Chem. Theory Comput.* **2016**, *12*, 1481–1490.

(3) McQuarrie, D. A.; Simon, J. D. *Physical Chemistry: A Molecular Approach*, 1st ed.; University Science Books: Sausalito, California, 1997.

(4) Walas, S. M. *Phase Equilibria in Chemical Engineering*, 1st ed.; Butterworth-Heinemann: USA, 1985.

(5) Rick, S. W. A reoptimization of the five-site water potential (TIP5P) for use with Ewald sums. *J. Comput. Phys.* **2004**, *120*, 6085–6093.

(6) Allen, M. P.; Tildesley, D. J. *Computer simulation of liquids*, 2nd ed.; Oxford university press: Oxford, United Kingdom, 2017.

(7) Frenkel, D.; Smit, B. *Understanding molecular simulation: from algorithms to applications*, 2nd ed.; Academic Press: San Diego, California, 2002.

(8) Mark, P.; Nilsson, L. Structure and dynamics of the TIP3P, SPC, and SPC/E water models at 298 K. *J. Phys. Chem. A* **2001**, *105*, 9954–9960.

(9) Jorgensen, W. L.; Chandrasekhar, J.; Madura, J. D.; Impey, R. W.; Klein, M. L. Comparison of simple potential functions for simulating liquid water. *J. Chem. Phys.* **1983**, *79*, 926–935.

(10) Berendsen, H. J. C.; Grigera, J. R.; Straatsma, T. P. The missing term in effective pair potentials. *J. Phys. Chem.* **1987**, *91*, 6269–6271.

(11) Izadi, S.; Anandakrishnan, R.; Onufriev, A. V. Building Water Models: a different approach. *J. Phys. Chem. Lett.* **2014**, *5*, 3863–3871.

(12) Abascal, J. L. F.; Vega, C. A general purpose model for the condensed phases of water: TIP4P/2005. *J. Chem. Phys.* **2005**, *123*, 234505.

(13) Horn, H. W.; Swope, W. C.; Pitera, J. W.; Madura, J. D.; Dick, T. J.; Hura, G. L.; Head-Gordon, T. Development of an improved four-site water model for biomolecular simulations: TIP4P-EW. *J. Chem. Phys.* **2004**, *120*, 9665–9678.

(14) Buch, V. Path integral simulations of mixed para-D_2 and ortho-D_2 clusters: The orientational effects. *J. Chem. Phys.* **1994**, *100*, 7610–7629.

(15) Hirschfelder, C.; Curtiss, F.; Bird, R. B. *Molecular Theory of Gases and Liquids*; Wiley: New York, 1954.

(16) Köster, A.; Thol, M.; Vrabec, J. Molecular models for the hydrogen age: hydrogen, nitrogen, oxygen, argon, and water. *J. Chem. Eng. Data* **2018**, *63*, 305–320.

(17) Cracknell, R. F. Molecular simulation of hydrogen adsorption in graphitic nanofibres. *Phys. Chem. Chem. Phys.* **2001**, *3*, 2091–2097.

(18) Marx, D.; Nielaba, P. Path-integral Monte Carlo techniques for rotational motion in two dimensions: Quenched, annealed, and no-spin quantum-statistical averages. *Phys. Rev. A* **1992**, *45*, 8968–8971.

(19) Lemmon, E. W.; Span, R. Short fundamental equations of state for 20 industrial fluids. *J. Chem. Eng. Data* **2006**, *51*, 785–850.

(20) Lemmon, E. W.; Huber, M. L.; McLinden, M. O. NIST reference fluid thermodynamic and transport properties–REFPROP. *NIST standard reference database* **2002**, *23*, v7, https://www.nist.gov/publications/nist-standard-reference-database-23-reference-fluid-thermodynamic-and-transport.

(21) Peng, D.-Y.; Robinson, D. B. A new two-constant equation of state. *Ind. Eng. Chem. Fundam.* **1976**, *15*, 59–64.

(22) Soave, G. Equilibrium constants from a modified Redlich-Kwong equation of state. *Chem. Eng. Sci.* **1972**, *27*, 1197 – 1203.

(23) Wagner, W.; Pruß, A. The IAPWS formulation 1995 for the thermodynamic properties of ordinary water substance for general and scientific use. *J. Phys. Chem. Ref. Data* **2002**, *31*, 387–535.

(24) Wiebe, R.; Gaddy, V. L. The solubility of hydrogen in water at 0, 50, 75 and 100Âř from 25 to 1000 atmospheres. **2005**, *56*, 76–79.

(25) Meyer, M.; Tebbe, U.; Piiper, J. Solubility of inert gases in dog blood and skeletal muscle. *Pflügers Archiv European Journal of Physiology* **1980**, *384*, 131–134.

(26) Gillespie, P. C.; Wilson, G. M. *Vapor-Liquid Equilibrium Data on Water-Substitue Gas Components*; 1980; pp RR_41, 1–34.

(27) Kling, G.; Maurer, G. The solubility of hydrogen in water and in 2-aminoethanol at temperatures between 323 K and 423 K and pressures up to 16 M Pa. *Chem. Thermodynamics* **1991**, *23*, 531–541.

(28) Devaney, W.; Berryman, J. M.; Kao, P.-L.; Eakin, B. *High Temperature V-L-E Measurements for Substitute Gas Components*; 1978; pp 1–27.

(29) Jung, J. Loslichkeit von Kohlenmonoxid und Wasserstoff in Wasser zwisen 0 C und 300 C. Ph.D. thesis, RWTH Aachen, 1962.

(30) Ipatev, V.; Teodorovich, V. Equilibrium compositions of vapor-gas mixtures over solutions. *Zh.Obshch.Khim.* **1934**, *4*, 395–399.

(31) Ugrozov, V. V. Equilibrium compositions of vapor-gas mixtures over solutions. **1996**, *70*, 1240–1241.

(32) Maslennikova, V. Y.; Goryunova, N.; Subbotina, L.; Tsiklis, D. The Solubility of Water in Compressed Hydrogen. *Russian Journal of Physical Chemistry* **1976**, *50*, 240–243.

(33) Bartlett, E. P. The concentration of water vapor in compressed hydrogen, Nitrogen and a mixture of these gases in the presence of condensed water. *Journal of the American Chemical Society* **1927**, *49*, 65–78.

(34) Yaws, C. L. *Thermophysical properties of chemicals and hydrocarbons*, 2nd ed.; Gulf Professional Publishing: Oxford, UK, 2014.

(35) Chase, M. W.; Curnutt, J.; Prophet, H.; McDonald, R.; Syverud, A. JANAF thermochemical tables, 1975 supplement. *J. Phys. Chem. Ref. Data.* **1975**, *4*, 1–176.

(36) Chase, M. W. NIST-JANAF Themochemical Tables, Fourth Edition. *J. Phys. Chem. Ref. Data* **1998**, *4*, 1–1951.